FACHBEREICH PHYSIK
UNIVERSITÄT DORTMUND

Design and Realisation of a new AMANDA Data Acquisition System with Transient Waveform Recorders

Dissertation zur Erlangung des Doktorgrades

vorgelegt von

Wolfgang Wagner

Dortmund/Wuppertal, Oktober 2004

Contents

1

Introduction

Some of the most exciting problems in astrophysics are the origin of the *cosmic rays* and the understanding of the accelerating processes. Probably neutrinos can play a role in answering these questions.
The charged part of the cosmic rays, e.g. nuclei, protons and electrons, are deflected by magnetic fields and lose all directional information, while stable neutral particles, i.e. neutrinos and photons, traverse the magnetic fields undeflected. In addition, charged particles and photons interact with matter and various radiation fields and are absorbed or deflected. In contrast, neutrinos have a very small cross section and can traverse the Universe mostly undisturbed.
Since many astronomical objects are obscured by matter and photon shields, neutrinos are the only particle type to escape from the inner core of the objects, delivering information about the relevant processes.
Due to the small cross section of neutrino interactions, neutrino detectors have to be very large in order to observe a sufficient number of events. High energetic neutrinos interacting with matter will produce secondary leptons, i.e. muons, electrons and taus, which can be observed by these detectors. The high energetic leptons can be detected in transparent media, i.e. water or ice, by the emitted Čerenkov light.
Neutrino detectors suffer from a large muon background produced by cosmic ray showers in the atmosphere. Therefore, the detectors are located under ground to shield them from the atmospheric muon background. In order to identify muons produced by neutrinos, the Earth is used as a filter. Muons propagating upwards through the detector are considered as secondary particles from neutrino interactions, while downwards moving muons are related to the atmospheric background.
The demands on neutrino detectors are

- a sufficient angular resolution $< 5^\circ$ in order to identify point sources

accurately. This can only be achieved by a good relative time resolution.

- a sufficient energy resolution to measure the diffuse spectrum of neutrinos over a wide energy range. Thus, the dynamic range of the detector has to be large.
- a high sensitivity at low energies to enable detection of low energetic neutrinos from supernovae and exotic particles.
- a dead-time free operation of the detector.

One of these underground detectors is the *Antarctic Muon and Neutrino Detector Array AMANDA*, a Čerenkov telescope, located in the deep ice at the geographical South Pole. The detector consists of 19 strings of *photomultiplier tubes PMTs*. The signals from the PMTs are measured by *Time to Digital Converters TDCs* and *peak sensing Analog to Digital Converters pADCs*. AMANDA is a working neutrino telescope, but many opportunities remain to improve the detector. The present *Data AcQuisition DAQ* system – MuonDaq – limits the detector capabilities. The major critical points can be summarised:

- The detector saturates for high energy events above 10^{16} eV limiting the sensitivity for high energy events and the energy resolution. Since the search for the sources of the extraterrestrial neutrinos is the main goal of neutrino astronomy, it is important to make detectors sensitive for high energy neutrinos [LM00]. It is expected that at an energy above 10^{16} eV the muon flux from neutrino interactions exceeds the atmospheric muon flux allowing for a better background rejection.
- The dead-time of the MuonDaq amounts to 15% [Sch02].
- The fact that the pADCs measure only the maximum amplitude causes ambiguities for complex signals.

The purpose of this thesis is the design and realisation of a new DAQ for the AMANDA detector in order to avoid the limitations of the present system and to extend the capabilities of the whole detector. The new system uses *Flash Analog to Digital Converters FADC* to digitise the full signal of the light sensors in each event.
A short introduction to high energy cosmic ray physics is given in chapter 2. Possible sources for extraterrestrial neutrinos are discussed and different models of neutrino fluxes from these sources are presented.
In chapter 3, a description of the AMANDA detector and the present DAQ system will follow. The principles of calibration and reconstruction are also explained in this chapter.

The layout of the improved new AMANDA DAQ system – TWRDaq – is decribed in chapter 4. The first steps towards an analysis of the data from TWRDaq are presented in chapter 5. The first results of a comparison between MuonDaq and TWRDaq are also presented in chapter 5.
Finally, the first steps to build a new trigger system based on an online analysis of the captured data are described. This system will be capable of searching for coincident hits within the detector volume and is presented in chapter 6.

2

Particle Physics and Cosmic Rays

2.1 The birth of Particle Physics

With the discovery of natural radioactivity, in 1896 by Henri Becquerel, and the discovery of the first elementary particle, the electron by Sir Joseph J. Thomson in 1897, the era of particle physics began. These discoveries gave the first hints that the atom is not the smallest constituent of matter.
In 1900 it was already known that the discharging rate of an electroscope depends on the amount of ionised particles in the air. Furthermore, it was found that an electroscope discharges in the presence of radioactivity. Initially, the origin of ionisation in air was assumed to be due to natural radioactivity in the air or from the Earth. A first measurement on the Eiffel tower showed a slight decrease of the discharging rate with height, but there was still a high level of ionisation. The absorption of radiation emitted by natural radioactivity sources in the air was measured on Earth. It was soon clear that the origin of the ionisation in high altitudes could not be the Earth. Initially, the radioactivity of air itself was considered as the likely source of the ionisation. However, it was demonstrated that the level of radiation (ionisation rate) was too large to be accounted for by radioactivity in the air [YS85]. In 1911 and 1912, Victor Francis Hess studied the ionisation of the air during several balloon flights. He discovered, that in contrast to his expectations, the discharging rate of an electroscope decreases only for the first several hundred meters in altitude; for higher altitudes it increases again. He showed that at a height of 1800 m the ionisation reaches the same level as at the Earth's surface. At 5000 m, he observed an ionisation level which was much higher than at sea level. At this time it was clear that Hess had discovered a new type of radiation coming from space, now termed *cosmic*

rays today [YS85, Hes11, Hes12].
By experimenting with cosmic rays, many new elementary particles, from the positron to the strange quark, were discovered during the following years. With the development of new techniques to artificially produce and accelerate particles, the era of accelerator physics began. Charged particles like electrons and protons are accelerated to very high energies up to several TeV producing new particles in interactions.
In the intervening years, many more particles have been discovered, ever larger particle accelerators and detectors were built to examine their properties. With the development of the Standard Model in the early 1970s, the understanding of elementary particles has reached a high level. For some time cosmic ray physics stood in the shadow of accelerator and particle physics.
However, many open questions remain, which can be answered only by experiments measuring high energy particles. Nature provides us with a beam of high energy particles beyond the reach of man-made accelerators – the cosmic rays.

2.2 The spectrum of Cosmic Rays

The ionisation measured by Victor Hess originated from secondary particles, which are produced in interactions of high energy particles with air molecules in the upper atmosphere. These primary cosmic rays are produced in distant sources such as supernovae or stars. The interaction of a primary cosmic ray particle produces a cascade of secondary particles, which develops in the atmosphere. Figure 2.1 summarises the current understanding of the development of air-showers. First hadronic interactions dominate the shower producing $\pi^0, \pi^\pm, K^0, K^\pm$ and other hadrons. The decay of these hadrons produces a large number of leptons and photons.

Since the discovery of the cosmic rays, a variety of detectors have measured their spectrum with high precision. Cosmic rays arrive isotropically from all directions at the Earth and their flux can be described by a power law: $dN/dE \propto E^{-\gamma}$. Above 10^9 eV, the primary cosmic rays consist of roughly 98% of nuclei accompanied by 2% of leptons. The flux of nuclei consists of about 87 % of protons, 12 % α particles and 1 % of heavier nuclei [Lon92]. Neutrinos, which also arrive in large numbers at the Earth, interact rarely with matter and are not contained in this calculation. Apart from neutrinos from the sun and from one supernova (SN 1987 A), no extraterrestrial neutrinos have yet been detected [Sup98].
The primary cosmic ray energy spectrum, beginning at a few hundred GeV, is displayed in figure 2.2. While the low energy evolution is governed by the Earth's magnetic field and solar modulation, blocking particles with energies

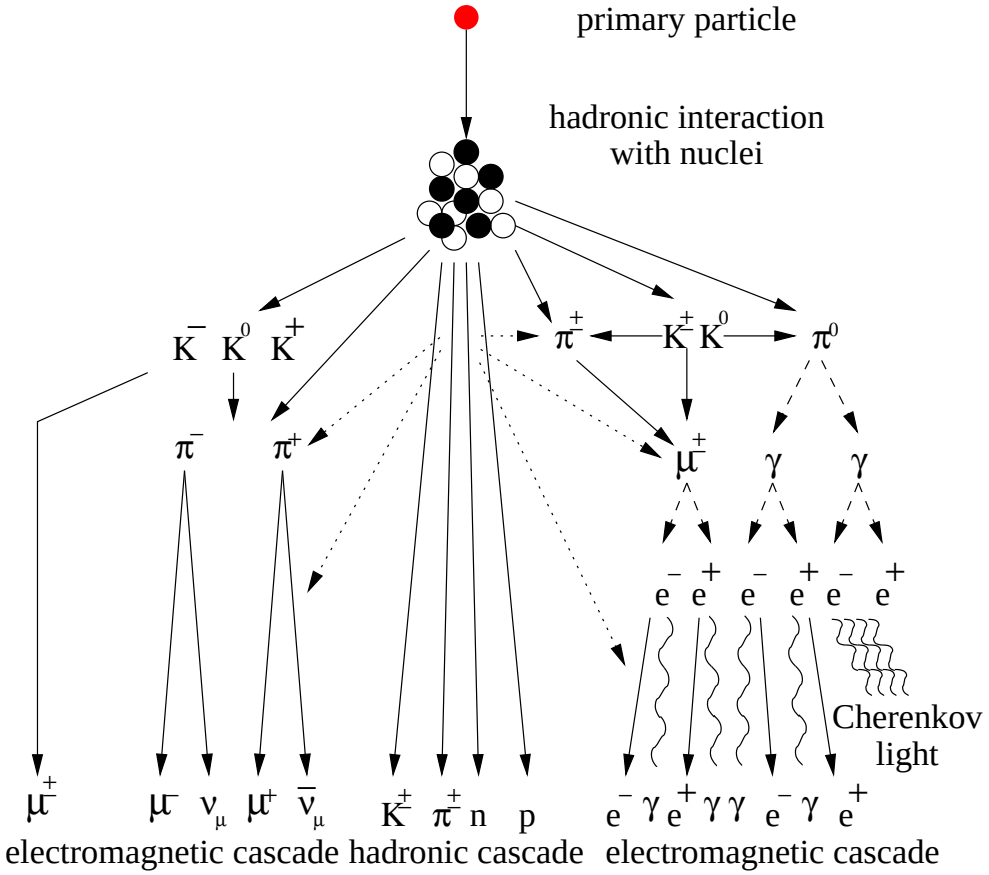

Figure 2.1: A Cosmic Ray shower in the atmosphere.

below several GeV [Gai90], the high energy spectrum reaches energies up to 10^{20} eV.
The behaviour of the spectral index γ is interesting, being stable over several orders of magnitudes but showing two major breakpoints, where γ changes significantly. At 10^{15} eV the spectral index changes from $\gamma = 2.63 \pm 0.02(\text{stat.}) \pm 0.09(\text{syst.})$ to $\gamma = 3.10 \pm 0.10(\text{stat.}) \pm 0.10(\text{syst.})$ and decreases again above 10^{19} eV [Wie98]. The break region around 10^{15} eV is called the knee, while the region around 10^{19} eV is called the ankle [Gai90].
The power law behaviour of the cosmic ray spectrum can be explained by the *diffuse shock acceleration* model. Particles are accelerated in successive processes gaining in each step a small amount of energy, proportional to the actual energy of the particle, in every step. With a constant probability to escape, this process results a power law energy spectrum. However there is a certain maximum energy for a specific accelerating system that depends on the average magnetic field and the size of the object [Gai90].

It is expected that a supernova shock wave can produce the cosmic ray

spectrum up to 10^{19} eV. The breakpoint at the knee can be explained by the *leaky box model*: Particles produced in local sources are confined by the average galactic magnetic field to the local galaxy, with a certain small probability they can escape from the galaxy. The mean time of residence in the leaky box, until the particle escapes, can be estimated as $\tau_{\text{esc}} = 2 \cdot 10^7$ years [Gai90].
At a certain energy the gyro-radius of the particle exceeds the radius of the galaxy and the particles escape from the confined galaxy. For energies above 10^{15} eV, the particles are no longer confined to the galaxy, lowering significantly the flux at higher energies.

Acceleration to higher energies above the ankle up to 10^{20} eV, can possibly be explained by processes in *Active Galactic Nuclei AGN*.
Several different mechanisms can accelerate particles in the most luminous sources. The understanding of these mechanisms is an important point in particle- and astrophysics.
Greisen, Zatsepin and Kuzmin predicted in 1966 an upper limit to the cosmic ray spectrum at $\sim 10^{20}$ eV, which is also referred to as the *Greisen Zatsepin Kuzmin GZK* cutoff. Protons above this cutoff energy are attenuated due to interactions with the CMB, resulting in a loss of energy and producing a Delta resonance,

$$p + \gamma \longrightarrow \Delta^+ \longrightarrow n + \pi \ .$$

The mean free path length for protons with energies above 10^{20} eV is predicted to be about several Mpc only.

In the past years, the knowledge of cosmic rays has increased significantly. However there are still many open questions concerning the cosmic rays of the highest energies around the ankle. Since the origin of cosmic rays is still unknown, an important goal of astronomy is to identify the cosmic ray sources. Furthermore, the acceleration mechanisms that produce particles with the highest energies are still unknown and have to be studied. Due to the low fluxes and limited experimental sensitivities, the energy spectrum of cosmic rays around 10^{20} eV is still uncertain. To answer these important questions, different types of radiation can be used. The next section gives an overview of the particles and their propagation.

2.3 Particle propagation and detection

Figure 2.3 presents an overview of astroparticle physics. The paths of different particles are shown from the source to the detectors on Earth. Detection

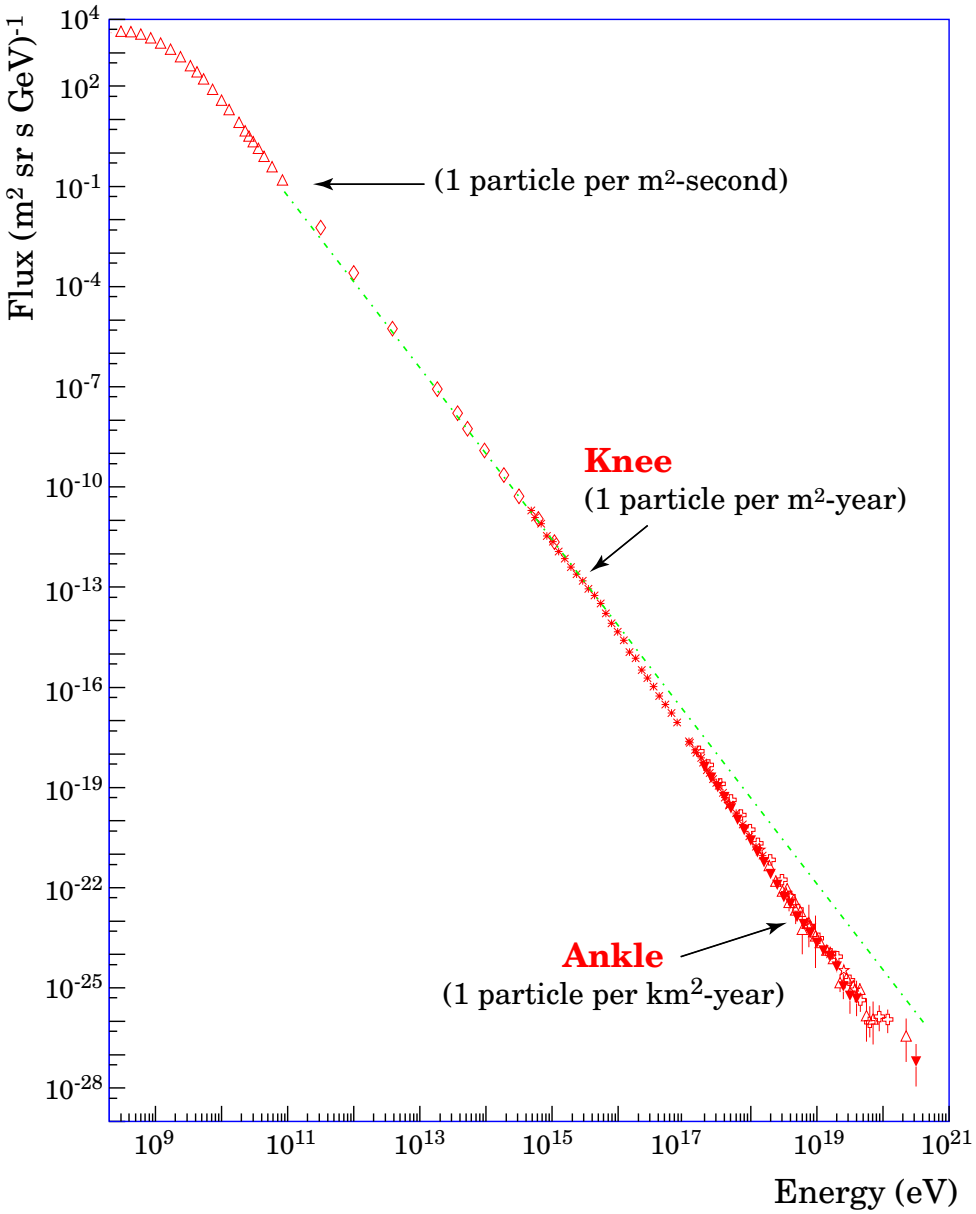

Figure 2.2: The Cosmic Ray Energy spectrum. The major breakpoints, the knee at $\sim 10^{15}$ eV and the ankle at $\sim 10^{19}$ eV, are clearly visible [Kam01].

of each type of radiation has particular advantages and disadvantages as described below.

- **Photons** give mostly information regarding the surface of opaque objects. Furthermore, compact sources are often surrounded by matter or dust clouds, obstructing the path of photons. Thus, it is not possible to

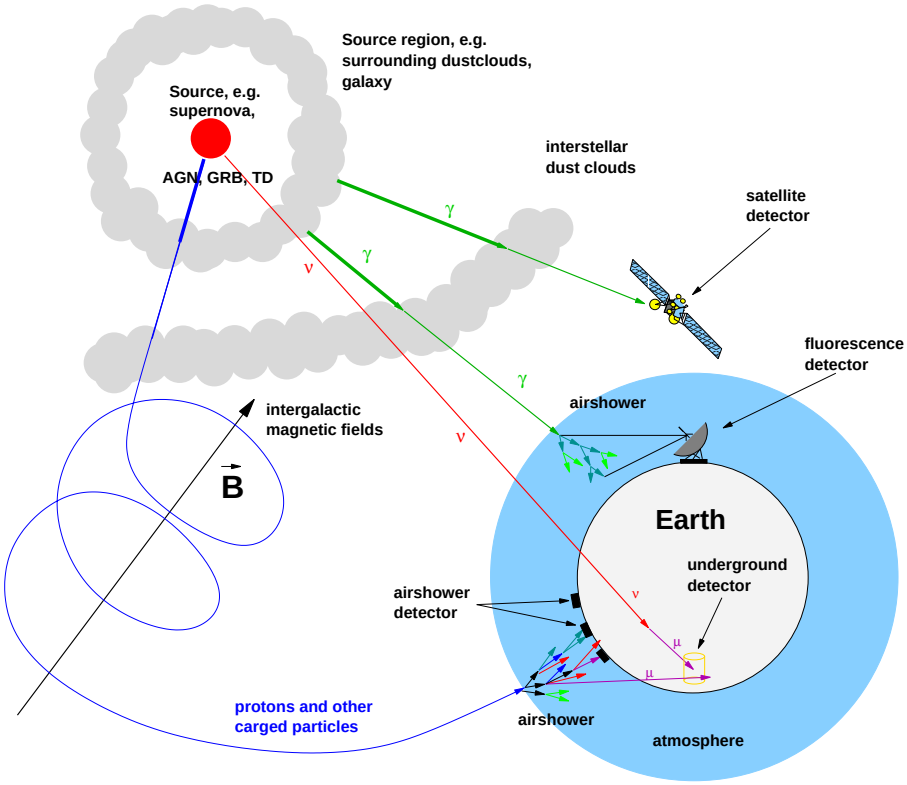

Figure 2.3: Survey of astroparticle physics. Only neutrinos can traverse through dust clouds and are not affected by magnetic fields.

look into the core of the source.

Photons with an energy above $2 \cdot 10^{14}$ eV interact with low energy photons from the *Cosmic Microwave Background CMB* producing an electron – positron pair. Figure 2.4 illustrates the energy dependence of the horizon for interactions with background radiation fields in the Universe including photons produced by the source itself.

$$\gamma + \gamma_{\mathrm{bg}} \longrightarrow e^{+}e^{-}$$

The flux of high energy photons from distant sources is limited by these reactions. The horizon for a 10^{15} eV photon is only about 7 kpc.

- **High energy charged particles** are deflected by interstellar and intergalactic magnetic fields. Therefore, charged particles arrive isotropically at the Earth without any memory of their initial direction. Only particles above 10^{19} eV are fast enough to retain directional information.
  The GZK cutoff limits the flux of high energy protons above 10^{20} eV, as

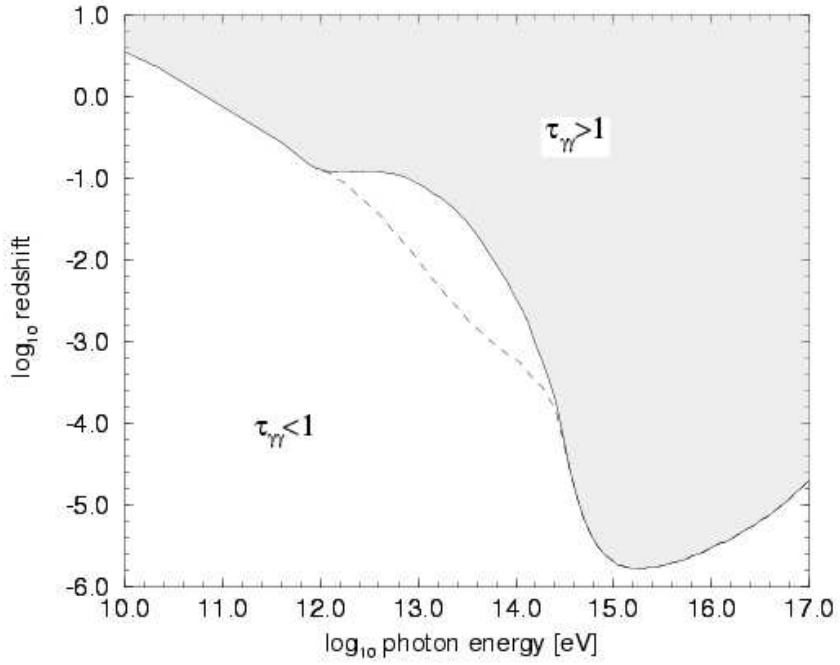

Figure 2.4: The energy dependence of the horizon for gamma astronomy corresponding to optical depth $\tau_{\gamma\gamma} = 1$ assuming $\Omega = 1$, $q_0 = 0.5$ and $h = 0.75$. The dashed line shows a second calculation using a different diffuse background model. The shaded area is not visible for photon astronomy [Man96].

described above. Therefore, only very nearby sources are expected to be seen from Earth [Gre66].

- Free **neutrons** quickly decay to protons with a half-life period of 885.7 ± 0.8 s [Gro04]. From the galactic centre very high energy neutrons above 10^{19} eV are capable of reaching the Earth before decaying. Thus, only a small part of the Universe is visible with neutrons.

- **Neutrinos** interact with matter via weak interactions with extremely small cross sections. In comparison to other kinds of radiation, neutrinos are not affected by dust clouds or magnetic fields and propagate from the source in a straight line. Neutrinos, which are produced in a source can escape from the core of that source.
  Neutrinos have been an exciting subject of physics research since their discovery [R$^+$56]. The experimental discovery of neutrino oscillations with solar and atmospheric neutrinos provides an insight into physics beyond the standard model [SNO02, Sup98].

Neutrinos offer the potential to discover sources which are not visible with other methods and may allow the observation of the active core of a source surrounded by dust shields. However, the small cross sections of neutrino interactions are also a disadvantage, neutrino detectors have to be very large in order to measure a sufficient number of events. Although the detection of neutrinos is difficult, it offers exciting prospects for exploring the Universe.

2.3.1 Neutrino production

Neutrinos have no electrical charge and cannot be accelerated directly, but are produced in the decay of primary accelerated particles. The most important source for high energy neutrinos are weak decays of charged pions (and kaons)

$$\begin{aligned} \pi^+ &\longrightarrow \mu^+ \nu_\mu \longrightarrow e^+ \nu_e \overline{\nu}_\mu \nu_\mu \\ \pi^- &\longrightarrow \mu^- \overline{\nu}_\mu \longrightarrow e^- \overline{\nu}_e \nu_\mu \overline{\nu}_\mu \\ p &\longrightarrow n\, e^+ \nu_e \,. \end{aligned}$$

These pions are produced in hadronic interactions of protons, neutrons and photons. In one scenario, high energy hadrons are accelerated and interact with each other or with photons in the source or the surrounding region:

$$\begin{aligned} p + p &\longrightarrow X + \pi^\pm, \\ p + \gamma &\longrightarrow X + \pi^\pm, \end{aligned}$$

and analogous processes involving neutrons. Thus, in order to produce the neutrinos hadronic interactions are necessary. However, neutrinos can be also produced in decays of heavy particles, e.g. heavy relics from the Early Universe, see section 2.4.3. On the following pages a selection of possible neutrino sources are discussed.

2.4 Possible sources of high energy neutrinos

In this section the most important models for the production of high energy neutrinos are presented. In the subsection 2.4.1 models based on black holes are discussed, while further subsections present supernovae and exotic particles.

2.4.1 Objects with black holes

Some of the most fascinating objects in the Universe are black holes. First, the English astronomer G. Michell considered in 1783 the possibility that a large massive star can attract and even trap light. In 1916, K. Schwarzschild developed a metrics describing the vicinity of a so called black hole. The radius of this object is described by the Schwarzschild - radius R_s

$$R_s = \frac{2GM}{c^2} \ ,$$

where G is the gravitational constant, M is the mass of the black hole and c is the speed of light in a vacuum. In 1963, R.P. Kerr found a new metrics including the angular momentum of black holes. It turns out that several high luminosity sources in the sky can be explained by assuming a rotating black hole as a central engine [Mir04].

Active Galactic Nuclei

Active Galactic Nuclei AGN are one of the most powerful sources in the Universe. Today's standard theory is that they can be described by assuming a galaxy with a super-massive black hole in the centre ($M \approx 10^6 - 10^8 M_\odot$)[1]. The black hole attracts matter from the surrounding host galaxy forming an accretion disk around the black hole [CMU95, Man97]. It is suspected that most galaxies have a massive black hole in their centre. However to produce the observed luminosity, the accretion rate has to be sufficiently high. In the middle of figure 2.5 a sketch of an AGN is shown. Perpendicular to the accretion disk, the AGN develops two relativistic jets which can be observed due to their radio emission. The accretion disk emits at UV and optical wavelengths, while the torus, which surrounds the centre, emits infrared light.

Due to their anisotropic structure, AGN show different appearances depending on the orientation with respect to the observer. An AGN with a jet pointing directly towards the Earth is observed as a *blazar*; these objects vary rapidly in intensity. An AGN observed perpendicular to the jets will be seen as a *radio galaxy*. In this case the end points of the jets are visible due to radio emission, while the core emits UV and optical light. There are further classifications according to the galaxy type, features of the emission spectrum and the intensity in radio emission, which are not discussed here. The production of neutrinos in AGN is of particular interest to neutrino astrophysics. The neutrino fluxes are tested assuming either a *diffuse flux* arriving isotropically from all directions or as a flux from certain point sources. Since the emission

[1] $M_\odot$ is the mass of our sun.

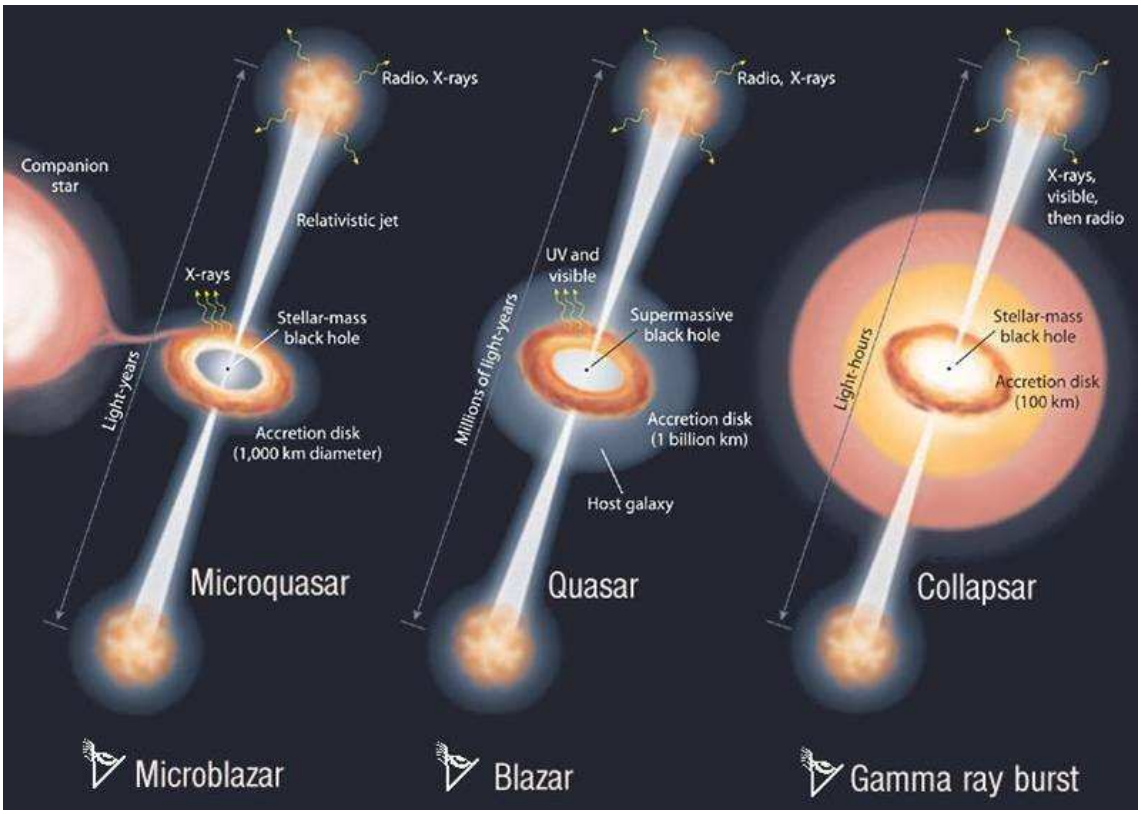

Figure 2.5: There are three different sources in the sky, which can be explained by the same mechanism, a black hole accreting matter. Inter alia, they differ in size and lifetime [Mir04]. The supermassive black hole in the center of the middle object is called an *Active Galactic Nuclei AGN*. An AGN pointing with its jet towards the observer is termed *Blazar*, while an AGN seen from the side is considered as a *Quasar*.

processes inside the AGN are not fully understood, it is important to know whether the acceleration of hadrons or leptons is the dominant source of the observed radiation. In hadronic processes it is expected that a significant neutrino flux will be produced due to pion decay. Therefore, the detection of an AGN as extraterrestrial neutrino source would help to understand the character of the sources.

In figure 2.6, various extragalactic neutrino flux predictions and experimental limits are shown. The models presented are listed below:

1. In the model of Becker, Biermann and Rhode (BBR) [JKB], flat and steep spectrum sources are considered using the jet-disk symbiosis model by Falcke et al. [FB95].

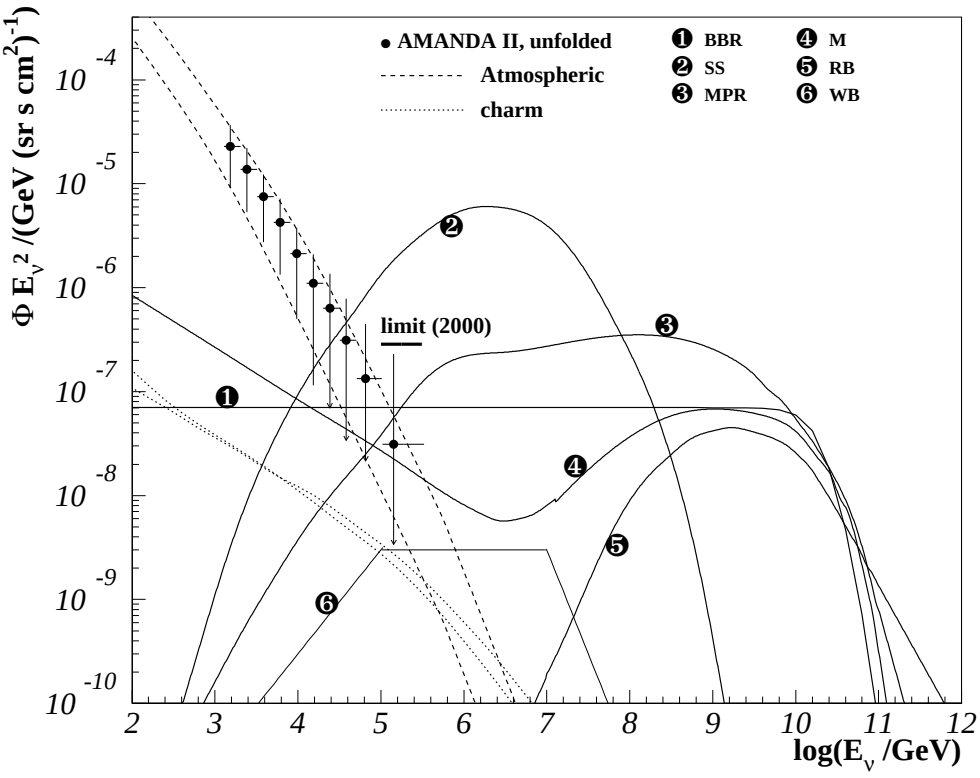

Figure 2.6: Muon neutrino fluxes - (1): $p\,p$ interactions; Becker, Biermann and Rhode (BBR) [JKB]; (2): Stecker and Salamon, AGN neutrino flux ($p\,\gamma$) [SS96]; (3): $p\,\gamma$ interactions, Mannheim, Protheroe, Rachen (MPR) [MPR01]; (4): Mannheim (M) [Man95], , $p\,\gamma$ in blazar and $p\,p$ in its host galaxy; (5): Rachen & Biermann (RB) [RB93], $p\,\gamma$; (6): Waxman and Bahcall (WB) [WB99]; Prompt neutrinos from GRBs, assuming that these are the sources producing the Cosmic Ray spectrum at $E > 10^{19}$ eV. The dashed lines give the atmospheric flux prediction from light baryon (i.e. no charm contribution) decay (horizontal and vertical) [VZ80, H$^+$95]. Dotted lines indicate the atmospheric spectrum from heavy baryons, i.e. baryons having also charm quarks as constituents. Amanda limit and data for muon neutrinos [M$^+$].

2. The quasar model by Stecker and Salamon (SS) [SS96] is normalised to the X-ray flux of AGN sources. It can be excluded by current AMANDA limits [M$^+$].

3. Mannheim, Protheroe and Rachen (MPR) [MPR01] predict a maximum flux from blazar sources for $p\,\gamma$ interactions.

4. The model by Mannheim (M) [Man95] includes $p\,\gamma$ interactions in blazars as well as protons from blazars interacting with protons in the host galaxy

of the active nuclei.

5. Rachen and Biermann (RB) [RB93] calculate the number of neutrinos from AGN proton interactions with the CMB.

6. Waxman and Bahcall (WB) [WB99] give an estimation of the GRB neutrino flux, assuming that the Cosmic Ray spectrum at $E > 10^{19}$ eV results from these sources.

The dashed lines in the figure represent the conventional atmospheric neutrinos, as calculated by Volkova [VZ80]. The upper line gives the horizontal neutrino flux while the lower line is the calculation for a vertical flux component. The neutrino flux from baryons with charm contribution in the atmosphere is indicated as dotted lines. Heavy baryons decay faster than light ones ($\tau \sim 10^{-12}$ s compared to τ(conventional)$\sim 10^{-8}$ s). The spectrum is therefore flatter because the particles including charm quarks do not interact with nucleons in the atmosphere. The model is given by [MRS03], the two lines indicate the uncertainties in the model. The atmospheric neutrino spectrum as observed by AMANDA is shown in figure 2.6. The data points are calculated unfolding the detector spectrum [M$^+$,Gee03]. The limit is calculated from the data.

Gamma Ray Bursts

Gamma Ray Bursts GRBs were first detected by a satellite in 1967 as a high intensity pulse of γ–rays. Due to the short time scales, of about ms to 100 s, it is expected that the source is a very small and compact object. GRBs are distributed homogeneously over the sky without any clustering in the galactic plane indicating that they originate from extragalactic sources. Today, a rate of about 670 GRB per year is detected [P$^+$99].
Two classes of GRBs have been detected, long enduring GRBs with a time scale ≥ 2 s and short GRBs with a shorter timescale. An afterglow detected at optical and radio wavelengths has been measured from long enduring GRBs. This made it possible to measure the distance to these objects using the redshift.
Since their luminosity is very high reaching up to 10^{52} erg, it is likely that GRBs are objects, which emit most of the radiation in jets. The currently favoured model is the *Fireball model FM*, which explains the development of the jets, but does not specify the engine of the GRB. However, an object including a black hole is likely [Lon92].
A possible scenario for a GRB is shown in figure 2.5. Due to the lack of hydrogen and helium emission lines in the spectrum, it is assumed that GRB are related to SN type Ic. The progenitors of these supernovae are massive rotating binaries with little hydrogen and helium. A GRB on March 29th 2003 was

identified as SN 2003 dh, by an unambiguous SN light bump in the spectra of the GRB [S$^+$03].
It is expected that due to the strong shockwave protons are accelerated, creating pions, which decay to large numbers of neutrinos. Thus, GRBs are also an interesting prospective source for neutrino astronomy. Figure 2.6 includes the flux of prompt neutrinos as predicted by the model of Waxman and Bahcall [WB99].

So far, no significant neutrino flux from GRBs has been detected.

Microquasars

Microquasars are galactic objects and have a similar structure as AGN. A stellar mass black hole or a neutron star is at the centre of the Microquasar [Mir04]. Since the centre is not visible, this question can only be inferred indirectly. The order of magnitude of the jet length is of the order of light years and the diameter of the accretion disk is about 1000 km. Figure 2.5 (left side) shows a Microquasar.
Due to their small size the fluxes of microblazars show a high variability [Mir04].

2.4.2 Supernovae

A star is formed by a hydrogen gas cloud, which contracts until fusion reactions start, due to the high temperature and pressure in the core of the cloud. The interactions of the hydrogen nuclei produce helium. During this period, the star is in equilibrium since the pressure caused by the fusion reaction balances the gravitational force.
If the temperature and mass of the star is high enough, it contracts again until the next fusion reaction is started. Depending on the mass further fusion reactions start until iron is produced. Since iron has the highest binding energy per nucleon, a further fusion reaction will not gain more energy and the star will finally collapse. During the collapse, which is called a *supernova SN* explosion, the pressure inside the star will become very high initiating a process called deleptonisation:

$$e^- + p \longrightarrow n + \nu_e \,,$$

resulting in a (proto-) neutron star and a large neutrino burst. Although neutrinos have a small cross section, they are trapped in the dense core of the supernova and diffuse out over a time interval of several seconds [A$^+$02c,B$^+$91]. In addition, the material will heat up during contraction, photons produce

e^+e^--pairs which are mostly reabsorbed due to the high density. However via the following process they can produce neutrinos:

$$e^+ + e^- \longrightarrow \nu_\alpha + \bar{\nu}_\alpha \,,$$

which can escape from the centre of the supernova. In this process all neutrino flavors ($\alpha = e, \mu, \tau$) are produced in equal numbers [A$^+$02c].
It is expected that from a distant supernova, the neutrino signal will be visible minutes to hours before the optical signal. Therefore a neutrino detector observing this signal can be used as an early warning system for a supernova in the future. The neutrinos emitted during the hot phase of the supernova have an energy between 11 MeV and 25 MeV [A$^+$02c].
In addition, high energy cosmic rays can be produced by shock acceleration in supernovae shells. The accelerated particles can decay producing further high energy neutrinos.

2.4.3 Weakly Interacting Massive Particles

An interesting problem in astrophysics is the quest for *dark matter*. Due to observations of the velocity distribution of stars and galaxies, it has been found that the mass of the visible matter is not sufficient to explain the dynamics of galaxies and galaxy clusters. Apart from baryons and neutrinos, there must be a large amount of invisible dark matter [Lon92].
So far, the nature of dark matter has not been identified. It is predicted that a large portion of this matter is non-baryonic. Thus, the search for dark matter concentrates on the so called *Weakly Interacting Massive Particles WIMPs*. One possible scenario is that WIMPs are neutralinos, which are particles predicted by supersymmetric extensions to the standard model of particle physics. Their mass is predicted to be in the TeV range.
WIMPs interact with surrounding matter only weakly or gravitationally. When traversing through matter, WIMPs can lose energy by elastic scattering off nucleons. Due to their large mass, WIMPs can be gravitationally trapped in large massive objects like the stars or planets and accumulate in the centre, where interactions between WIMPS may become more likely. They can annihilate pairwise producing neutrinos [A$^+$02a].
One possibility of detecting WIMPs is the detection of an excess neutrino signal from the centre of the Earth or the sun [Eks04].

Taking into account the variety of possible sources presented on the preceeding pages, a possible neutrino detector has to satisfy certain requirements:

- A sufficient angular resolution $< 5^\circ$ in order to identify point sources accurately. This can only be achieved with good time resolution.

- A high energy resolution is necessary to measure the diffuse spectrum of neutrinos. Thus, the dynamic range of the detector has to be large.
- The sensitivity should be high at low energies to enable detection of supernovae and WIMPs.

3

The AMANDA experiment

The advantage of neutrino astronomy, the fact that neutrinos travel unhindered through matter and magnetic fields, also results in the technical challenge of their detection. The detector volume has to be very large in order to obtain a sufficient number of events.
The aim of the *Antarctic Muon and Neutrino Detector Array AMANDA* is to detect high energy neutrinos. AMANDA is a Čerenkov detector, which uses the deep ice at the geographical South Pole as active volume. The detector consists of 19 chains – strings – of light sensors located between 1150 and 2350 m below the ice surface. Fig. 3.1 shows the detector in its present configuration. The sensors were deployed between November 1995 and February 2000. The detector has been chosen to be located at $\sim$ 1500 m below the surface, because of the clear and bubble free ice at this depth. In addition, the ice overburden shields the detector from high energy muons produced by cosmic ray interactions above the detector.
This section contains a short survey of the detector and its operation.

3.1 Neutrino detection technique

Neutrinos interact in matter via charged current reactions, producing a secondary charged lepton ℓ accompanied by a hadronic cascade, where the lepton takes a large fraction of the energy:

$$\nu_\ell + \text{nucleon} \longrightarrow \ell + \text{hadronic cascade}\,.$$

The lepton loses its energy via continuous ionisation and stochastic processes, e.g. bremsstrahlung, pair production, nuclear interactions and Compton scattering.

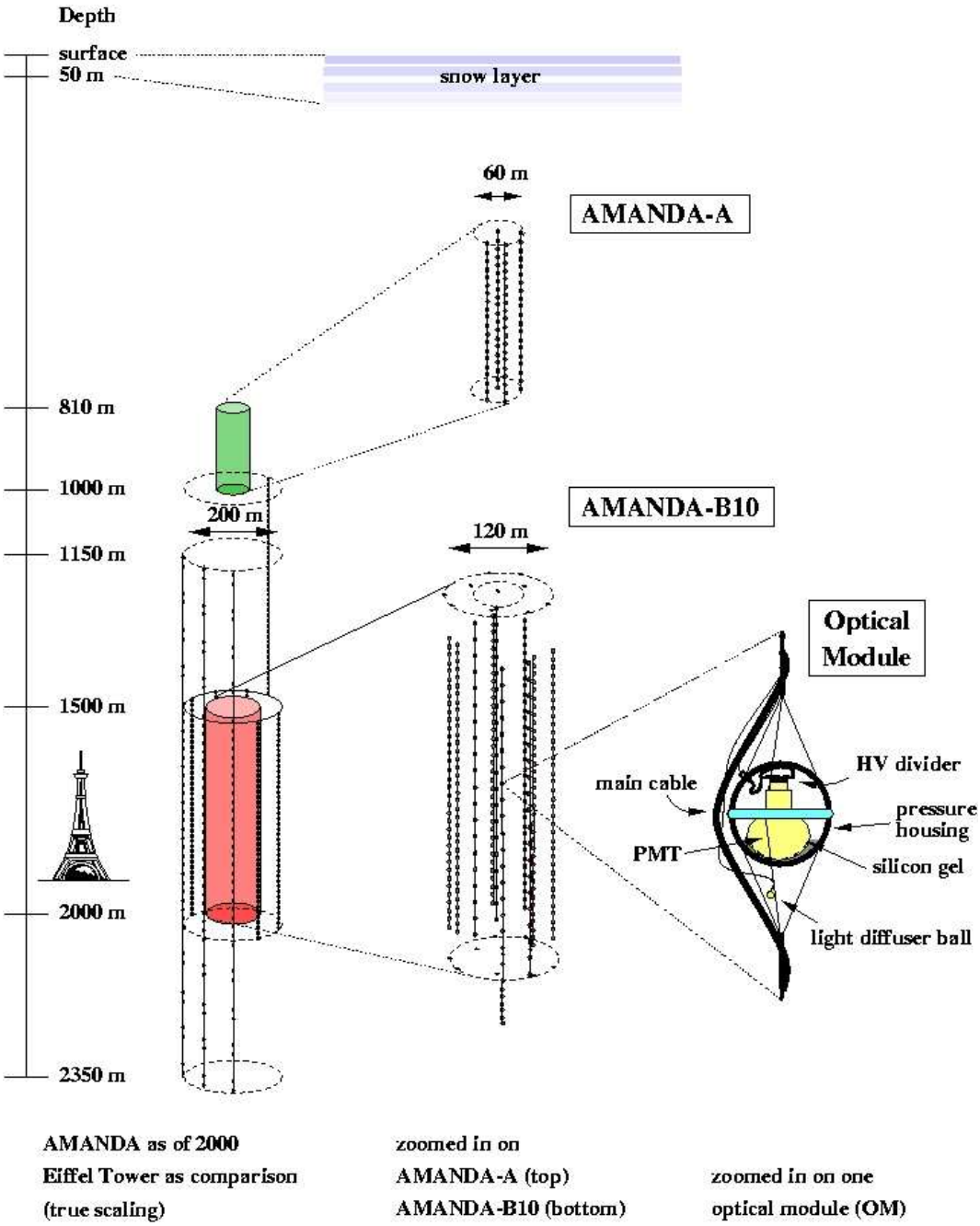

Figure 3.1: The AMANDA detector since 2000.

If the velocity of a charged particle exceeds the velocity of light in the surrounding matter, a cone of Čerenkov light is emitted. The angle θ_c of the Čerenkov light emission with respect to the particle direction is determined

by the velocity of the particle v and the refractive index of the surrounding matter n and is described by

$$\cos\theta_c = \frac{1}{\beta n}$$

with $\beta = v/c$. The number of photons N per unit length x and wavelength interval $d\lambda$ due to Čerenkov radiation is given by [Leo94]

$$\frac{d^2N}{dxd\lambda} = \frac{2\pi\alpha z^2}{\lambda^2}\left(1 - \frac{1}{\beta^2 n^2}\right), \tag{3.1}$$

where, α is the fine structure constant and z is the particle charge. The detection of charged particles e.g. electrons, muons and taus can be achieved using water or ice as the detector medium, which are transparent for Čerenkov photons. The emitted light can be detected using photomultipliers with high gain.

Figure 3.2 shows the detection of particles with light sensors.

Muons lose their energy continuously via ionisation. Beyond several hundred GeV stochastic processes, e.g. bremsstrahlung, nuclear intractions and pair production, become more important. The muon energy loss can be described by

$$-\frac{dE}{dx} = a(E) + b(E)\cdot E\,, \tag{3.2}$$

where $a(E)$ represents the muon energy loss by ionisation and $b(E)$ describes the energy loss by stochastic processes. The parameters a and b vary only slowly with energy [Gro04]. In addition, a cone of Čerenkov will be observed in transparent matter, which is displayed in figure 3.2(a). While the energy loss due to Čerenkov is negligible, the Čerenkov cone allows the particles to be detected and their trajectory to be measured. For particle which travel far enough in the detector, it is also possible to detect the particle direction.

The mean deviation angle Ψ between the direction of the incident ν_μ and the produced muon is expected to be [LM00]

$$\Psi = 0.7^\circ \cdot \frac{E_\nu}{\mathrm{TeV}}^{-0.7}.$$

In contrast, electrons lose energy very quickly in a small volume and produce a short cascade of secondary particles, which is displayed in figure 3.2(b).

The tau produced by a ν_τ have short decay lengths causing a similar cascade. Taus with an energy above 10^{15} eV will produce a unique signature in the detector – two bright cascades connected with a short track, a so called “double bang”. These high energy tau-induced cascades can be distinguished from

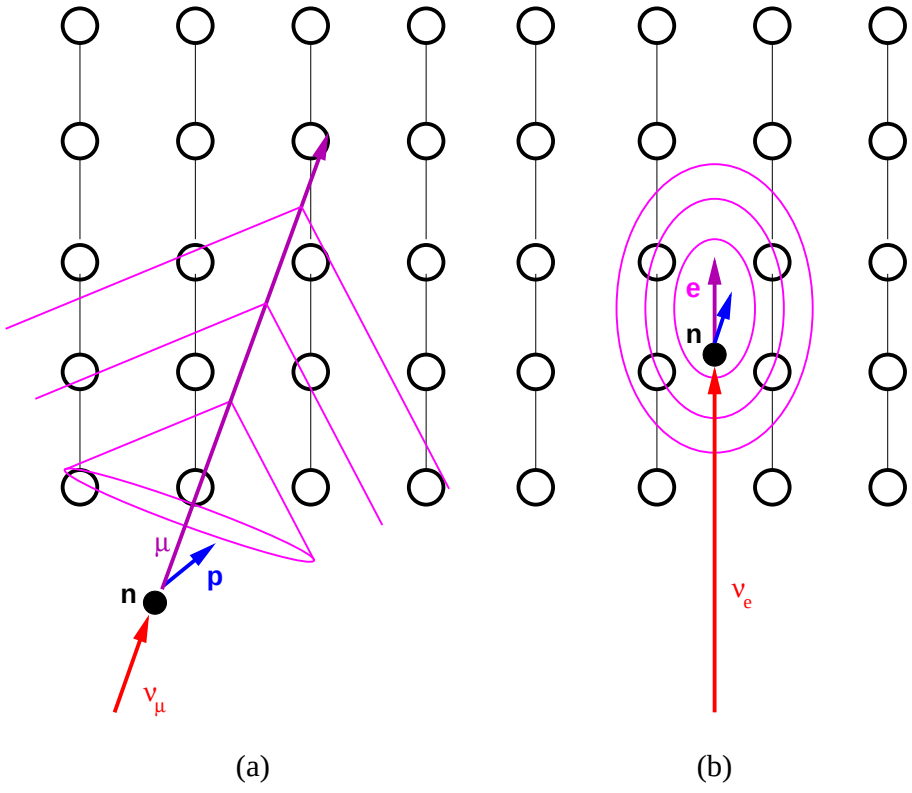

Figure 3.2: Detection principle of charged particles with light sensors using the Čerenkov technique. A muon-neutrino produces a Čerenkov cone (a), while electron-neutrinos produce a short cascade (b).

electron-induced cascades [W$^+$02, JL95].
Reconstruction of particle trajectories and energies is performed taking into account the arrival times and the number of photons in each photomultiplier. The background for underground Čerenkov detectors mainly consists of atmospheric muons, which are produced by cosmic ray showers in the atmosphere. While hadrons, photons and electrons, produced by cosmic rays, are absorbed in the atmosphere or at the surface, muons can travel larger distances in matter until they either decay directly or come to rest and decay. Only neutrinos can traverse the entire Earth. For neutrinos of energy below 10^{15} eV, the Earth is nearly transparent. Therefore, muons with directions originating from below the horizon are considered as secondary particles produced by the interaction of a neutrino. Thus, the Earth acts as a filter. The ratio between background atmospheric muons and neutrino induced muons near the detector is about 10^6 [A$^+$02b].
For neutrinos with an energy above 10^{16} eV, which are referred to as *Ultra High Energy neutrinos UHE*, the Earth becomes progressively more opaque.

The relation between the transmission coefficient for neutrinos traversing the Earth and the zenith angle is shown in figure 3.3. Therefore, for identification of UHE neutrinos, different methods must be employed. Muons from these neutrinos mostly reach the detector from close to the horizon [H$^+$01].

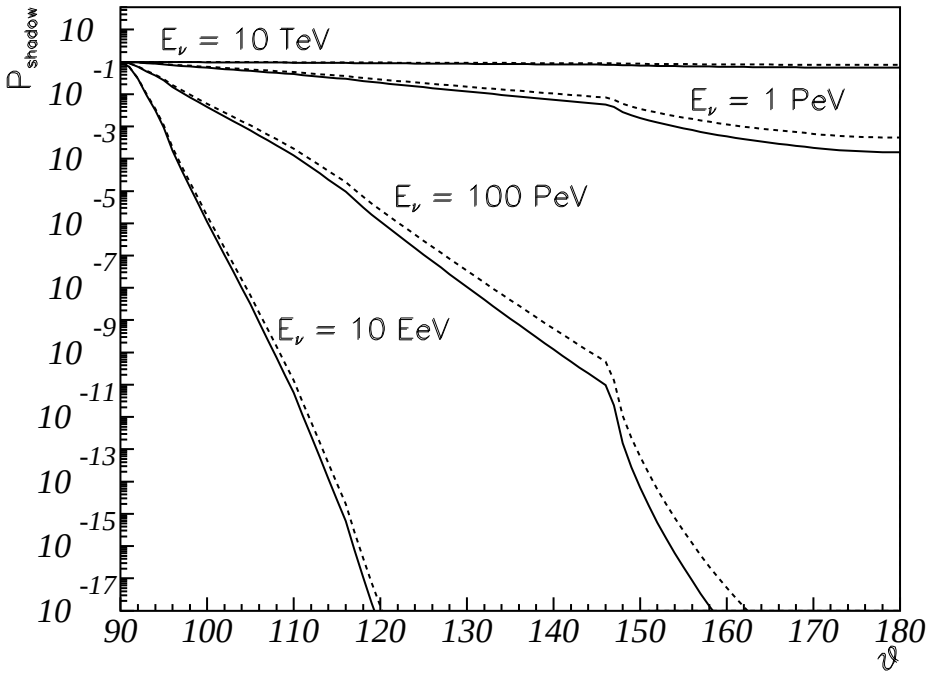

Figure 3.3: Transmission coefficient for neutrinos when traversing the Earth [Bec04].

3.1.1 Ice properties

Table 3.1 shows a comparison of the optical properties of ice and water. The absorption length in ice is much larger than in water. In contrast, the effective scattering length[1] in water is much larger than in ice. Due to the large back-

[1]The effective scattering length Λ_{eff} was originally defined by optical oceanographers to account for the mean scattering angle θ_{scatt}: $\Lambda_{\text{eff}} = \frac{\Lambda_{\text{scatt}}}{1 - \langle cos(\theta_{\text{scatt}}) \rangle}$

ground radiation produced by bioluminescence and K^{40} decay in salt-water, ice as detector material proves to be a good choice.

Property	Water	Ice
absorption length	50 - 60 m	90 - 100 m
effective scattering length	2000 m	25 - 30 m

Table 3.1: Optical properties in water and ice. [LM00]

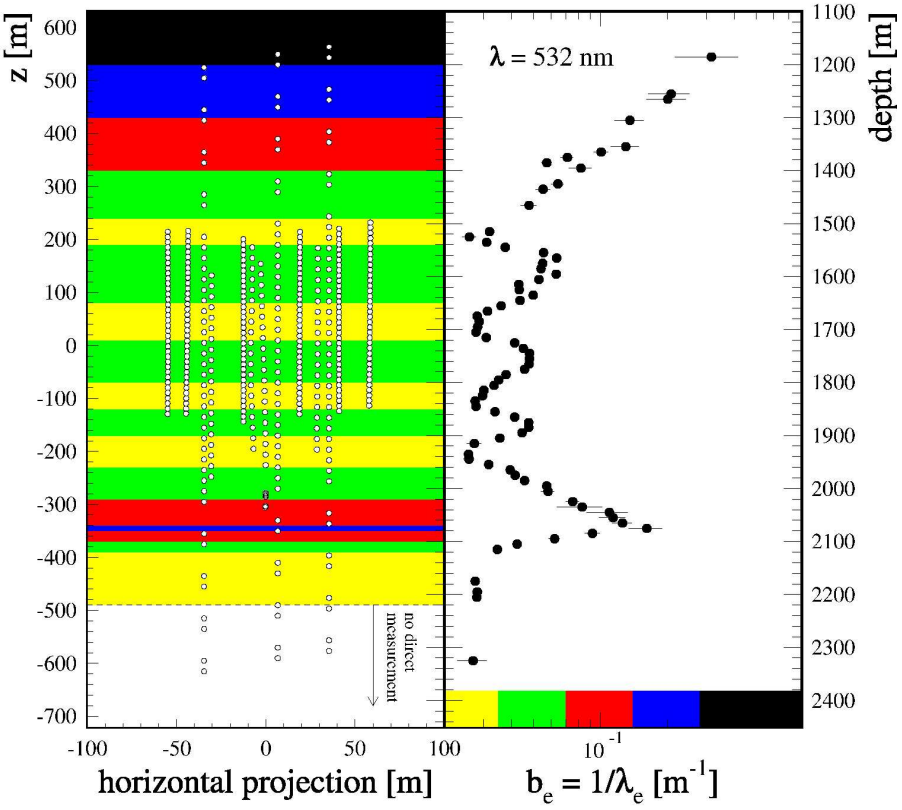

Figure 3.4: The depth dependence of the scattering length. The center of the detector corresponds to a depth of about 1700 m.

The Antarctic ice formed in several thousand years influenced by weather conditions and volcanic erruptions. Fluctuations of the dust density in the atmosphere caused dust layers in the ice. The depth dependence of the

scattering length for Antarctic ice at the South Pole is displayed in figure 3.4. The scattering increases with dust concentration. Above 1400 m scattering is dominated by air bubbles in the ice, while below the air bubbles disappear and scattering is mostly caused by dust layers. These dust layers are also observed in AMANDA data by an increased hit probabilty of OMs at the depth of these dust layers [W+99].
It was shown that in depths between 1400 m and 2300 m the ice properties are suitable for a neutrino observatory [W+99].

3.2 The *MuonDaq*

In total AMANDA is composed of 677 *Optical Modules OMs*, which are displayed in figure 3.1 (right). The OMs contain a *photomultiplier tube PMT* and the high voltage electronics consisting of a voltage divider. The AMANDA detector is equipped with 8 inch PMTs (5912-2) from Hamamatsu with 14 dynodes. The PMTs are connected to the pressure glass sphere with a silicon gel and can be operated at a high gain of about $1 \cdot 10^9$. In addition most of the OMs are equipped with a nylon ball serving as diffuser, which is connected via an optical fibre to the surface and is used for calibration purposes.
This section presents an overview of the current AMANDA *Data Acquisition DAQ* system, which is referred to as the *MuonDaq*. The reconstruction uses the arrival time and the number of photons represented by every PMT pulse from each OM.

Strings	transmission technology	number of modules	deployment
1 - 4	coaxial cables	80	1995/96
5 - 10	twisted pair	222	1996/97
11 - 13	optical fibre	123	1997/98
14 - 19	optical fibre	252	1999/2000

Table 3.2: Comparison of the AMANDA strings [W+01].

Table 3.2 lists the different building stages of AMANDA. Construction can only take place during the Antarctic summer season from November to February.
The analogue PMT signals are transmitted to the ice surface. Taking into account new experience gained and new developments in electronics, various techniques have been used for the analogue transmission over the years.

The first four strings deployed in the Antarctic season 1995/96 used coaxial cables for signal transmission. The detector was enlarged in the following season 1996/97 by 6 strings equipped with twisted pair cables. This detector is called AMANDA B10. It turned out that the twisted pair cables are more vulnerable to electromagnetic interference between cables - called *cross talk* - and electromagnetic radiation from outside the detector.
PMT pulses have a typical length of about 20 ns for a *single photon electron 1.p.e.* pulse. Due to dispersion, a PMT pulse sent along a 2 km electrical cable will widen significantly from 20 ns to about 200 ns [A$^+$00]. Thus, the resolution in pulse separation is of the order of ∼200 ns.
Finally, the recent enlargements of the detector were perfomed using optical fibres for signal transmission. The electrical signal current of the PMT drives a *light emitting diode LED* or a laser diode, which is located in the OM. The light signal is coupled into an optical fibre, which transmits the signal to the surface, where a *Positive intrinsic Negative* diode PiN converts it again into an electrical signal. For these OMs the pulse resolution is much better. Two pulses arriving with a time delay of more than 20 ns can be resolved. The detector in its present configuration is called AMANDA II [W$^+$01].

A schematic overview of the current *MuonDaq*, is shown in figure 3.5. The electronics at the surface are located in the MAPO[2] laboratory, located at a distance of 800 m from the geographical South Pole.
The analogue signal from the OM (1) is amplified at the surface. Electrical signals are decoupled from the cable and amplified by the so called *Swedish Amplifiers SWAMP* (2), while the optical signals are converted back into an electrical signals and amplified by the *Optical Receiver Board ORB* (3). While the ORBs are equipped with two prompt and one delayed output, the SWAMPs provide three prompt and one delayed output. The amplification for the prompt output and the delayed output is different. In most cases, the amplification for the prompt output is larger. The delay for the delayed output is $\sim 2\mu$s.

One of the prompt outputs is connected to a discriminator (4), which is integrated in the AMANDA trigger system. A further output of the discriminator to a to a *Time to Digital Converters TDC* [3] (5) measuring the arrival time and pulse length of the PMT pulses with a time resolution of $\sim$ 1ns. More precisely, the TDCs measure the positive and negative crossing point of the signal at a certain threshold, as determined by the discriminator. The TDCs are capable of storing up to 16 edges. Assuming one leading and trailing edge for each pulse, the TDC will record 8 complete pulses. However, since in some cases one of the edge can be lost, the place in the memory can be filled with an additional leading edge of a further pulse. Additional pulses are lost. This limits the dynamic range and the sensitivity of AMANDA especially for *Ultra High Energy UHE* events, since high energy events may contain more than

[2]named after **M**artin **A**. **PO**merantz, the first astronomer working in Antarctica
[3]The currently used TDC is a V693 from CAEN with 128 channels (VME module).

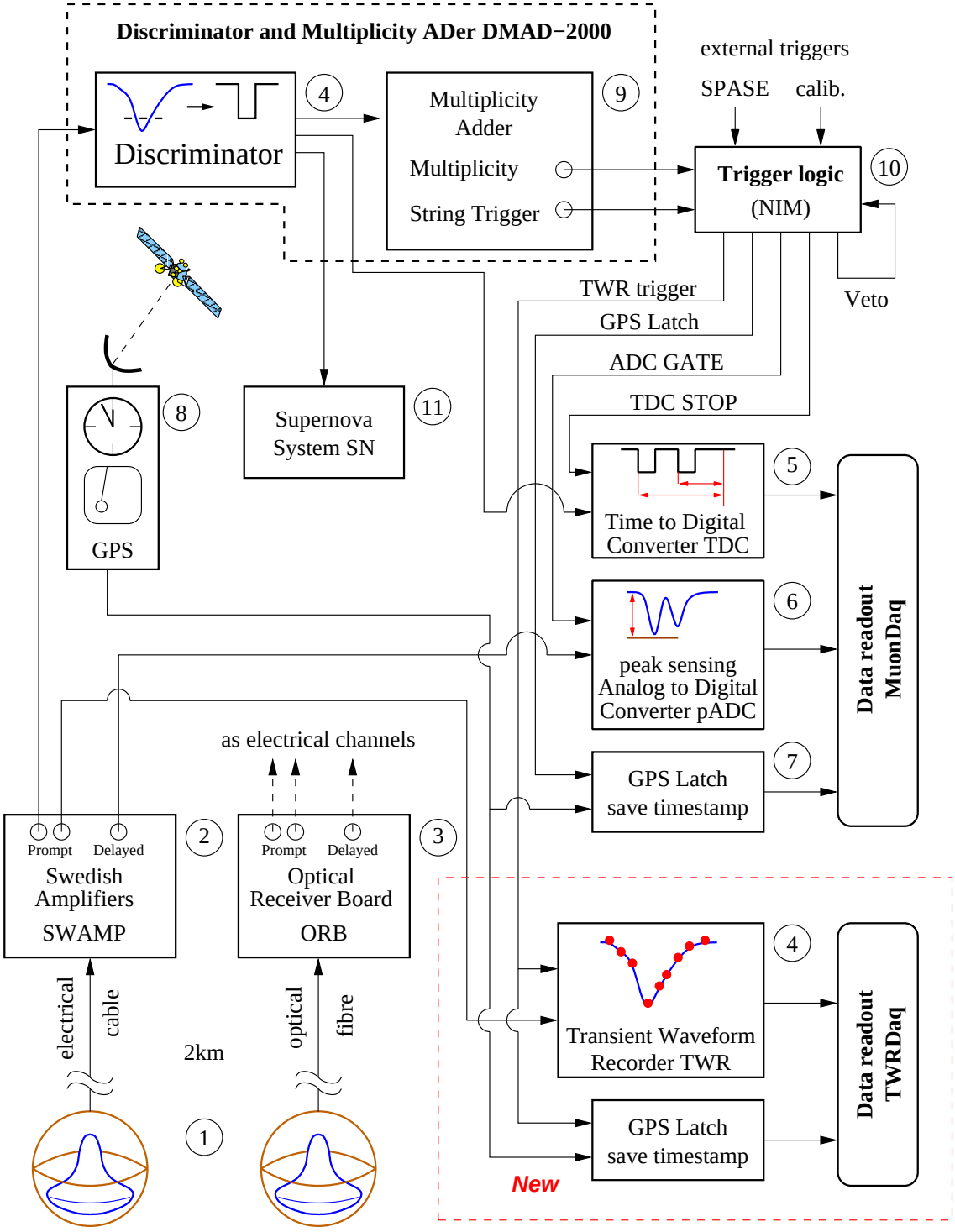

Figure 3.5: The current AMANDA DAQ system - MuonDaq

eight individual pulses in many PMTs.
The delayed output of the SWAMPs and the ORBs is connected to a *peak sensing Analog to Digital Converter pADC* [4] (6), which samples the maximum pulse amplitude in a time window of about 6 μs around the trigger time. Thus, for OMs with more than one pulse per event the association between TDC times of a pulse and pADC pulse amplitude is ambiguous.
The global trigger time is recorded by a *GPS Latch* (7), which is described in detail in section 4.2.1. The GPS Latch is synchronised with the central AMANDA GPS clock (8).
The *Discriminator and Multiplicity ADder DMAD-2000* is composed of discriminators (4) and the Multiplicity Adder unit (9), providing several trigger signals with different multiplicity thresholds. AMANDA uses a multiplicity trigger with a sliding time window of 2.5 μs. The DMAD requests $M \geq$ hit OMs within the time window. Currently, the threshold is set to $M = 24$. The DMAD also provides an advanced local coincidence trigger called the *string trigger*, which is sensitive to coincidences within a single string.
An additional trigger logic (10) consisting of various NIM modules is used to produce the final trigger signals, which start the TDC, pADC and GPS Latch and data readout. This trigger logic uses the trigger signals from the DMAD and additional external triggers, e.g. an external trigger from the *South Pole Air Shower Experiment SPASE* and calibration triggers.
As described in section 2.4.2, a supernova will produce many neutrinos with an energy of about 10^7 eV, which produce short tracks of lengths of about 10 cm. Since the signals from these short tracks will not produce coincidences, the multiplicity trigger is not able to detect a supernova. Nevertheless, the number of arriving neutrinos is very large and will affect the signal rate of each PMT in the detector. A system of scalers monitors the noise rate of each PMT and searches for an enhancement in the full detector in certain time slices. This so called Supernova System (11) is directly connected to the discriminators [A$^+$02c].
The dead time of the MuonDaq is currently dominated by the dead time of the readout system. The deadtime amounts to 2.2 ms [Sch02] representing about 15 % of the events. The multiplicity trigger threshold (M=24) has been chosen to compromise between high energy and low energy efficiency. If the multiplicity threshold is too low, the efficiency for low energy events with a small number of participating OMs is high, but the probability for losing a high energy event is high. Vice versa, a too high multiplicity threshold results in a high efficiency for high energy events and a low efficiency for low energy events.

[4] The 7164 Peak-Sense Analog-to-Digital Converter from Philips with a 12 bit resolution and a voltage range of 4.096 V is used.

3.3 Calibration

3.3.1 Time calibration

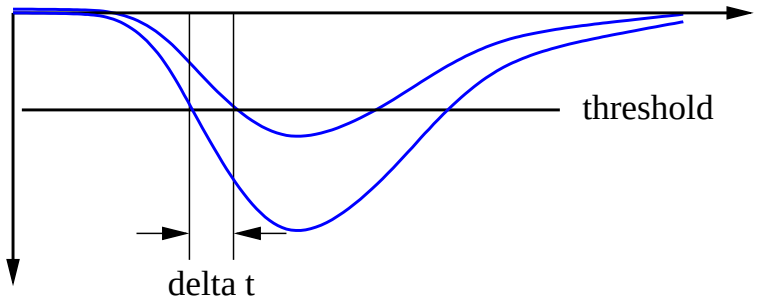

Figure 3.6: Time slewing due to fixed threshold.

About 2 km of cable separate the OMs from the readout electronics at the ice surface. In order to achieve sufficient timing resolution for reconstruction, the arrival times of the pulses must be corrected for the time offset t_0. These offsets are measured by sending light pulses from a YAG laser[5] to a nylon ball located below every OM. This ball serves as a light diffuser [A$^+$00].
With an *Optical Time Domain Reflectometer* the propagation time of the light pulse down to the ball can be determined accurately. The light pulses propagate a short distance through the ice and enter the PMT. By measuring the arrival time of the arriving PMT pulses at the surface, the time delay t_0 can be measured [A$^+$00].
An additional time-slewing appears due to the fixed discriminator threshold and the dispersion of the pulses in the cable. The time-slewing is illustrated in figure 3.6. A small pulse exceeds the discriminator threshold later than a large pulse causing a systematic time shift. It was found that the time-slewing correction can be described as $\alpha/\sqrt{\text{pADC}}$, where α is a constant for each channel. This procedure is termed α-calibration.
The parameter α can be determined by the arrival time distribution displayed in figure 3.7. A linear regression yields the value of the constant. The relative time-shift between a laser pulse and the crossing of the discriminator threshold versus $1/\sqrt{\text{pADC}}$ can be approximated by a linear function. The crossing of the Y-axis gives the time offset t_0.
The complete time correction applied can be written as

$$t_{\text{true}} = t_{\text{measured}} - t_0 - \alpha/\sqrt{\text{pADC}}\,. \tag{3.3}$$

[5]Yttrium, Aluminium and Garnet laser. This term usually refers to an laser with a wavelength of 532 nm. In fact it should be Nd (neodymium) YAG but Nd is usually omitted. The name describes components of the synthetic gemstone used in the laser.

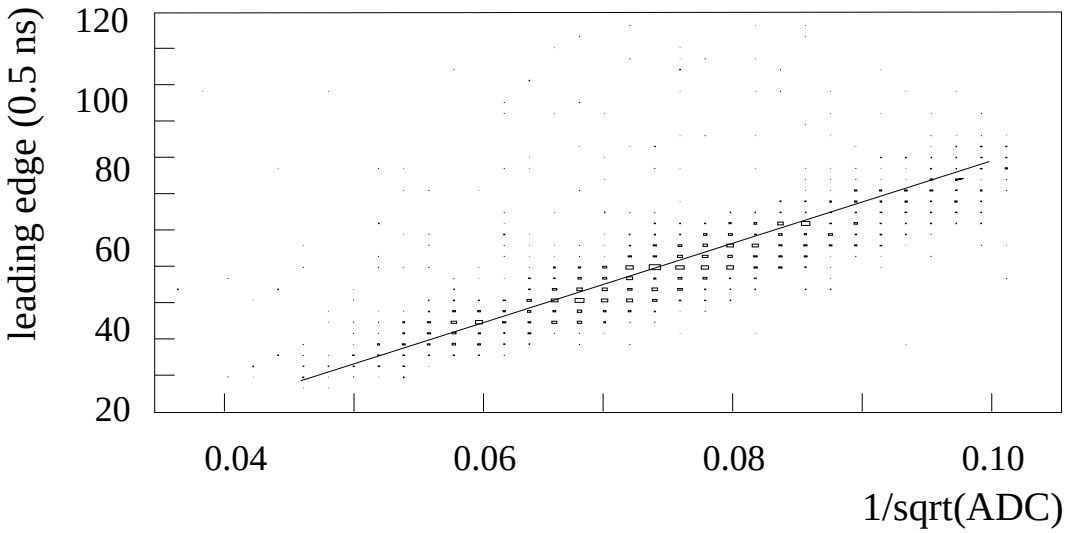

Figure 3.7: Relative time shift between a laser calibration pulse from the surface and the crossing time of the signal over the discriminator threshold versus $1/\sqrt{\text{pADC}}$ [A$^+$00].

with the true arrival time t_{true}, the arrival time measured at the surface t_{measured}, the time delay due to cable transit times t_0 and the measured pADC value representing the pulse amplitude. Applying this technique a time resolution between 4 ns and 7 ns can be achieved [A$^+$00].

3.3.2 pADC calibration

The number of detected photons is an important piece of information. It is expected that N photons arriving at almost the same time result in a PMT pulse with an amplitude N times larger than a single photon pulse amplitude. Since most of the PMT pulses are single photon pulses, the size of a single photon amplitude can be extracted from the pADC spectrum.

Figure 3.8 shows the distribution of pADC values for one channel. The single photon bump is visible. The mean pulse amplitude for a single photon is determined by a fit. The number of photons contained in a pulse is determined by dividing the measured pADC value by the fitted value for a single photon. For larger pulses containing several photons, the number of photons can be underestimated if some of the photons arrive with a time delay. The maxima of the single photon pulses will not match exactly in time, resulting in a wider pulse with a smaller amplitude. In these cases, the integrated pulse rather than the pulse amplitude would be a better measure for the number of photons.

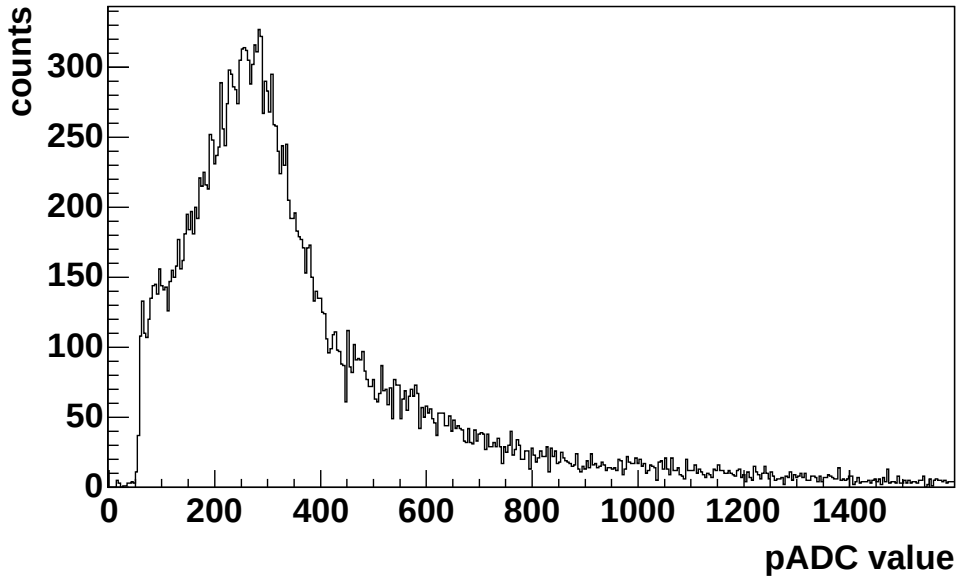

Figure 3.8: The distribution of pADC values for OM 15.

3.4 Reconstruction

The analysis of the data from AMANDA mainly focuses on track reconstruction and extraction of the particle energy. A good survey of the reconstruction algorithms is found in [A+04a].

3.4.1 Track reconstruction

Particle tracks are reconstructed using a maximum likelihood method, based on *probability density functions p.d.f.* of the arrival time of individual photons.
Assuming that a particle with energy E_0 traverses the detector on a track

$$\vec{\mathbf{r}}(\mathbf{t}) = \vec{\mathbf{r_0}} + c_{\text{vac}}(t - t_0) \cdot \hat{\mathbf{p}}\,, \tag{3.4}$$

in the direction defined by the unity vector $\hat{\mathbf{p}}$, with nearly the vacuum velocity of light c_{vac}, the arrival time t_{geo} of an unscattered photon is given by,

$$t_{\text{geo}} = t_0 + \frac{\hat{\mathbf{p}}(\vec{\mathbf{r}}_\mathbf{i} - \vec{\mathbf{r}}_\mathbf{0}) + d\tan\theta_c}{c_{\text{vac}}},$$

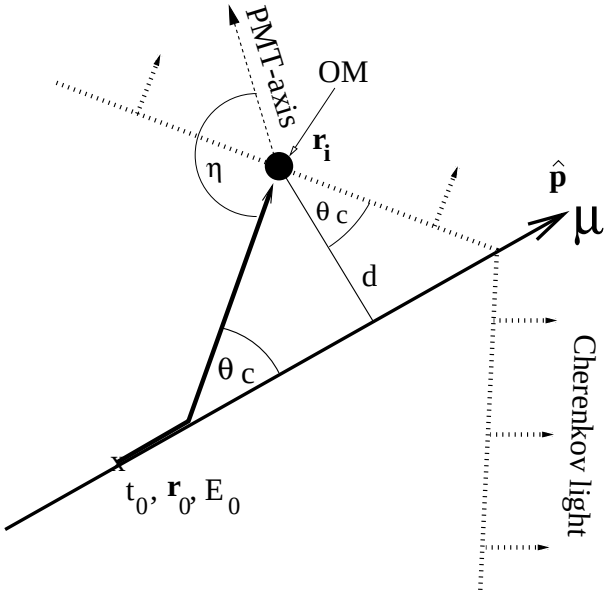

Figure 3.9: Cherenkov cone: definition of track parameters.

where $\vec{\mathbf{r}}_\mathbf{i}$ is pointing to the OM$_i$ and $\vec{\mathbf{r}}_\mathbf{0}$ defines the point, where the Čerenkov photon is emitted. The delay between the expected arrival time as calculated from a chosen track and the measured arrival time in a single OM is labelled *time residual*: $t_{\text{res}} = t_{\text{hit}} - t_{\text{geo}}$. A schematic overview of the track geometry is given in figure 3.9.
The Likelihood function is defined as

$$\mathcal{L}(\mathbf{x}|\vec{\mathbf{r}}_\mathbf{0}, t_0, \hat{\mathbf{p}}, E_0) = \prod_i p(x_i|\vec{\mathbf{r}}_\mathbf{0}, t_0, \hat{\mathbf{p}}, E_0) \tag{3.5}$$

where x_i describes all information delivered from AMANDA, i.e. arrival time t_i, pADC value pADC$_i$ and the time over threshold TOT$_i$ of the OM$_i$. The p.d.f.

$$p(x_i|\vec{\mathbf{r}}_\mathbf{0}, t_0, \hat{\mathbf{p}}, E_0) \tag{3.6}$$

represents the probability density of observing a photon at time t_i in OM$_i$ for a track with parameters $(\vec{\mathbf{r}}_\mathbf{0}, t_0, \hat{\mathbf{p}}, E_0)$. The p.d.f. is a function depending not only on the track parameters, but also on the PMT orientation and the ice properties. Currently, a simple parameterised p.d.f. based on a homogeneous ice model is used. This function, named *Pandel function*, uses a small set of empirical parameters and the absorption length λ_a. The Pandel function used by the reconstruction program has been obtained from simulated data [K$^+$97]. The likelihood function used in the analysis presented in this thesis is a *Single Photo Electron SPE* function, which considers every arriving photon to be

independent of the other photons and describes only single photon pulses.
In order to achieve accurate track reconstruction, a hit-cleaning procedure is applied to the data. During the hit-cleaning OMs with a high noise rate are excluded from the reconstruction. In addition, noise hits and after-pulses are also excluded from the analysis. In principle, hits that are isolated in time and space are considered as noise hits [A$^+$04a]. Afterpulses are late pulses inherent to PMTs and do not contain any extra information[6].
Since the reconstruction only accounts for the arrival times and the number of photons in the OM, these values have to be calibrated from the raw data. During calibration the arrival times are corrected for the offset due to cable length and for time slewing due to different signal amplitude as described in section 3.3. The number of photons is determined by dividing the measured pADC amplitude by the expected size of a single photon pulse.
The reconstruction algorithm has to be initialised by a first guess track as a seed for the maximum likelihood fit. In this thesis, the direct walk algorithm was used. Data selection of, e.g. upgoing tracks, can be accomplished based on the first guess algorithm [A$^+$04a].
The final track parameters are found by maximising the likelihood function. So far, track reconstruction is often performed using the first pulse. In addition, several new techniques have been developed to use the information from pulses following the first pulse. A detailed review of muon track reconstruction in AMANDA is given in [A$^+$04a]. The reconstruction of cascades follows a similar procedure and is described in [A$^+$03] and will not be discussed here in detail.
One algorithm which allows the separation of cascade and track like events, is the "tensor of inertia fit": All hit OMs are weighted with their measured pADC value and considered as virtual mass points in a volume. The tensor of inertia calculated from this virtual mass distribution has three main axes corresponding to the eigenvalues. While for a cascade the three axes have about equal size, one value will exceed the other values for a track.
However, the accuracy for track reconstruction is low for a single cascade, because the Čerenkov light appears as a bright, spherical distribution in the detector, which is illustrated in figure 3.2.

3.4.2 Energy reconstruction

While the track reconstruction is based mainly on the accurate arrival times of the PMT pulses, the energy reconstruction also relies on the number of

[6]One possible cause for after-pulses are residual gas atoms in the PMT. A fast electron moving from the cathode to the first dynode can ionise an atom. The ionised atom will be accelerated in the electric field between dynode and cathode. When hitting the cathode a number of electrons are ejected from the cathode forming a secondary cascade of pulses which are called after-pulses. The time between the first direct pulses from the photon and the after-pulses and the number of after-pulses are a characteristic for each PMT type [Leo94].

photons. Currently, three different approaches for the energy reconstruction are used [A$^+$04a]:

- The density of emitted photons along the muon track depends on its actual energy. An OM nearby the track without a hit is less probable. The energy can be estimated from the likelihood function taking in account the number of hit OMs and the number of OMs without a hit along the track. The basic idea is that a track of a high energy particle is visible in a larger volume than that of a low energy particle.

- An estimate of the number of photons is given by the pADC values. Employing these values in the likelihood function results in an improved energy resolution. This method is referred to as Full E_{reco}.

- Another method to measure the energy is to use a neural network [Gee03]. This has been performed using several energy dependent input variables. One of these variables is, for example, the number of pulses in all OMs. The determination of the energy spectrum of ν_μ is performed using regularised unfolding based on the work described in [Blo84].
  The energy spectrum of ν_μ was measured from 10^{12} eV up to 10^{14} eV with a high precision, shown in figure 2.6. However, it turned out that the dynamic range of the energy reconstruction is limited for energies above 10^{16} eV by saturation of input variables.

4

The new AMANDA Data Acquisition system TWRDaq

4.1 Motivation for a new DAQ system

It has been demonstrated in [A+01] and [A+00] that AMANDA is a fully functioning neutrino telescope. Nevertheless, some opportunities remain to improve AMANDA's capabilities. The primary objective of AMANDA is to identify astronomical sources of neutrinos. Figure 2.6 shows the measured energy spectrum of atmospheric neutrinos and several predictions of extragalactic neutrino fluxes. It is expected that the extragalactic neutrino flux exceeds the atmospheric neutrino flux above several PeV. Thus, the identification of extragalactic neutrinos is more promising at higher energies. In addition, it has been shown that the effective volume of the AMANDA detector increases with energy [B+01]. The muon energy is correlated to the integrated number of photons in the detector.

The AMANDA detector uses ice as an active medium with non-negligible scattering. The time spread of the PMT pulses due to scattering is larger than the resolution of the pulse separation. Thus, the signal waveform produced by a PMT, can be complex. A typical complex signal waveform of an electrical channel is displayed in figure 4.1. The present AMANDA DAQ system – the MuonDaq – has limited capabilities for these complex waveforms. The main problems and ideas for improvement are outlined in the following points:

- The pADC delivers only one value per channel per event. Thus, the α-calibration is ambiguous for channels with more than one hit and photon counting is not possible. The goal is to utilise all of the information available from the sensors in the ice without losing important information due to such ambiguities.

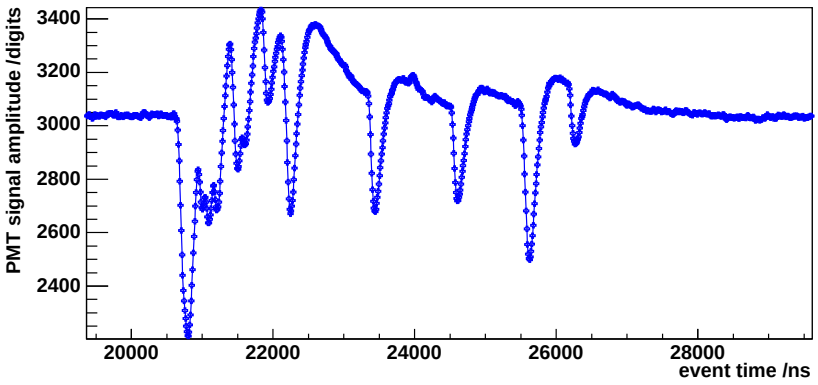

Figure 4.1: A typical complex signal waveform from an electrical channel (OM 283).

- The current procedure to extract the number of photons from the pADC works only if the photons arrive almost at the same time. If not, the pulse amplitudes will be smaller and the pulses wider. This leads to a systematic underestimation of the number of photons for pulses that contain more than one photon.

- The TDC is only capable of measuring up to 16 edges, limiting the dynamic range to 8 pulses. High energy events saturate the TDCs leading to a non optimal resolution for these most interesting events. For the energy and the track reconstruction of UHE particles, it is necessary to have a large dynamic range for the number of photons detected by each PMT. It is required to extend the dynamic range for the number of detected pulses by a factor of ~ 10. Due to more accurate information with respect to the pulse amplitude, the dynamic range for the integrated number of photons, increases even more by a factor of ~ 100. This helps to improve the sensitivity for high energy muons and cascade events. Since ν_τ and ν_e are detected by observing the induced cascades, with a large amount of light in a small volume, the increased dynamic range is crucial.

  The saturation of energy depending variables above a certain energy was demonstrated using the neural network method for energy reconstruction (see section 3.4.2). Figure 4.2 displays the relation between the total number of PMT pulses expected in the detector – N_{hit} – and the simulated muon energy E_μ. The saturation above 10^{16} eV can be clearly seen. Due to the saturation of the input parameter N_{hit}, the dynamic range of the energy reconstruction is likewise limited. Figure 4.3 shows the muon energy E_{reco}, as reconstructed by the neural net, versus the true muon energy E_μ from the simulated data. For this analysis the

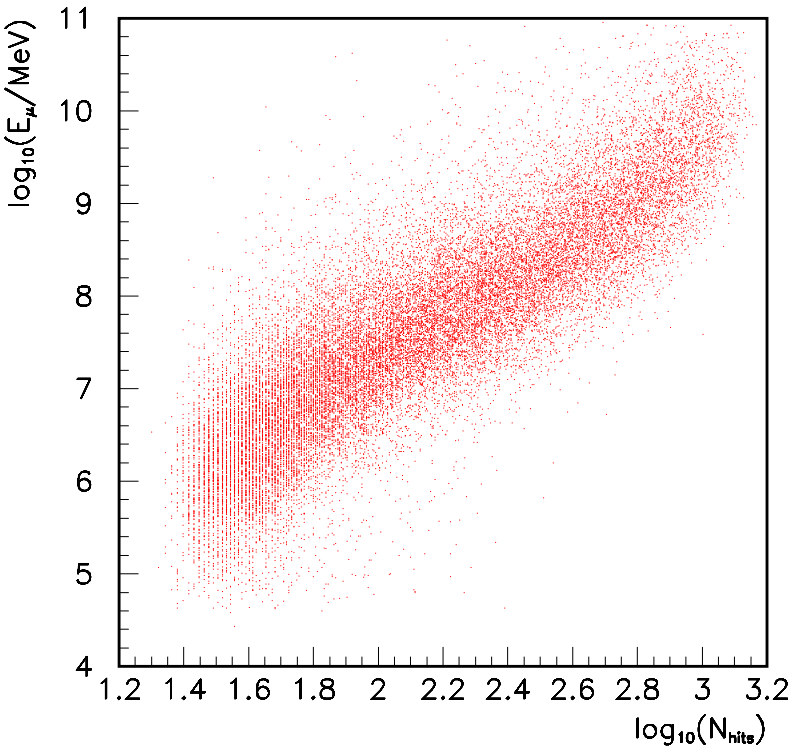

Figure 4.2: Relation between total number of hits and simulated muon energy [Gee03].

neural net is only trained up to $5 \cdot 10^{15}$ eV, where the saturation of the input parameters begins.

- The dead time of the current system is approximately 15 %, resulting in significant loss of data. The dead time is mainly caused by the readout process of the DAQ. It is desired to reduce electronics-induced dead time to a negligible level of less than 1 % using the TWRDaq.

These problems indicate the necessity to install a substantially improved DAQ system. In actual fact, these goals can be achieved using the *Transient Waveform Recorder TWR* [Sys03] – a Flash ADC, which is capable of recording the complete waveform of a PMT. During the Austral summer 2001/2002 a test setup with 48 channels was installed. This test version of the TWRDaq ran stably throughout the winter. A test on the time resolution compared the arrival times of pulses from both DAQ systems. The test showed a good and

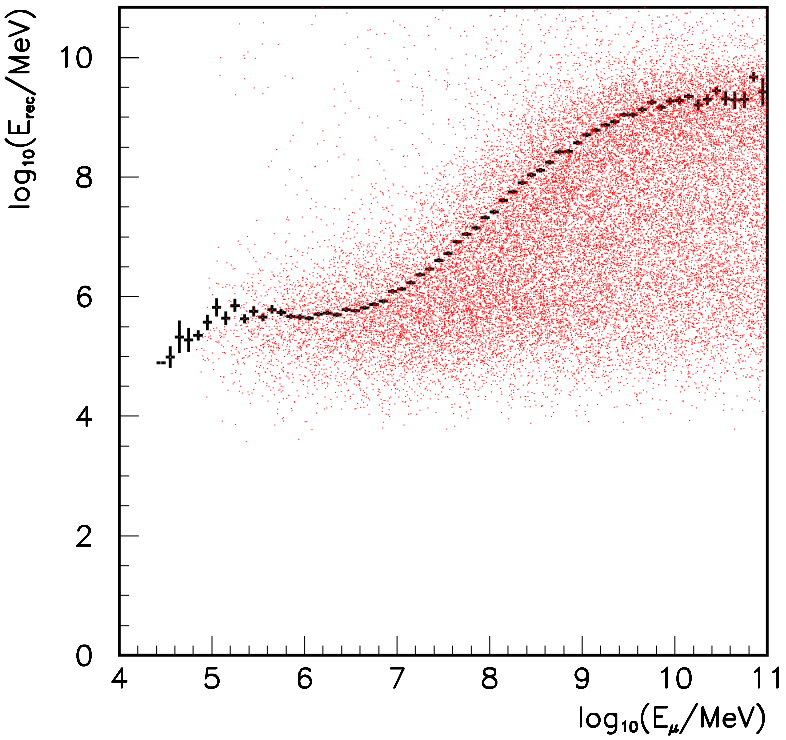

Figure 4.3: Relation between the muon energy E_{reco} as reconstructed by the neural net versus the true muon energy E_μ (simulated data). The dashed line is a fit through the MC data [Gee03].

stable correlation with an accuracy of about 30 ns. Figure 4.4 presents two typical waveforms containing a single photon pulse from an electrical channel (above) and an optical channel (below).

This system was extended in the following summer season 2002/2003 to read almost the entire AMANDA detector. The TWRDaq was running in parallel with the MuonDaq.

Finally, during the following summer season 2003/2004, this system was upgraded again, increasing the readout frequency from 90 Hz to 150 Hz, which allowed the multiplicity threshold to be lowered. The number of connected channels increased to 597 out of 677. Since most of the reliable channels were connected to the systems in 2003 and 2004 a full track reconstruction is possible and can be compared to the MuonDaq.

Both the TWRDaq systems, running in 2003 and 2004, are described in this document. Section 4.2 describes the physical layout of the system, while the

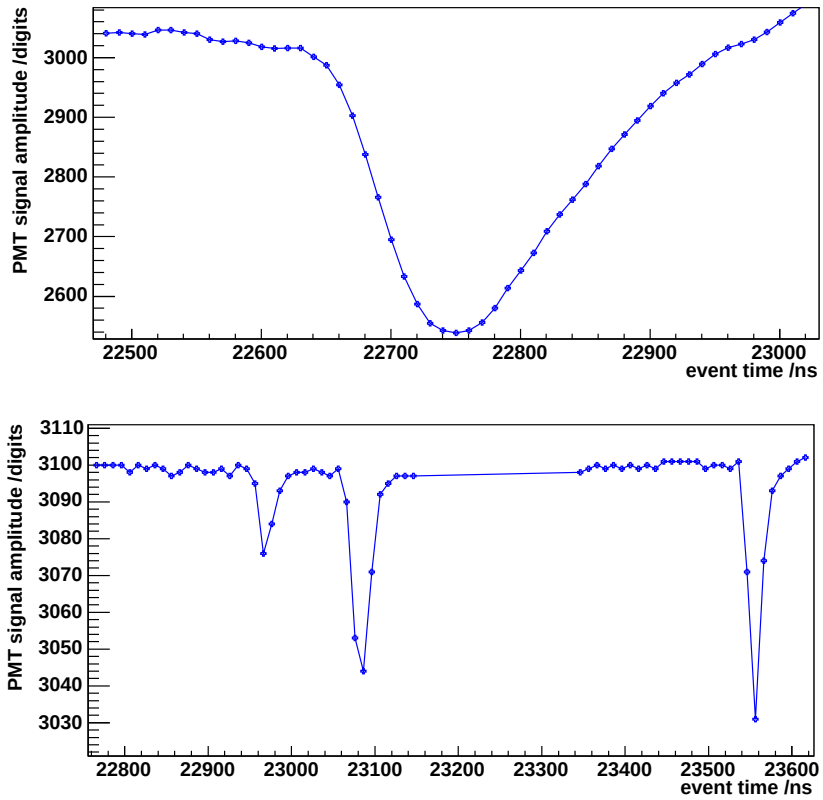

Figure 4.4: Two typical waveforms containing a single photon pulse from an electrical channel (OM 155 – top) and an optical channel (OM 622 – bottom).

following chapters discuss the extraction of information from the waveforms and first experiences regarding the reconstruction using waveforms.

4.2 The TWRDaq system

4.2.1 The Transient Waveform Recorder TWR

The *Transient Waveform Recorder TWR* built by SIS[1] is a 12 bit Flash ADC[2] sampling the incoming signal continuously at a rate of 100 MHz, in a ring buffer of 1024 samples, covering a total time window of 10.24 μs. The TWR is a VME[3] module, which is configured, controled and read out via the VME

[1]Struck Innovative Systems in Hamburg/Germany

[2]A parallel encoding Analog to Digital Converter ADC, sampling the incoming signal by comparing it to a cascade of reference voltages with a certain frequency.

[3]Versa Module Europa

Parameter	value
Number of channels	8
Sampling frequency	100 MHz
Time window	10.24 μs
Samples per waveform	1024
Resolution	12 bit
Voltage Range	5V (+1 V to -4 V)
Memory banks	2
Events per memory bank	128

Table 4.1: Characteristics of the TWR.

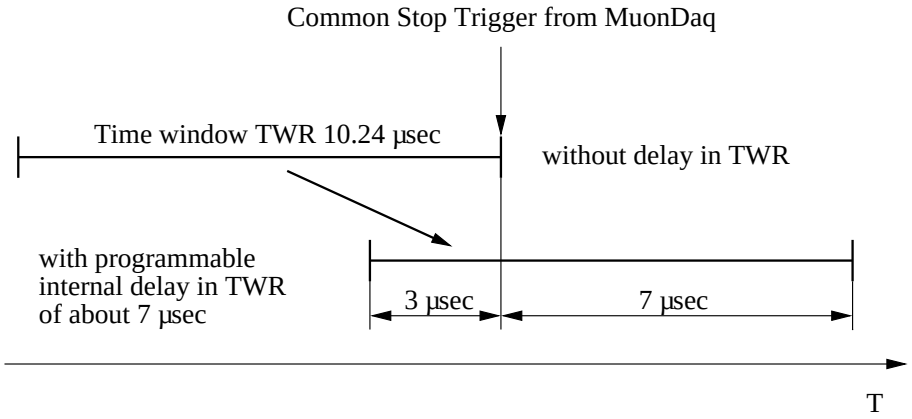

Figure 4.5: Adjustment of the event time interval with respective to the trigger time. An appropriate time window around the trigger time is chosen by delaying the incoming trigger signal.

bus connector. The characteristics of the TWR are summarised in table 4.1. TWR is triggered externally. After each trigger pulse (event-trigger), which serves as a *common stop trigger*, the TWR switches to the next ring buffer and starts sampling the next event. Every TWR contains 8 channels. The TWR has a total voltage range of 5 V reaching from 1 V to -4 V.
In order to measure a certain time window before and after the trigger pulse, the incoming trigger signal is delayed by a programmable number of clock cycles - *trigger delay* - inside the TWR. This is illustrated in figure 4.5. Since the OMs are located at different depths, the incoming signals arrive with different delays at the surface. In order to measure a similar time window for every OM[4] the OMs are distributed to the TWRs according to their signal delays. The individual trigger delay for each TWR is programmed to

[4]Intended are 3 μs before the trigger and 7 μs after the trigger.

accomplish this condition.
For the optical channels of AMANDA the fast output of the *Optical Readout Board ORBs* are used as the input signal, while for the electrical channels the fast output of the SWAMPs is used.
Every TWR has two memory banks each containing 128 events. The TWRs are running in *Autobankswitchmode*, which reduces the dead time of the system by separating the readout and the data-taking process. After starting the sampling, the first memory bank is filled. During read out of the first memory bank, the second memory bank is filled. As long as the readout time for one memory bank is not longer than the time for receiving 128 trigger signals, the data-taking and the readout process are independent and the dead time is negligible. This case is very rare.
The TWR is equipped with a timestamp counter, which allows the measurement of the time between events. In normal mode, it runs at 100 MHz. The frequency can be down-scaled in order to measure larger time differences. The sample clock frequency is not affected by down-scaling the timestamp clock speed. This feature of the TWR enables the TWRDaq to find synchronisation errors between the TWRs by comparing the time differences between adjacent events in different TWRs.
In the current TWRDaq system, the absolute timing information is given by the GPS time (see below), while the timestamp counter of the TWR is only used to test the synchronisation within the present TWRDaq.
Every channel has an independent programmable *detection threshold* th_{det}, which is set during initialisation. While the baseline of the PMT signals is about 0 V, the signal amplitude is negative. The thresholds are adjusted according to the individual noise behaviour of each OM. For a normal event only 6 % - 8 % of the OMs contain a PMT signal below the threshold. Therefore, it is essential to mark waveforms containing a pulse below th_{det} and store this information in a dedicated register. A waveform is *valid*, if at least one of the 1024 values is below th_{det}. During the readout process only these valid waveforms are read out.

The GPS latch GPS2VME

The GPS2VME [Lei03] latch is basically a clock which is synchronised externally by a *Global Positioning System GPS* clock. The synchronisation is done via three electrical signals delivered by the GPS clock, located in the AMANDA counting room. The different signals are listed in table 4.2. The achieved accuracy of the time signal is 150 ns.
The current version of the GPS2VME is a VME module, which is configured and read out using the VME bus. The GPS2VME is triggered by an external trigger signal. For each trigger the GPS2VME latches the actual time infor-

Signal	Description	Frequency
1PPS	Pulse Per Second synchronising begin of second	1 Hz
10MHz	10 MHz clock pulse fine synchronisation pulse	10 MHz
Timestamp	serial timestamp synchronise day, hour, minute	1 Hz

Table 4.2: Signals delivered from the GPS clock to synchronise the GPS2VME module.

mation. This timestamp consists of 4 long-words, the number of seconds of the actual day, the 10 MHz counter of the actual second, an event counter and single bits indicating the stability of the incoming synchronisation signals. The timestamps are stored in a FIFO, which is read out via the VME bus. For more information about the GPS2VME see [Lei03].

Another function of the GPS2VME latch is to produce a trigger veto during emission of strong radio signals[5], which interfere with the data taking process.

The SIS3100 interface and the Digital Signal Processor DSP

To interconnect and control the various remote VME crates of the system, holding the TWRs and the GPS latch, a VME to VME interface is used. A complete VME/VME interface consists of two *VME interface modules SIS3100* and an optical cable with two fibres linking them. In order to connect the PC to the system, a similar PCI/VME interface is used, consisting of a SIS3100 and a *PCI interface card SIS1100* with an optical cable in between. The VME interfaces SIS3100 are used to build a network of VME crates. Some of the SIS3100 contain a *Digital Signal Processor DSP*, which is optimised for processing large amounts of data using fast and simple algorithms.

The DSPs programs are written in assembler and are loaded and started during initialisation. For communication between the TWRDaq software and the DSP, several registers located in the DRAM of the SIS3100 are used.

In addition, the SIS3100 modules in the remote crates provide several programmable NIM[6] input and output registers, which are used to disable the

[5]The *Very Low Frequency VLF* experiment studies the lower ionospheric and mesospheric signatures of charged particle using a radio beacon signal transmitted from South Pole. It turned out that this signal results in a non negligible amount of cross talk in the twisted-pair signal cables of strings 5 to 10 averting normal data taking. The AMANDA trigger has to be blocked during the VLF emission, which take place four times per hour for about 1 minute.

[6]Nuclear Instruments and Methods signal level – logic '1' = -0.8 V, logic '0' = 0 V at 50 Ω termination [Leo94].

trigger signal during initialisation [Sys02].

4.2.2 Trigger logic - Veto logic

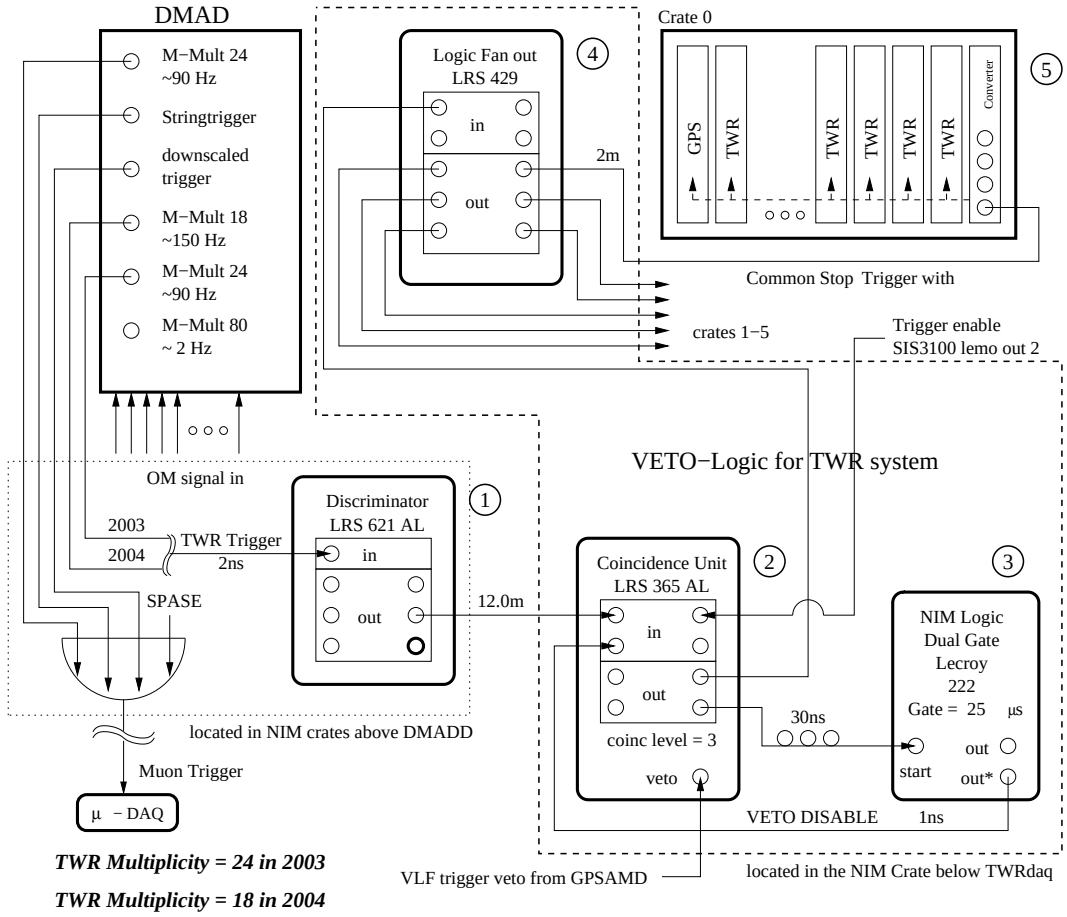

Figure 4.6: Trigger setup.

The current version of the TWRDaq is triggered externally by the trigger logic of the MuonDaq – the DMAD–2000. In 2003 the same multiplicity trigger level as in the MuonDaq was used (i.e. M = 24 hit OMs in a time window of about 2.5 μs with a trigger frequency of $\sim$90 Hz). Since February 2004 a lower multiplicity level M = 18 has been used, resulting in a trigger frequency of about 150 Hz, while the MuonDaq still uses the M = 24 trigger. The trigger signal is distributed to all TWRs and the single GPS latch simultaneously.
A description of the trigger system including all important time-delays can be seen in figure 4.6. The system is described in the text. The original trigger signal from the DMAD goes through a veto-logic to stabilise the system. The

DMAD trigger logic issues a trigger signal when approaching the multiplicity threshold. For a single event this can happen several times producing a burst of trigger signals. An artifical dead time of about 20 μs is used to prevent these multiple triggers. Trigger signals starting the TWRDaq in a short time distance lead to half filled buffers and thus result in corrupted data.
The external trigger pulse from the DMAD (event-trigger) goes to a discriminator (1) which serves as a pulse shaper. This signal is used as input for a level three coincidence logic (2). Only, if the DMAD trigger signal, the TRIGGER ENABLE from the TWRDaq and the VETO DISABLE shows a logic 1, does the trigger pass starting the TWR trigger.
The TWR trigger signal launches a gate generator (3), which forms the VETO DISABLE. The inverse output of the gate generator is connected to the logic coincidence and disables the output of the coincidence module for the chosen length of the gate signal. The delay between the TWR trigger signal and the start of the VETO DISABLE is 30 ns, determining the length of the TWR trigger signal.
The passing trigger is distributed by a logic fan out (4) to the different crates holding the TWRs and GPS latches. In order to reduce the input cabling of the crates and to make the system more reliable, the trigger is distributed via the P2 bus[7] on the VME backplane. The trigger is received by a converter board (5) in the crates changing the signal level to ECL[8] and transmitting it via the backplane.
The incoming trigger signal is delayed inside the TWR by a programmable number of clock cycles (internal clock of the TWR at 100 MHz) and serves as a COMMON STOP TRIGGER to the TWR, which switches to the next ring buffer and starts sampling for the next event. This external trigger signal is delivered simultaneously to all TWRs and to the GPS latch, which is synchronised by a connected GPS clock and stores the actual timestamp for each trigger in a FIFO.

4.2.3 The TWRDaq readout system

The TWRDaq is a network of VME crates including one *master crate* connected to several *remote crates*. The crates are connected by SIS3100 interfaces. A survey of the complete system of 2003 is shown in figure 4.7. The local SIS3100 modules in the remote crates contain the DSP and act as a bus master. The remote crate no. 3 also contains the GPS latch. The trigger is distributed to all TWRs and the single GPS latch simultaneously. Thus, a TWR event contains a GPS timestamp and a number of waveforms. As ad-

[7]Second free connector of the VME bus system.
[8]Emitter Coupled Logic

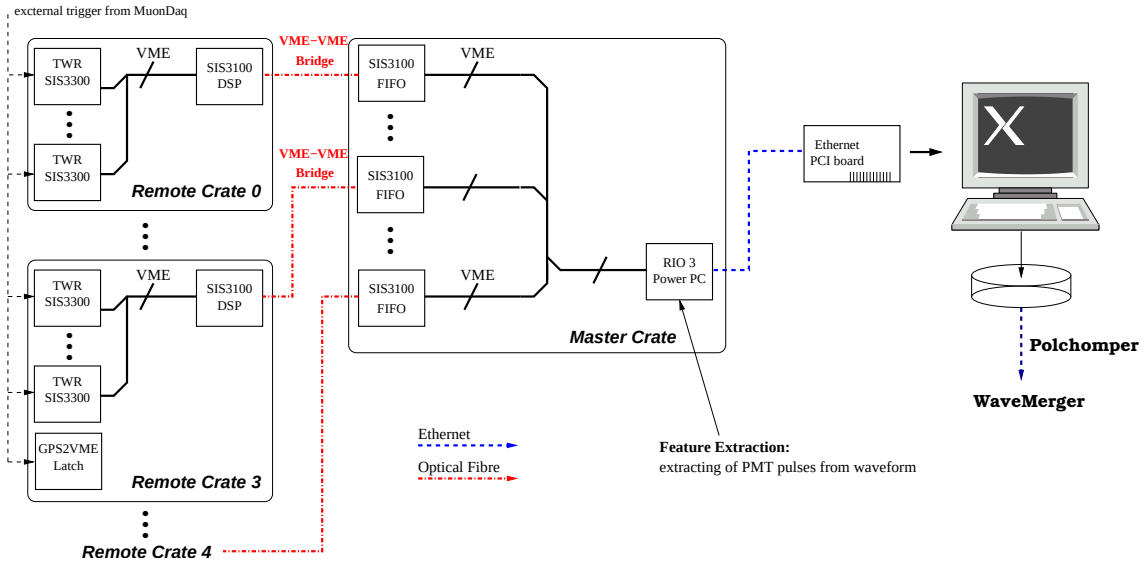

Figure 4.7: Survey of the TWRDaq system in 2003.

ditional timing information, the timestamps of the TWRs are stored. These timestamps are currently used for testing only.
After 128 event triggers, the buffer of the TWR is full and the data is read out by the DSP. The DSP program sorts the data according to events and sends it via two optical fibres to the other side of the SIS3100 interface, located in the *master crate*, which receives the data and stores it into a FIFO. In order to save time and disk space, the DSP only reads waveforms from those TWRs, that contain a pulse below the detection threshold. The information about which waveforms are "valid" is delivered by the TWR. This procedure is called *Zero suppression*.
In 2003, the TWRDaq readout was accomplished by two programs, the *reader* and the *eventbuilder*. The system was controlled by the reader running on a rio3 Power PC located in the master crate. The reader was a software package embedded in the *Multi Branch System MBS* [9] [B+00]. The data were read from the SIS3100 modules located in the master crate.
Finally, the data had to be collected from the rio3 and written into the final data format. The rio3 was connected to a PC running Linux via Ethernet, and the eventbuilder program, reading the data directly from a shared memory segment in the memory of the rio3, working as a client of the MBS system.
The current TWRDaq system has been running since February 2004. It is displayed in figure 4.8 and is a modified version of the DAQ running in 2003.

[9] DAQ software package developed by the *Gesellschaft für SchwerIonenforschung GSI* in Darmstadt, Germany.

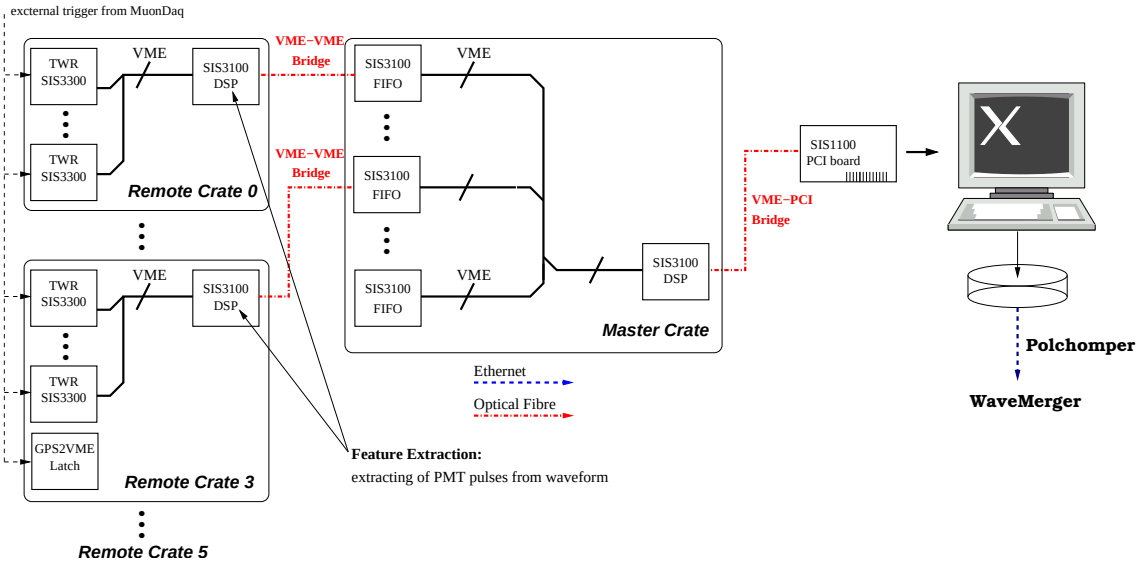

Figure 4.8: Overview of the TWRDaq system in 2004.

Limitations in performance of the rio3 Power PC and the MBS system led to the decision to upgrade the system. The changes made the system more reliable and made it possible to increase the trigger rate up to 200 Hz.
A major change is the replacement of the rio3 Power PC by an additional VME/PCI interface, consisting of a SIS1100 PCI card and a SIS3100 VME board.

The system in 2004 is now started and controlled fully by the eventbuilder software on the Linux PC. It is connected to the master crate by an additional bridge, consisting of a SIS3100 module in the master crate and a SIS1100 (PCI card) in the PC, linked by an optical fibre.

The state diagram of the TWRDaq is displayed in figure 4.9. When starting the TWRDaq, the TWR configuration file *TWR.cnf* is read and the baselines are measured as described in section 4.2.3. Afterwards the TWRs are initialised and the sampling starts by enabling the trigger signal. This state is referred to as initialisation. The TWRDaq is running and waits for the DSP to signal a full buffer of data.
After reading the data, the synchronisation is verified between TWR and GPS time. In case of synchronisation errors the system is restarted (all modules are reset and the system is started again), otherwise the system will wait for the next data buffer. This procedure is explained later in this section. If an unrecoverable hardware failure is detected, the system is aborted. In addition the system can be stopped by an external interrupt.
Table 4.3 summarises the main features and differences between the TWRdaq

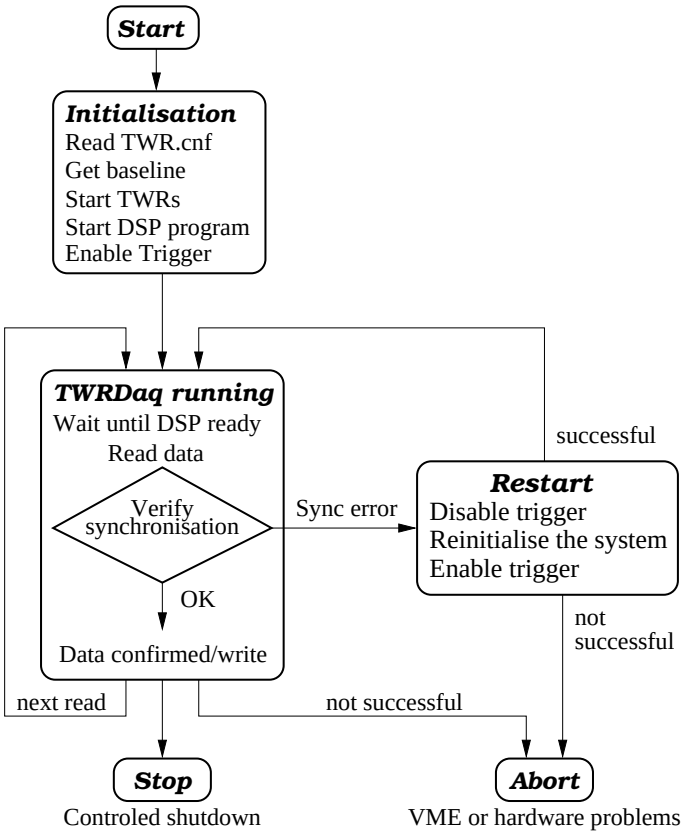

Figure 4.9: State diagram of the TWRDaq.

	TWRDaq in 2003	TWRDaq in 2004
number of remote crates	5	6
number of remote TWR s	72	75
number of connected channels	576	597
artificial dead time	20 μs	20 μs
DMAD multiplicity level	24	18
average trigger frequency	$\sim$ 90 Hz	$\sim$ 150 Hz
internal trigger delay	7μs	individual for each TWR
feature extraction done by	TWRDaq software on rio3	DSP program in remote SIS3100

Table 4.3: Main features and differences between TWRDaq in 2003 and 2004 season.

in the 2003 and 2004 seasons. The first TWRDaq in 2003 used a fixed internal trigger delay of about 7 μs, which led to a time window of about 3 μs before and 7 μs after the trigger time for the signals at the surface. Due to different

cable delays for the OMs, an individual trigger delay for each TWR has been used since 2004.
The further data flow is well described in the manual pages of the data-handler [Ack]. The raw TWR data is written to tape and it is also sent to other related processes. The final data format is displayed in figure A.2 in the appendix. The filename convention for the raw data files is described in section A.1.1 in the appendix.

The feature extraction

After zero suppression, a further data compression is necessary and is explained in this paragraph. While the hit information of the MuonDaq only consists of a few numbers, the data volume of a waveform is substantially larger. In the present configuration, a full uncompressed waveform of one channel consists of 2048 bytes. Since the pulses are rather short, the waveform mostly contains baseline noise.
In order to reduce the data amount significantly, an online data compression algorithm is applied to the data, which is referred to as *Feature Extraction FE* throughout this document. The basic idea is to extract the signal pulses from the waveform including a number of preceeding and succeeding values. In 2003 the compression was implemented in the software running on the rio3, while in 2004 it was implemented in the DSP program. Since the PMT pulses of an electrical channel have a width of about 300 ns and the pulses of an optical channel only about 30 ns, this is an effective way to reduce the data amount at an early stage.
The complete *feature extraction* algorithm is shown in figure 4.21. Figure 4.10

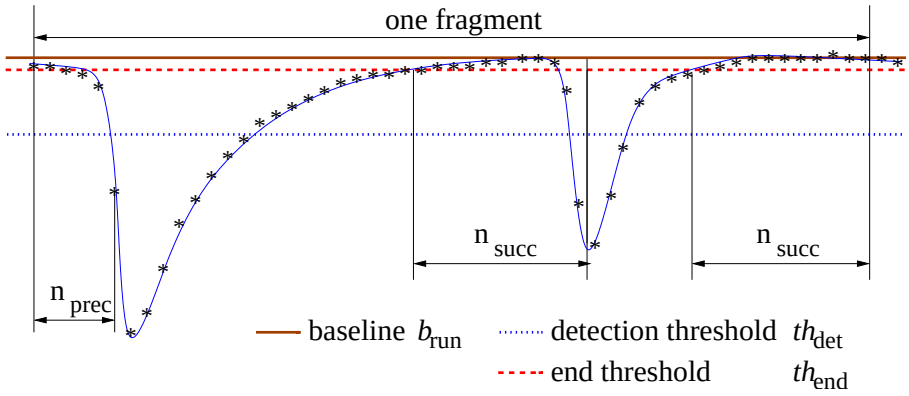

Figure 4.10: Different thresholds are applied to the signal during the extraction of pulses.

visualises the different thresholds applied to the signal. The algorithm searches for a value below the *detection threshold* th_{det}. If a value below this threshold is found, a *waveform fragment* is created. First, a programmable number of preceeding n_{prec} values are added and all following values are added to the fragment until the end of the pulse is detected. Since the slope of the leading edge of the PMT pulse has a smaller slope and may overshoot the baseline b_{run}, an absolute threshold th_{end} is defined for the end of the pulse. It is close to the baseline and is calculated as

$$th_{\mathrm{end}} = b_{\mathrm{run}} - 4\,\mathrm{digits}\,.$$

In order to obtain the full pulse including the tail of the pulse, the end of the pulse is detected by applying th_{end}. Finally, n_{succ} samples are added to the fragment after the end of a pulse. The thresholds are set in digits, where 1 digit corresponds to 1.22 mV.
If an adjacent pulse is detected within the n_{succ} samples, i.e. a sample surpasses th_{det} again, the waveform fragment is continued with this pulse. Otherwise the fragment is closed. Any further pulse is recorded in an additional fragment. The waveform can consist of more than one fragment, which itself can contain more than one PMT pulse.
The algorithm was not changed between the seasons 2003 and 2004, except that in 2003 the complete waveform was written out, if the number of waveform fragments per waveform was larger than 4. The extracted pulses are stored in a binary data format described in figure A.3 in the appendix.
The parameters used for the *feature extraction* in 2003 and 2004 are listed in

channel type	Parameter	season 2003	season 2004
electrical	number of preceeding samples	20	12
	number of following samples	4	8
optical	number of preceeding samples	20	3
	number of following samples	4	4

Table 4.4: Parameters for the Feature Extraction used in 2003 and 2004.

table 4.4. The algorithm depends on the applied thresholds, which have to be optimised to detect single photon pulses.

Determining the detection threshold th_{det}

The *detection threshold* th_{det} has to be determined for every individual channel in the TWR. In order to make the system independent of baseline changes, th_{det} is calculated from a *measured baseline* b_{run} and a *fixed threshold* th_{amp} as

$$th_{\mathrm{det}} = b_{\mathrm{run}} - th_{\mathrm{amp}},\,.$$

The threshold th_{amp} is a fraction of the single photo-electron pulse and is

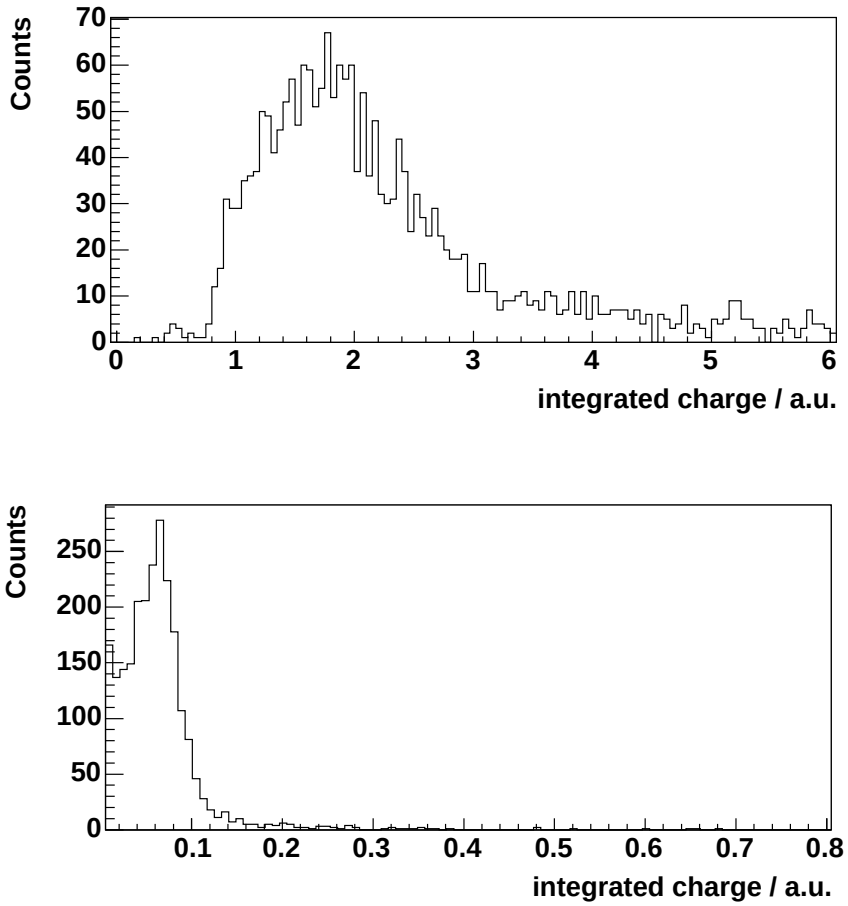

Figure 4.11: Distribution of integrated charges of an electrical (OM 1 – top) and an optical channel (OM 625 – bottom).

obtained from the charge distribution histogram, see figure 4.11. The charge of a pulse is defined as the area between baseline and the actual pulse. The threshold is optimised in such a way that the single photon pulse is visible while the PMT noise is minimised. Typical distributions of integrated charges are displayed in figure 4.11, for an optical and an electrical channel.
The values of th_{det} have a fixed value for a whole season. They are listed in the TWR.cnf file, which is explained in detail in the appendix. The value of b_{run} is determined once per run, during initialisation, by calculating the average value of 128 waveforms. Since most of the waveforms are empty and the pulses are small compared to the total waveform window, this procedure delivers a good estimate for the baseline. Thus, b_{run} has a fixed value for each run[10], which is contained in the header of each raw data file.

[10]The length of a run is 24 hours.

Since the baseline can vary with time, an actual estimate for the baseline is

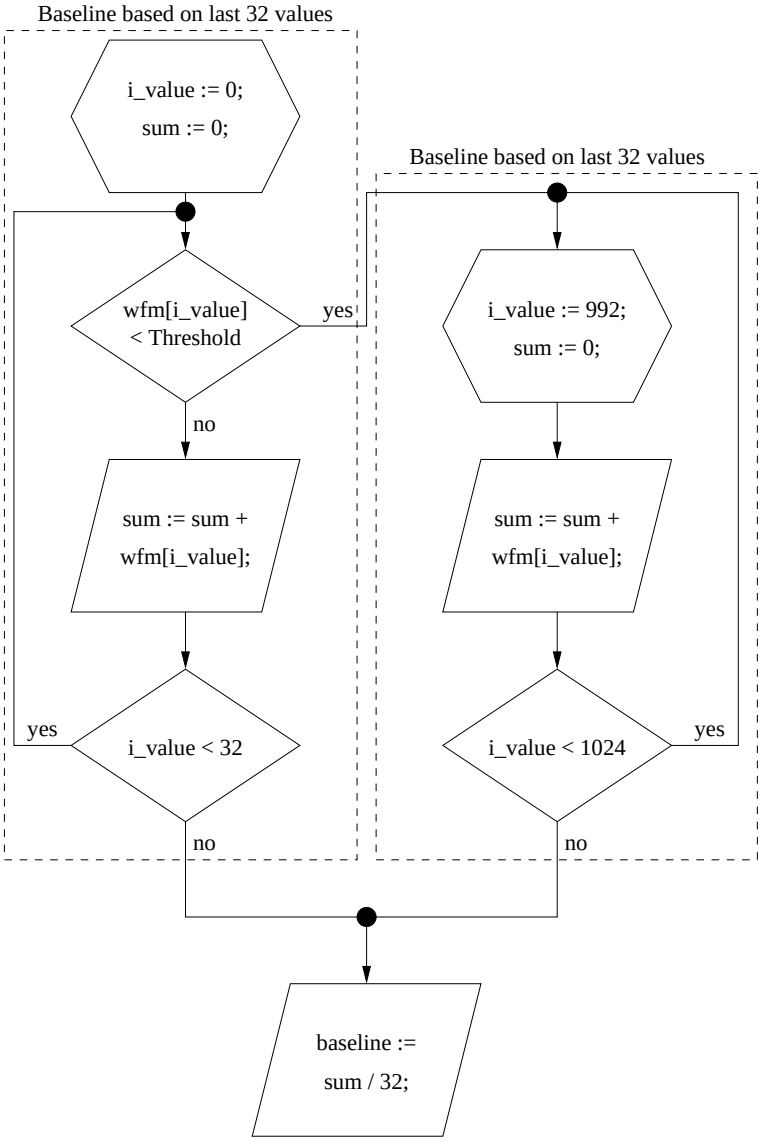

Figure 4.12: Procedure for estimating the baseline. The full waveform containing 1024 samples is stored in the `wfm` field. If no pulse is detected below the threshold within the first 32 samples of the waveform, the baseline is calculated as average of the first 32 samples. Otherwise the average of the last 32 samples is considered as baseline estimate.

necessary for data analysis. The value of b_{run} does not give any information about short term baseline shifts and the noise behaviour of the individual channel. Thus, for every single waveform an estimated baseline is determined, which is called *dynamic baseline* b_{dyn} throughout this document. In the 2003 season the value of b_{dyn} was determined by calculating the average value of the first samples prior to the first pulse in a waveform. If a pulse appears

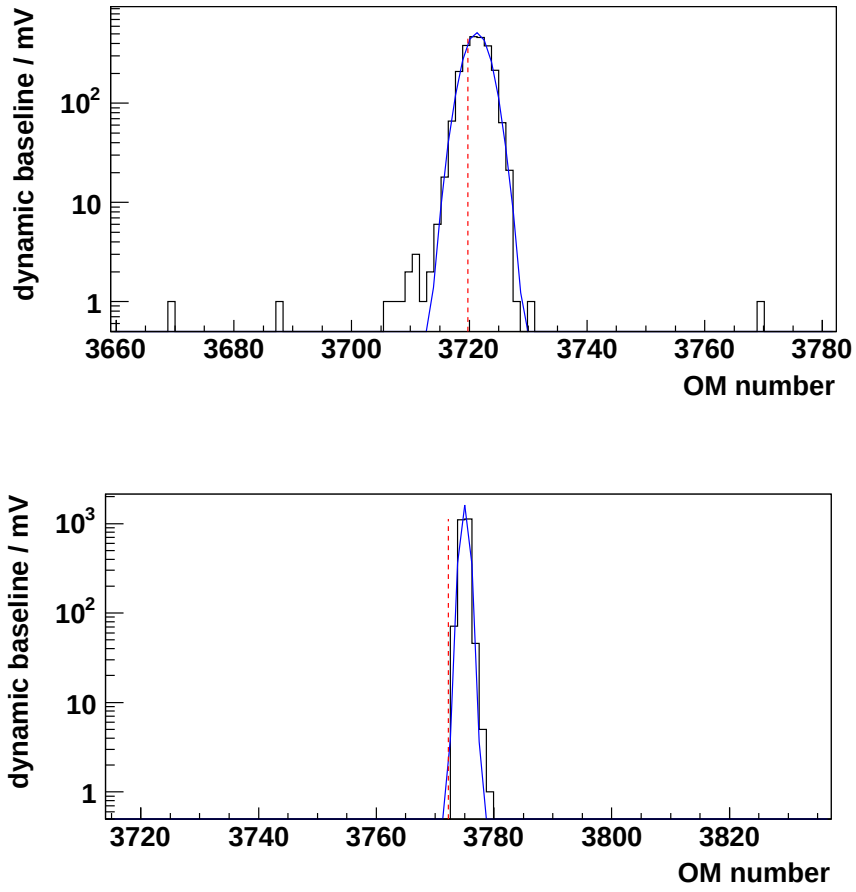

Figure 4.13: Distribution of b_{dyn} of an electrical (top) and an optical channel (bottom). The dashed line shows the b_{run}.

within the first 20 values of the waveform, the part of the waveform after the last detected pulse was used. The calculation was done on the rio3 Power PC.
In the 2004 season the procedure was changed slightly in order to implement the algorithm in the DSP. The procedure of estimating the baseline is sketched in figure 4.12. At first, the DSP starts to loop over the first 32 values of the waveform. If no value below the threshold is detected, the average value of these 32 values is considered as an estimate for the baseline. If at least one value below the threshold is detected, the baseline is determined by the last 32 values of the waveform. The probability to detect a pulse within the first 32 samples and within the last 32 samples of the waveform is small.
Figure 4.13 shows typical distributions of b_{dyn}, for an electrical and an optical channel. The deviation of the average value of b_{dyn} from the b_{run} is displayed in figure 4.14 for each channel. A systematic shift appears, which is caused by the procedure determining the b_{run}. As explained before, b_{run} is determined

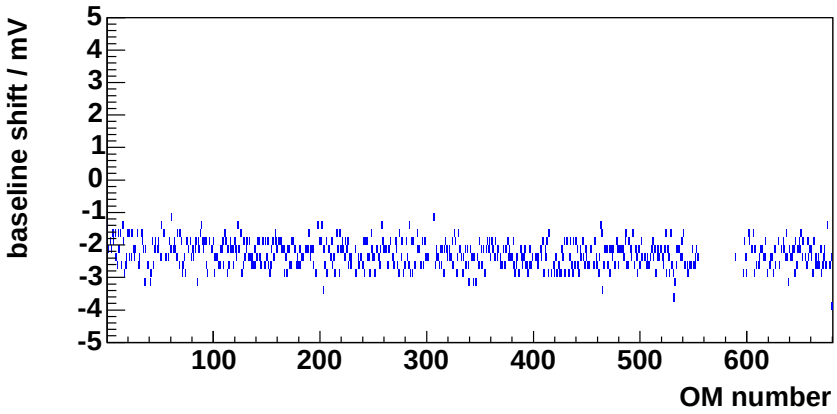

Figure 4.14: Difference between b_{run} and b_{dyn} versus channel number.

by integrating over 128 waveforms with a possible background of pulses in the waveforms. Pulses that appear in the waveforms shift b_{run} to a lower value than the true baseline. Since this shift is small and stable, it is included in the detection threshold.
Since the memory space for a program in the DSP is limited, the algorithm has to be simple. The current algorithm, as displayed in figure 4.21, may produce overlapping fragments. In order to reduce the amount of data and to simplify the further analysis, such overlapping fragments are merged to one compact fragment by the eventbuilder.

The efficiency of the compression mainly depends on the pulse widths and the resulting fragment lengths. Figure 4.15 shows the distribution of the fraction of remaining data as a percent of the initial data volume for an electrical and an optical channel. As the electrical channels produce wider pulses, the waveform fragments are longer and the compression efficiency is lower for these channels. The average fraction of remaining data is displayed in figure 4.16 for all channels. It can be seen that the compression efficiency differs for different types of analogue transmission. While the first four strings (OM 1 – OM 80), which use coaxial cables produce longer pulses and result in a compression of about 8 % of the initial data, the waveforms from strings 5 to 10, using twisted pair cables for analogue transmission, have shorter pulses resulting in a lower amount of data after reduction of about 5 %. The waveforms of the channels using optical transmission (most of the OMs above OM 302) are compressed to about 3 %. Some channels above OM 302 have broken optical fibres and are read out by twisted pair cables. These OMs can be identified in figure 4.16 by the larger amount of remaining data.

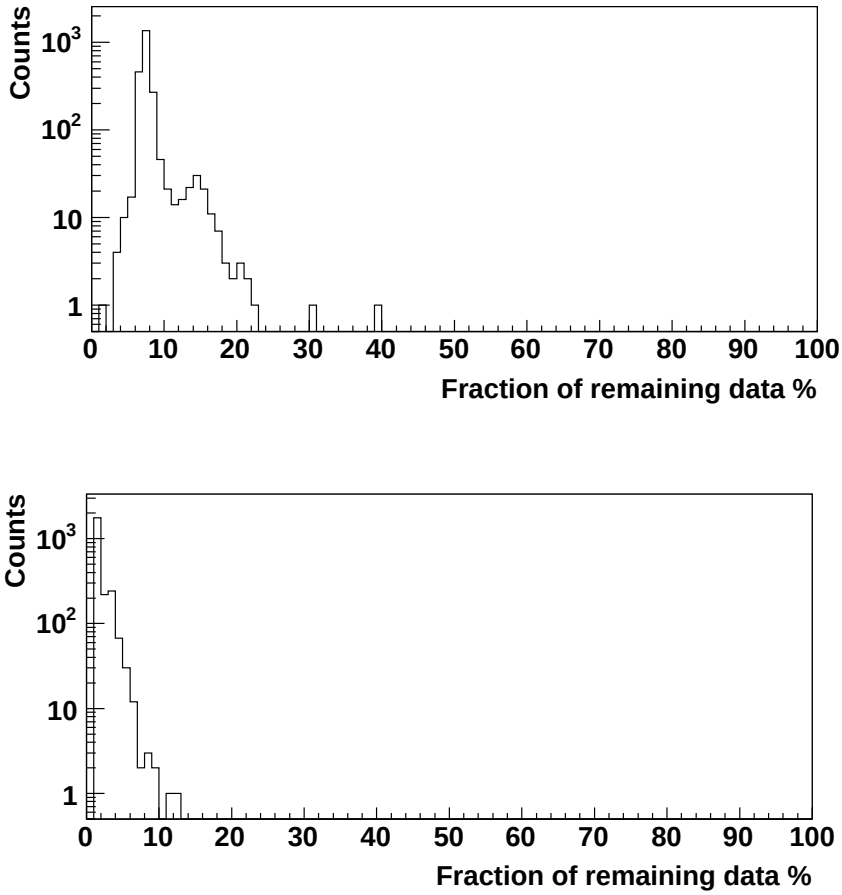

Figure 4.15: Remaining data amount in percent of the initial data illustrating the compression efficiency of an electrical (top) and an optical channel (bottom).

4.2.4 Verification of the synchronisation

The data are read out by the DAQ in bunches of 128 triggered events. The trigger signal arrives synchronously at the TWR modules and the GPS latch. However, there is a small chance of a lost or an additional trigger, e.g. due to electronics noise. A synchronisation error which is not noticed will lead to a misalignment in the data. With an additional trigger in one TWR after the Nth event, all following waveforms from this specific TWR will be associated with a wrong event leading to corrupted data for all following events. Thus, a misalignment must be avoided. However, the TWRs are equipped with an intrinsic measure of time which can be used for relative time measurements, the timestamp counter register. A synchronisation error

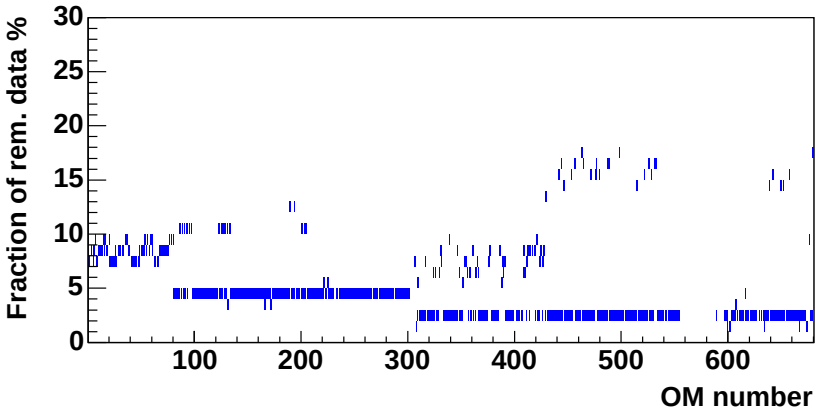

Figure 4.16: Average remaining data amount of all channels.

is detected by inspecting the time difference between event 127 and event 128 using the timestamp counter of each TWR and the GPS timestamps. First, the timestamp differences of all TWRs are compared to a reference timestamp difference calculated from TWR 1 in the first crate. Then, the reference timestamp difference is compared to the time difference of the GPS timestamps.
In case of synchronisation errors, the system is stopped, the trigger is disabled and the system will be reinitialised and restarted. The data is not written out.

4.2.5 Filtering and Merging

In order to verify the data quality, events belonging to the same trigger signal sampled by both MuonDaq and TWRDaq, are merged to one event. The events are identified by the GPS time. This is performed by the *wavemerger* program using the GPS times of both DAQ. A comprehensive survey of the wavemerger and the further datahandling can be found in [A$^+$04b].

The further data handling is shown in figure 4.17. The data from the eventbuilder is written to disk and is collected by the *Polechomper* program. This is a program running at the South Pole network, which is responsible for data transfer and storage. All raw data from MuonDaq and TWRDaq is stored on tape. The tapes are sent to the Northern hemisphere in the following Antarctic summer. The whole year, a stream of data is sent continuously via satellite to the outside world. Due to the limited bandwidth for the data transmission from the Pole to the outside world, it is essential to filter

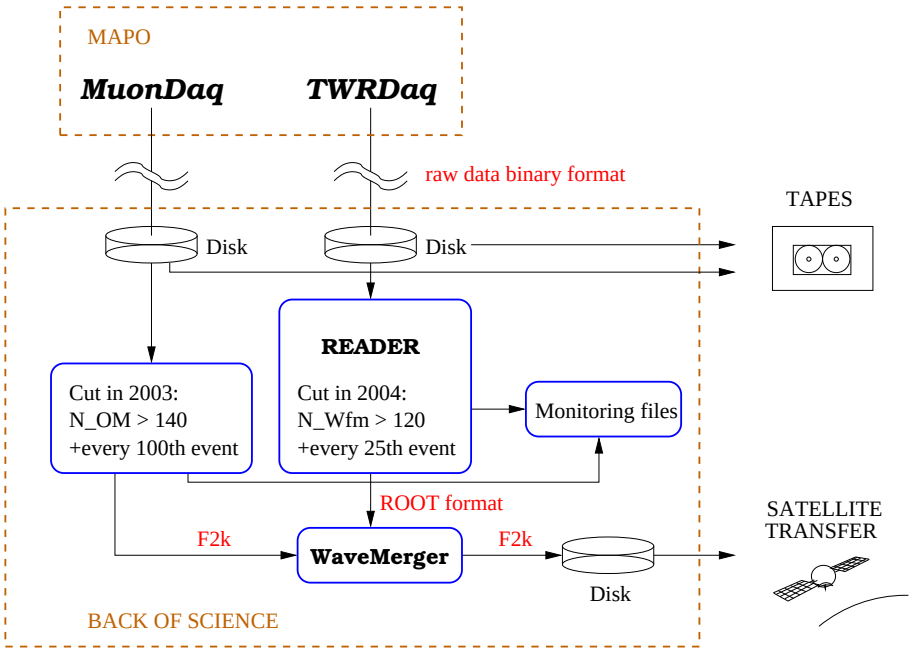

Figure 4.17: Survey of the online data-flow at the Pole.

the data and to transmit only the most interesting events, i.e. high energy events. The *wavereader* reads the raw data from TWRDaq and sends it to the *wavemerger*.
In 2003 all data from the TWRDaq was sent to the wavemerger, while only events with more than 140 hit OMs in the MuonDaq were sent to the wavemerger.
However, due to the higher data rate, this was not practicle in 2004. In 2004, all data from the MuonDaq was sent to the wavemerger, while only events with more than 120 hit OMs in the TWRDaq were sent to the wavemerger. Events passing this cut are sent to the merging process, which searches the data from the MuonDaq for events matching the TWR events.
In addition to these high energy events, a down-scaled stream of normal events are also merged. Currently every 25th event is selected, which helps to understand these low energy events in the Northern hemisphere. However, many of these low energy events are not written to the standard AMANDA format (f2000), because there are no matching events from the MuonDaq. The data produced by the merging process is send to the satellite link and is transmitted to the Northern hemisphere.
In order to monitor the system, the reader produces histograms which are written into a root format and later merged with other root monitoring files from the MuonDaq to produce a monitoring file for each run. These files are sent via satellite to the AMANDA monitoring system [Ahr01].

4.3 System stability tests

In the Antarctic season 2003/2004 the multiplicity threshold M for the TWRDaq was lowered from $M = 24$ to $M = 18$. Furthermore, some test runs were made with a trigger multiplicity of $M = 16$. Figure 4.18 shows the distribution of trigger rates for different multiplicities. For $M = 16$ the trigger rate can rise up to 220 Hz without causing instabilities in the readout process.

The dead time of a data taking system can be determined by analysing the

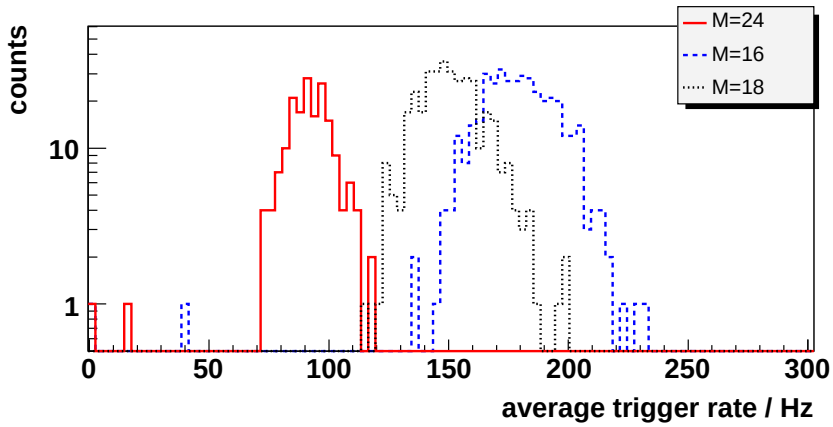

Figure 4.18: Trigger rates using different levels of multiplicity from the trigger of the MuonDaq. The trigger rate is determined in a time window of one second. The measured trigger frequencies below 70 Hz occur just before or after the VLF veto window (for details see section 4.2.1).

time differences between adjacent events [Leo94], which is shown in figure 4.19 (top). As already explained in section 4.2.2, an artificial dead time of about 20 μs was chosen to avoid overlapping waveforms. In figure 4.19 (lower), a magnification of the first bin of the upper histogram is shown. A sharp cutoff is visible, which is caused by the artificial dead time. Assuming that this dead time is exactly 20 μs, the real dead time in percent of the total number of triggers can be estimated to be 0.015 ± 0.01 % for $M = 24$ and 0.018 ± 0.013 % for $M = 18$. Thus, the TWRDaq in the present configuration operates almost without dead time.

The increase in events of smaller size, i.e. fewer waveforms, for low trigger multiplicities can be seen in figure 4.20. It can be seen that, for a lower trigger

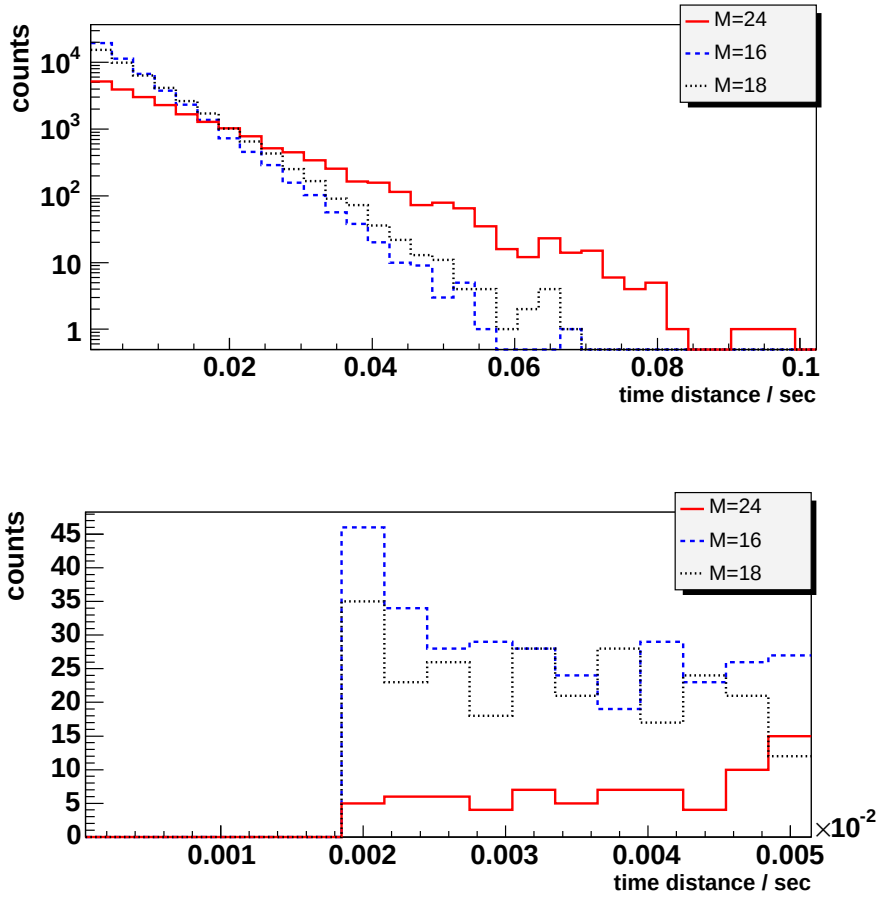

Figure 4.19: Time difference between adjacent events for various multiplicity triggers (top). A magnification of the first bin is displayed below. The artificial dead time of about 20 μs can be seen as a cutoff in the figure below.

multiplicity these events with a small number of hit OMs dominate. Furthermore, it was shown that using a multiplicy trigger with $M = 16$, the events are still not dominated by noise events [Mes03]. Thus, they contain meaningful data.

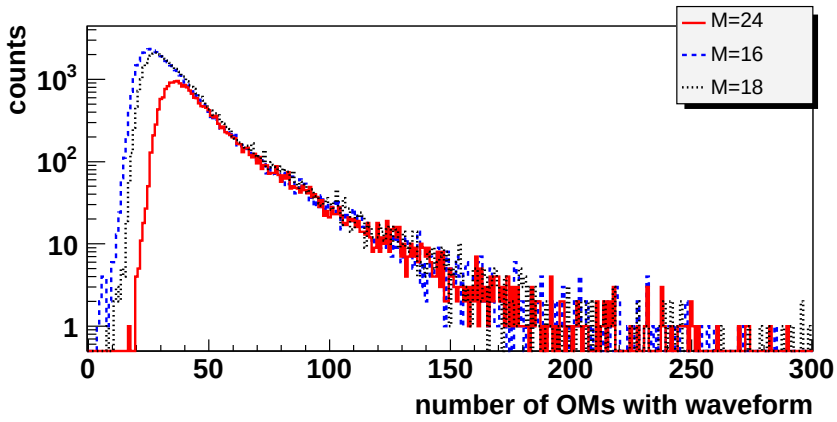

Figure 4.20: The distribution of number of hit OMs per event in the TWRDaq.

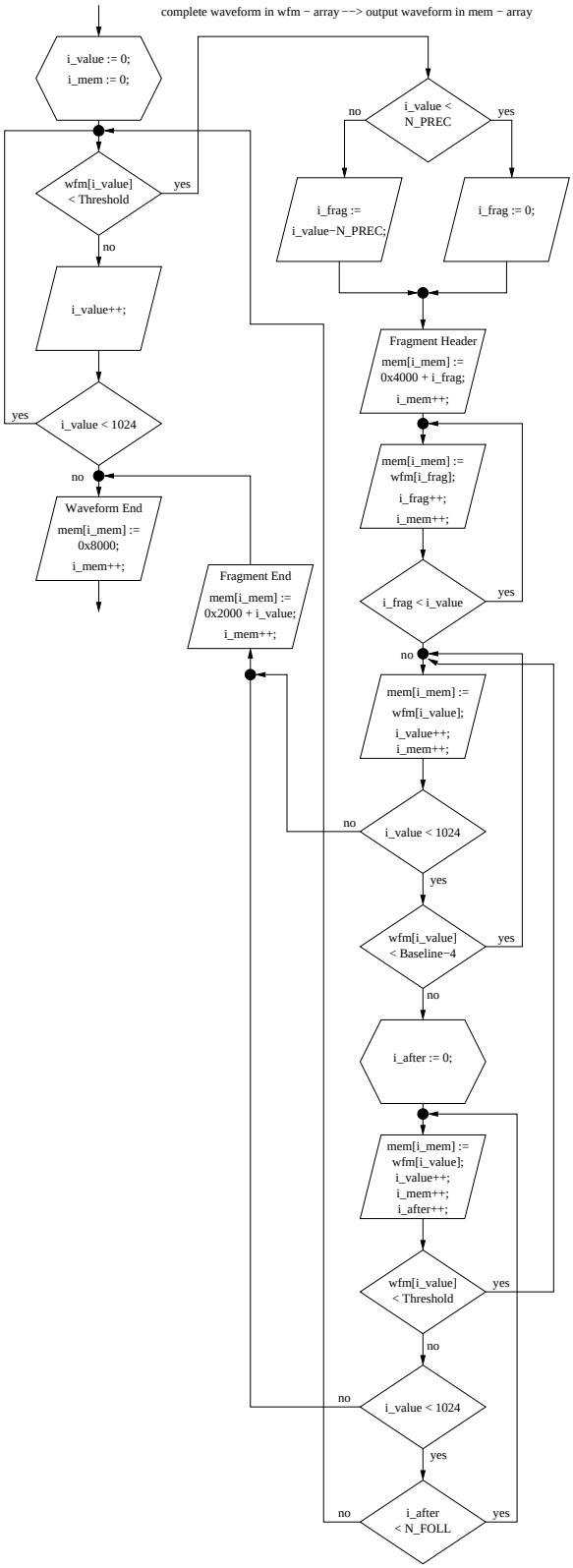

Figure 4.21: The complete Feature Extraction Algorithm.

5

Reconstruction with Waveforms

This section surveys on the reconstruction results as obtained with data from TWRDaq. First, the hit extraction algorithm, which analyses the waveform fragments and extracts hits, is described in section 5.1.1.
The quality of the analysis relies on the resolution of the measured pulse start time. The time calibration of the TWRDaq is described in detail in section 5.1.2.
In order to verify the correctness of the data from the TWRDaq, it is compared with the data from the MuonDaq in section 5.2.
Finally, a first approach to the use of TWR data for track reconstruction is described in section 5.2.3. The goal is to demonstrate that a track reconstruction with data from the TWRDaq gives identical results to the MuonDaq. The reconstruction uses the existing AMANDA software.

5.1 Data processing and analysis

5.1.1 Hit extraction

For the reconstruction of particle tracks and their energy in Čerenkov detectors, the arrival time of the pulses and the number of photons in each pulse has to be extracted from each OM. Thus, a hit in an OM consists of a timestamp and a number of photoelectrons extracted from a PMT pulse.
First, the pulses in the waveform have to be identified by an algorithm. A waveform pulse may be the superposition of a number of single photoelectron pulses, which arrive at different times. Therefore, the resulting shape of the waveform can be rather complex. In order to obtain the maximum information, a good pulse separation is desirable for reconstruction, i.e. to extract arrival times of pulses, even if they have only a small time separation.

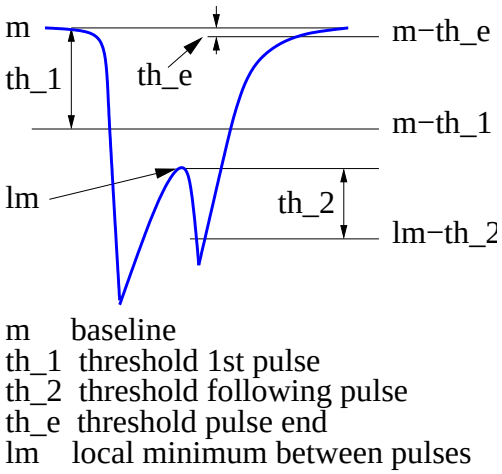

Figure 5.1: Relative thresholds used for hit extraction.

While the narrow pulses of the optical channels result in good resolution for pulse separation, the electrical channels show a different behaviour. Due to dispersion in the electrical cables, the received signals at the surface are wider and the resolution for the pulse separation is worse.

The hit extraction uses different thresholds, which are illustrated in figure 5.1. Similar to the *feature extraction* algorithm, the first pulse is found with a fixed threshold, *th_1*, relative to the baseline *m*. Typical values for the threshold are 180 mV for the electrical channels and 18 mV for optical channels. Thus, the applied absolute threshold is *m* - *th_1* for a first pulse.
In order to identify an adjacent pulse in the falling edge of the previous pulse, the algorithm searches for a local minimum, *lm*, by applying a different threshold, *th_2*, relative to any local minimum. Since *th_1* takes into account the amplitude of a single photo-electron pulse from each individual channel, *th_2* was chosen as a fraction of *th_1*. The pulse end is detected if the signal exceeds another threshold level, *the_e*. After detecting the end of a pulse, the algorithm searches for a next pulse, again using *th_1* as the threshold level. For the analysis in this thesis, the optimised thresholds (see section 4.2.3) for the *feature extraction* are used for detection of the first pulses. For the pulse end, a reduced relative threshold of th_e = th_1 / 10 is used.

The pulse separation benefits from the extra information contained in the waveforms as compared to the MuonDaq. For overlapping pulses, the local minimum between the pulses serves as the baseline and the *linear fit method* (see below) can be applied to all pulses. The advantage of the pulse separation using the dynamic threshold is demonstrated in figure 5.2. While the TDC detects only two pulses (lower dashed lines), the waveform analysis can resolve four pulses (middle dash-doted lines).

The number of photo-electrons in each pulse is obtained by integrating the

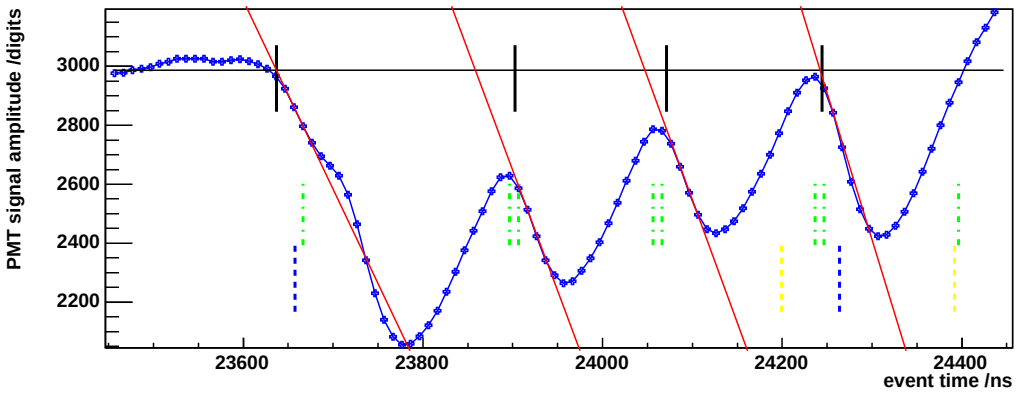

Figure 5.2: A waveform measured with OM 180. The lower (dashed) vertical lines show the leading and trailing edge as measured by the TDC, while the middle (dash dotted) lines indicate the pulses found by the hit extraction. The pulse separation benefits from the increased information contained in the waveforms. The solid lines show the result of the linear fit method.

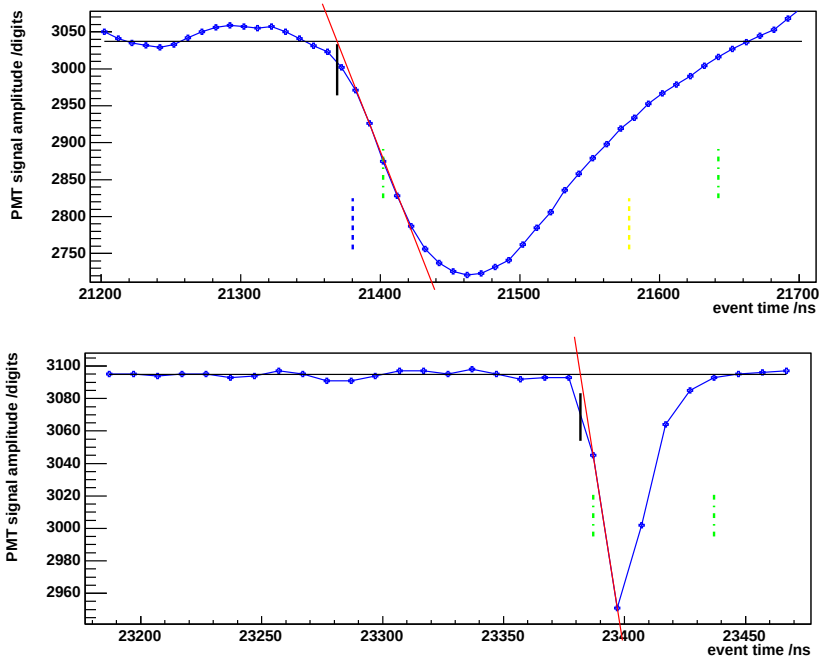

Figure 5.3: Linear fit to determine the pulse onset time. An electrical pulse of OM 115 (top) and an optical pulse of OM 521 (bottom).

area of the waveform between the baseline and the pulse itself and dividing

it by the mean charge for a *single photo electron 1 p.e.* pulse. The charge of each pulse is proportional to the area between the baseline and the pulse itself. In order to get a meaningful unit for the charge, the area is transformed into nC. The analogue signals are transmitted from the ORBs and SWAMPs to the TWRs via coaxial cables, which are terminated by a 50 Ω resistor. The charge C in nC is calculated as

$$C = \frac{10\text{ns}}{50\Omega} \cdot \frac{5V}{4096} \cdot \sum_{i=0}^{n} (a_\text{i} - b_\text{dyn}) \,,$$

where a_i are the sampled values of the TWR, n is the number of sampled values in the pulse and b_dyn is the *dynamic baseline*. The pulse onset time as determined with a fixed threshold is not sufficient for the analysis. Sampling the complete shape of the PMT pulses provides the opportunity to improve the time resolution itself.

Linear fit method

The determination of the pulse onset time is performed using a linear fit to the leading edge. The algorithm searches for the maximum rise between two values, x_i and $x_{\text{i}+1}$, within the leading edge. In the case of an **electrical channel**, the first sample before the maximum rise, $x_{\text{i}-1}$, and the first sample after the maximum rise, $x_{\text{i}+2}$, are used to determine the tangent. For the **optical channels**, the tangent is calculated with just the two values x_i and $x_{\text{i}+1}$ of maximum rise. The difference in the procedures, for the optical and electrical channels is due to the maximum number of values within the leading edge. In the case of an optical channel, the pulse width is shorter and therefore, the maximum number of values is smaller than in the electrical case.
The crossing point of the tangent from the linear fit and the baseline is considered as a good estimate of the pulse onset and is shown in figure 5.3 for an optical and an electrical channel. This procedure would lead to incorrect results for an adjacent pulse located on the falling edge of the predecessor pulse. The pulse onset time of these is determined by the crossing point of the linear fit and the local miminum, *lm*. Due to dispersion in the cables, the electrical channels have a slower leading edge rise-time. Therefore, the time difference between the beginning of the pulse found with the fixed threshold and the pulse onset as determined with the *linear fit method*, is larger for electrical channels. In contrast, the difference is very small for the optical channels, since pulses from these channels have a small width and a steep leading edge. In most cases, the leading edge of these pulses contains only 2 or 3 samples. The α-calibration used by the MuonDaq (see section 3.3.1), can be replaced by the *linear fit method*.

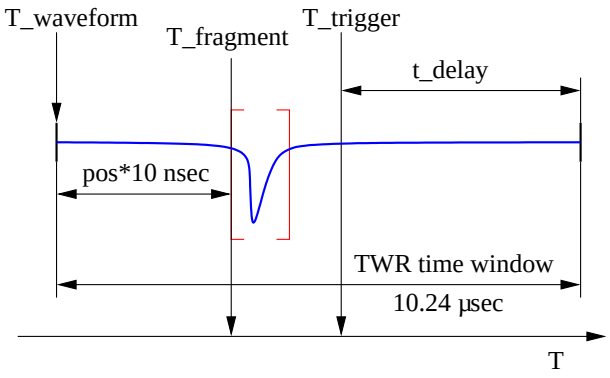

Figure 5.4: Time correction for the waveforms.

An important piece of information contained in the TWR raw data is an estimate for the current baseline, called the dynamic baseline b_{dyn}, as introduced in section 4.2.3. This baseline estimate, b_{dyn}, may be used in the hit extraction analysis to give a value for the baseline, m. The merged data of 2004 include b_{dyn}, while the merged data of 2003 do not. However, in 2003 about 20 samples before the first pulse were included in every fragment. The average of the first five values in the fragment forms a reliable estimate for b_{dyn}.

5.1.2 Time synchronisation and calibration

The global time information for an event which is included in the TWR raw data is the GPS timestamp of the trigger time T_{trigger}. The start time of every waveform fragment has to be determined. Figure 5.4 illustrates the correction procedure. As described in section 4.2.1, the incoming trigger signal is delayed by a time interval, t_{delay}, in order to sample a time interval around the trigger time. The parameter, *pos*, is stored in the TWR raw data and gives the position of the waveform fragment relative to the total waveform window. *pos* is counted in sample points. Thus, the start time of every waveform fragment has to be corrected using the folowing formula

$$T_{\mathrm{fragment}} = T_{\mathrm{trigger}} - (10.24\mu\mathrm{s} - t_{\mathrm{delay}}) + (\mathrm{pos} \times 10\mathrm{ns})\,. \tag{5.1}$$

As already mentioned in section 3.3.1, the transmitted analogue signals experience a delay, t_0, due to different cable delays in the ice. In addition, various delays are caused by the electronics. For reconstruction, these delays have to be determined in order to obtain the exact arrival times of the photons at the location of the OM.

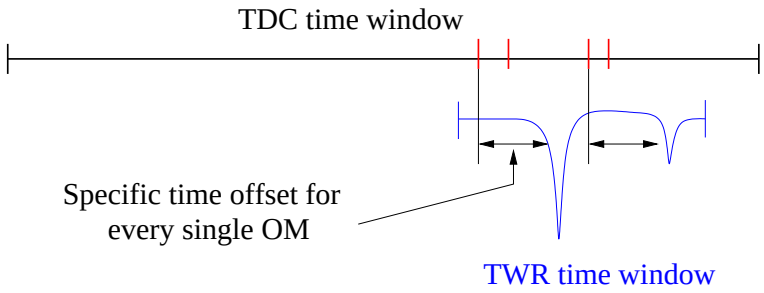

Figure 5.5: A first approach to calibrate the timing of the system using the t_0 calibration of the MuonDaq.

The t_0-calibration has been done for the data from the MuonDaq using a calibration laser signal [A+00]. For the analysis of the MuonDaq data, the pulse onset time is represented by the leading edge as measured by the TDC. Since the TDC time is determined using a discriminator with a fixed threshold, the arrival time has to be corrected by the α-calibration, depending on the pulse amplitude (pADC value). This correction is defined by

$$t_{\text{corrected}} = t_{\text{raw}} - t_0 - \frac{\alpha}{\sqrt{\text{pADC}}}\,. \tag{5.2}$$

However, the association between the pulse and the pADC value is ambiguous for more than one pulse per waveform leading to incorrect time corrections for multiple pulses.

A first approach to the calibration of the TWRDaq is to calibrate the time offsets with respect to the MuonDaq and to use the calibration constants for the MuonDaq.

In order to find these offsets, δt_0, the merged data stream is used since it combines data from MuonDaq and TWRDaq. The main idea is to calculate the time difference between the first appearing pulse in the waveform and the leading edge of the first pulse in the TDC data for single OM, which is connected to both TWRDaq and MuonDaq, .
Although both DAQs use different thresholds for detecting pulses and since the TDC time window (about 34 μs) is much longer than the time window of the TWR (10.24 μs), it is assumed that most of the pulses are assigned to the same physical pulse. The occurence of a peak justifies that assumption.
In order to enhance the time accuracy, the α-calibration is applied to the data from the MuonDaq. The exact pulse start time of the waveform pulses is determined using the linear fit method as described above.

The distribution of δt_0 for an electrical and an optical pulse are shown in figure 5.6. The value of δt_0 can be determined by a Gaussian fit, which is also displayed in the diagram.

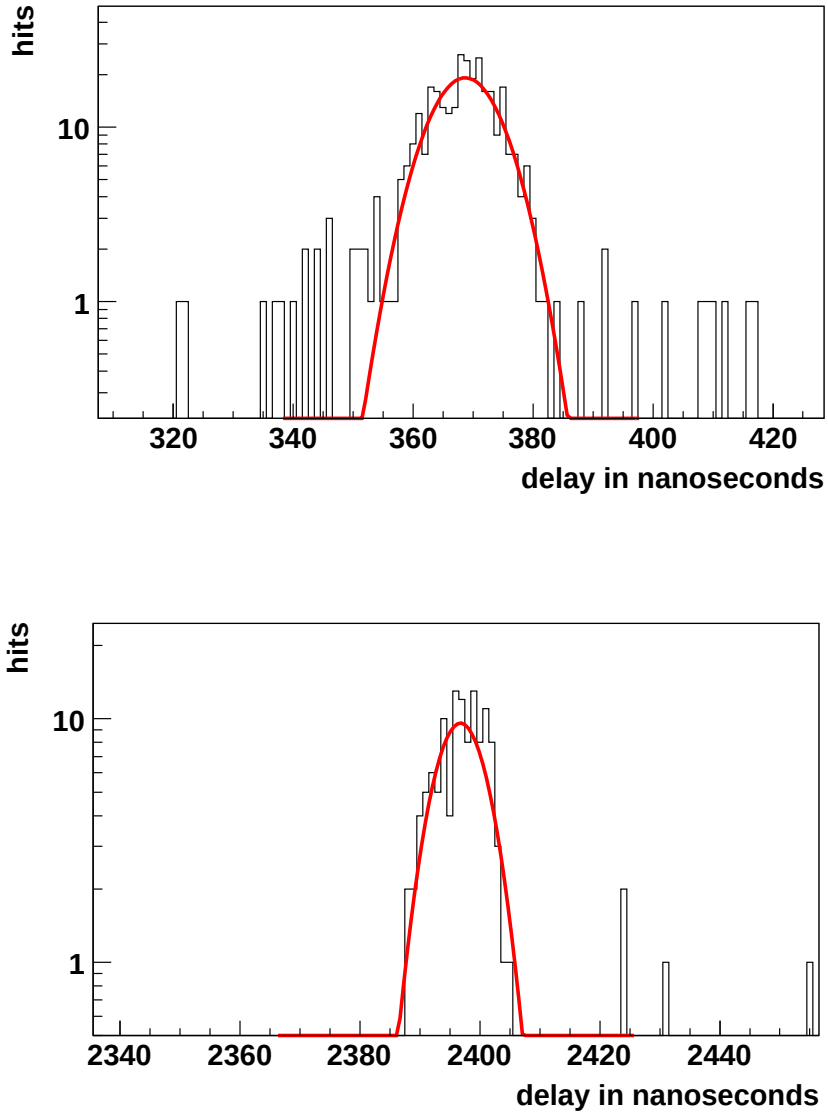

Figure 5.6: The time difference between the first pulse in a waveform and the first leading edge in the TDC window. Above an electrical channel (OM 5), below an optical channel (OM 423) are shown.

The distribution of δt_0 for the whole detector for the year 2003 is shown in figure 5.7.

The accuracy of this calibration can be estimated using the width of the δt_0 distribution, which is displayed in figure 5.8. While the optical pulses show a typical width between 3.5 ns and 4.5 ns, the distributions of the electrical

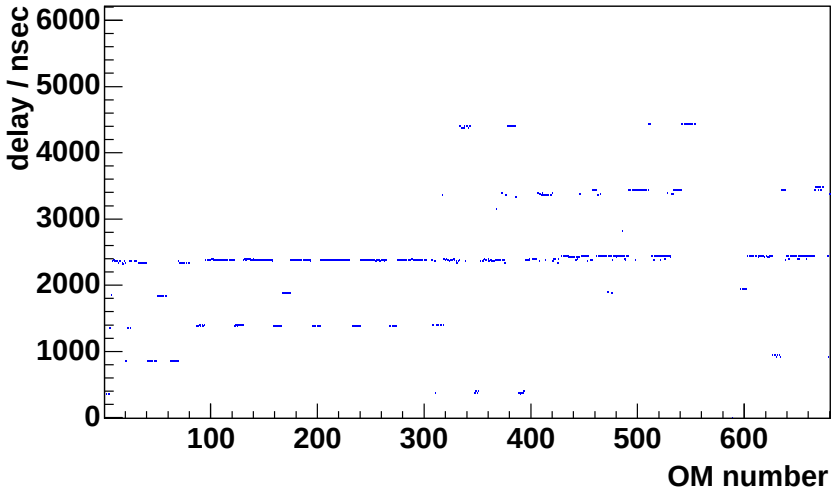

Figure 5.7: The distribution of the δt_0 versus OM number (results from 2003 data).

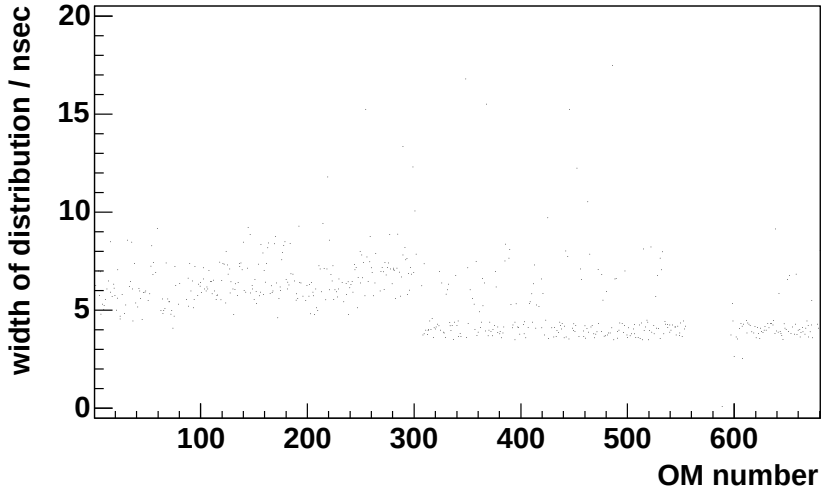

Figure 5.8: The distribution of the σ of the time calibration fit versus OM number (results from 2003 data).

channels are wider, between 5 ns and 8 ns. As described in section 5.3.1, the error of the TWR synchronisation dominates the optical channels, while

the width of the electrical channels can be related to a lower accuracy of the applied α-calibration or the *linear fit method*.
However, it was found that the calibration can be improved by using only very large pulses having sharper leading edges, especially for strings 1 to 4.

5.1.3 Photon counting

Charge calibration

For N single photons arriving within a small time window, T, the signals will superimpose to one pulse in the PMT and cannot be separated. If the photons arrive almost synchronously, the amplitude will reach a value of N times the amplitude of a single photon pulse. However, as the arrival times differ more, the superposition results in a flatter and wider pulse. Thus, the amplitude is not a good measure of the number of photons.
For larger time delays between the arriving photons, the pulses can be separated. While the pulses of OMs with optical transmission are measured with a width of a few 10 ns, the pulses of OMs with electrical transmission are much wider. In this case, the separation is less efficient.
While the MuonDaq uses the pulse amplitude for determining the number of photons contained in the pulse, the reconstruction of waveforms may utilise the integrated charge of the pulse, excluding the overshoot. A clear advantage is the fact that, for overlapping single photon pulses arriving with a time delay, t_d, and an average pulse width, t_{width}, with $t_d < t_{\text{width}}$, the integrated charge rather than the amplitude, gives a more reliable measure for photon counting. Figure 5.9 shows a typical distribution of the integrated charge of one OM.
The size of the single photo electron pulse is determined by a gaussian fit, which is displayed in figure 5.9. The distribution of the single photo electron pulse can be seen in figure 5.10 for the electrical and the optical channels. Since the electrical pulses are much wider and the amplification gain is larger for the SWAMPs than for the ORBs, the charge is much larger for the electrical channels.
The reconstruction in this thesis still uses the amplitude to determine the number of photons. Since the presently applied reconstruction does not take into account the number of photons, the results will not change. However, a more advanced reconstruction would benefit from the expected improved resolution.

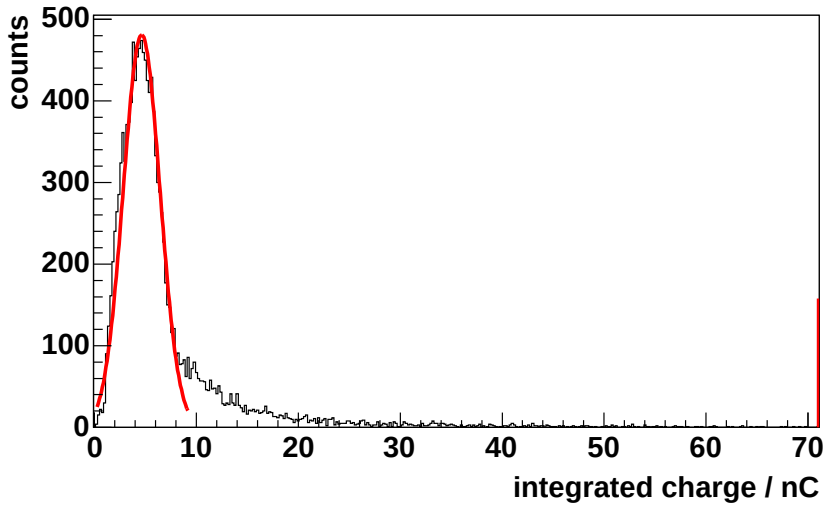

Figure 5.9: The charge distribution of OM 56 (electrical channel). The size of the single photo electron pulse is determined by a gaussian fit. The line shown at the upper end of the distribution represents the largest charge observed in this run.

5.2 Comparison of the performance of MuonDaq and TWRDaq

The first test on the TWR data consists of a comparison of the data taken with MuonDaq and TWRDaq. Again the combined data set, called merged data, is used. The goal is to confirm that the merging procedure is working well and to investigate the dynamic ranges and the stability of the measurements.
Using the algorithm as described above, the pulses are detected and the hit information is extracted from the waveforms.

5.2.1 Hit efficiency

While the TDC collects the pulses in a time window of 34 μs, the TWR in its present configuration measures the incoming signals in a total time window of 10.24 μs around the trigger. Figure 5.11 displays the distribution of the pulse onset times obtained from TDC and TWR after time calibration. The limited TWR time window is clearly visible. The TWRDaq loses mainly after-pulses, which arrive several microseconds after the event. In order to obtain an estimate for the hit efficiency and pulse resolution of the TWRDaq,

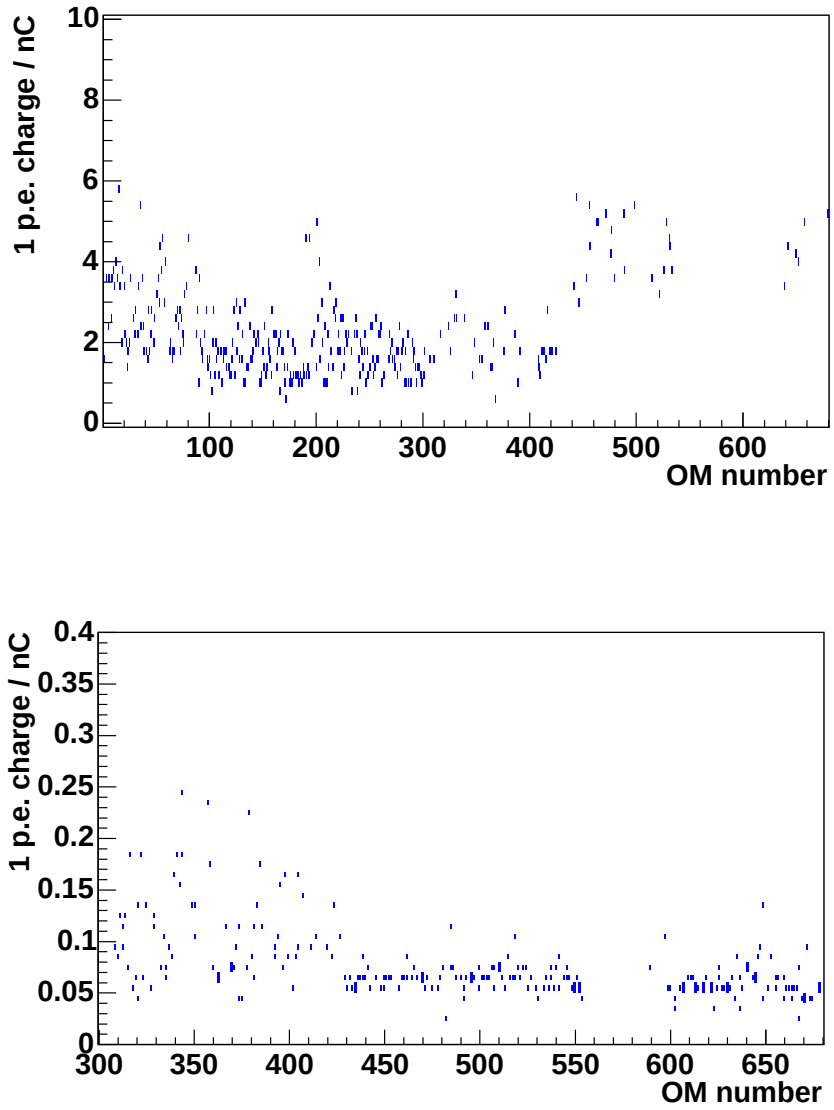

Figure 5.10: The mean charge of a single photo electron pulse of the electrical (top) and optical channels (bottom).

the number of pulses found by both DAQs in the TWR time window has to be compared. Figure 5.11 shows the leading edge distribution of the TDC hits and the TWR pulses for one OM. The TWR time window is clearly visible and is determined and reduced in order to avoid side effects on both sides by about 200 ns. The relative *pulse rate ratio,* η, of the sum of all hits in the reduced time window of both DAQs gives an estimate of the hit efficiency. η

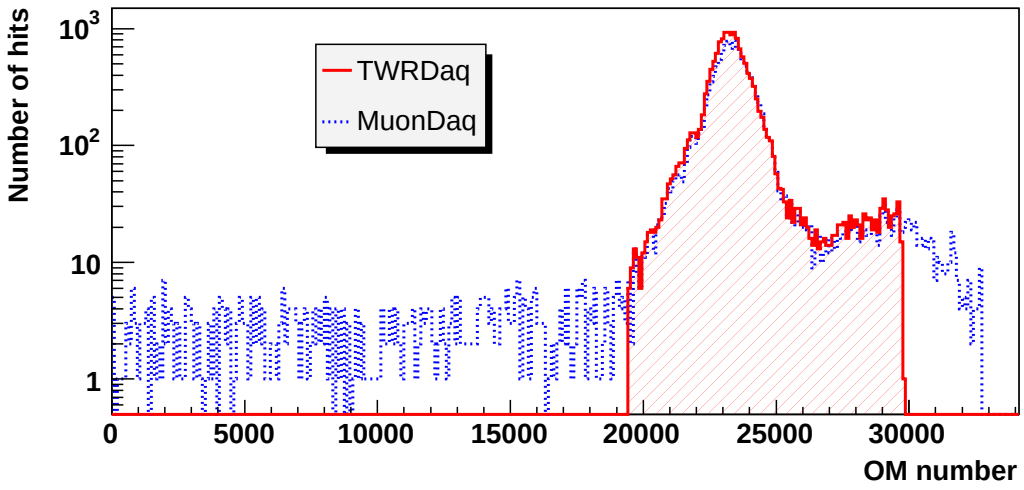

Figure 5.11: The leading edge distribution of OM 516 using data from the MuonDaq and the TWRDaq. The dashed histogram contains the hits measured by the TWRDaq.

is defined as

$$\eta = \frac{\text{detected pulses in TWRDaq}}{\text{detected pulses in MuonDaq}} .$$

Since the AMANDA detector uses several types of analogue signal transmission techniques with different resolutions for the pulse separation, the results are split into several plots for each type of signal transmission. The hit efficiency for the first four strings of the detector, using coaxial cables for signal transmission, is displayed in figure 5.12 (top). The diagrams for all other types of signal transmission can be found in the appendix A.2.1. In order to get an estimate for hit efficiency of every group of channels, the distribution of pulse rate ratios is displayed in figure 5.12 (bottom). The mean and the RMS of these distributions are summarised in table 5.1.
In principle, the relative pulse rate ratio is larger for optical signal transmission, which can be explained by the lower detection threshold for the TWRDaq applied to these channels. While the TWRDaq uses thresholds between 15 mV and 25 mV for the optical channels, the MuonDaq threshold for these channels varies between 50 mV and 60 mV. In contrast, the TWRDaq detection threshold for the electrical channels is higher in order to reduce the amount of data. While the threshold is about 180 mV for the TWRDaq, the threshold

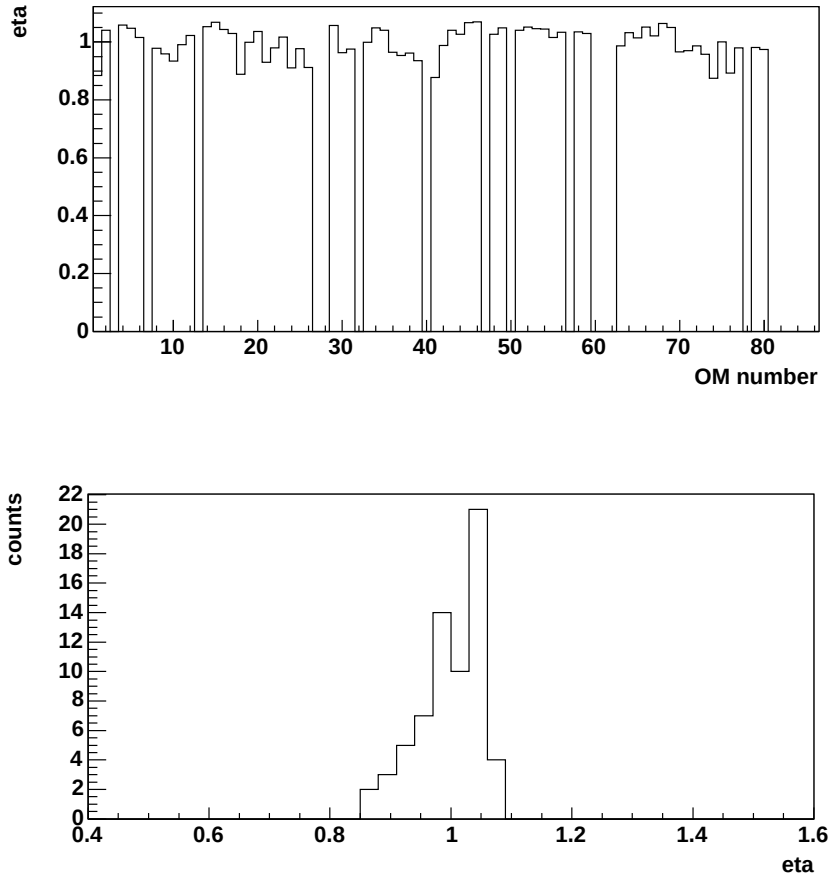

Figure 5.12: Hit efficiency for the first 4 strings. The ratio of pulses, η, for each OM is shown above, while the distribution of η is shown below.

String	Type of analogue transmission	Average η	RMS of η	th_{det} TWRDaq mV	th_{det} MuonDaq mV
1 - 4	electrical	0.97	0.08	180	100
5 - 10	electrical	1.08	0.05	180	140
11 - 13	optical	1.14	0.04	15 - 25	60
11 - 13	electrical	0.99	0.08	180	100 - 150
14 - 19	optical	1.18	0.09	15 - 25	50
14 - 19	electrical	0.98	0.11	180	200

Table 5.1: The distribution of relative pulse rate ratios for different types of analogue signal transmission.

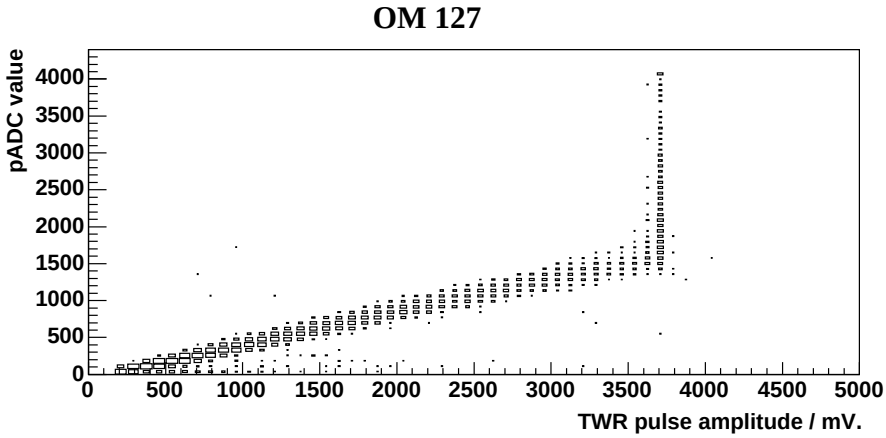

Figure 5.13: The relation between the pulse amplitude of the largest pulse in the waveform and the pADC value from MuonDaq for an electrical channel (OM 127). The pADC value corresponds to mV.

for the MuonDaq is about 100 mV for the first four strings and about 140 mV for the strings 5 to 10. This effect is partly balanced by the higher resolution in pulse separation that increases the number of pulses in the TWRDaq.
One result of this investigation is the loss of pulses due to higher TWR thresholds, th_{det}, for the electrical channels. The value of th_{det} will be re-optimised in the coming season.

5.2.2 Amplitude and dynamic ranges

While the pADC uses the delayed output, the TWR is connected to the prompt output of the SWAMPs or ORBs. Both outputs have different amplification characteristics. The gain of the prompt output of the SWAMP is larger than the gain of the delayed output by a factor of $\sim$3.

A simple test of the stability of both DAQs is to compare the observed pulse amplitudes. Figure 5.13 shows the relation between the amplitude of the largest pulse found in the waveform and the pADC value for an electrical channel. The correct association of the pulses results in a linear relation. The histogram clearly shows the limitation of the voltage range of the TWR. The fact that the TWR saturates earlier is caused by the higher amplifier gain of the prompt output. The total voltage range of the TWR is 5 V, reaching from approximately +1.2 V to -3.8 V. The amplitude of the waveform pulses saturates at around 3.7 V.

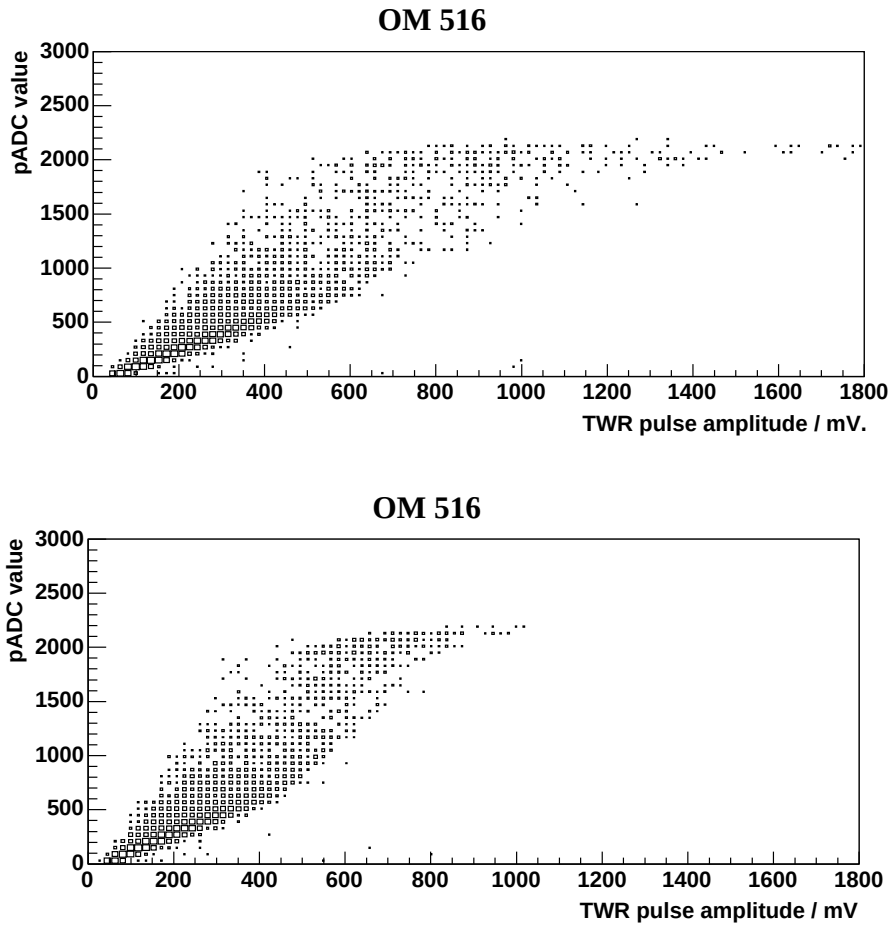

Figure 5.14: The relation between the pulse amplitude of the largest pulse in the TWR and the pADC value from MuonDaq for an optical channel (OM 516). The diagram above shows the relation without application of the amplitude fit procedure and the lower diagram shows it using using the procedure. The pADC value corresponds to mV.

The saturation of the pADC [1] is also visible around pADC = 4096 mV.

Figure 5.14 (top) displays the corresponding relation for an optical channel. While the signals of the electrical channels are comparatively large and often exceed the dynamic range of the TWR and the pADC, the signals of the optical channels are smaller and are limited by the maximum output voltage of the ORB. The linear correlation is not as good as for the electrical channels. Due to the narrow pulses, the TWR, with its limited sampling resolution of 10 ns, may miss the pulse maximum, which leads to an underestimation of the pulse

[1] The pADC has a digital range of 12 bit (0..4095 digits).

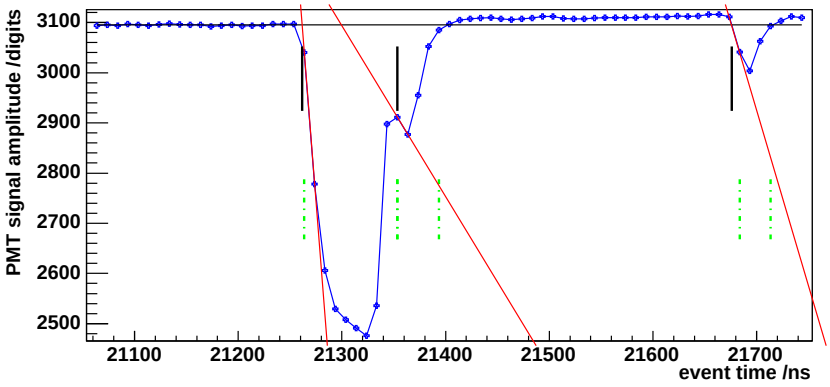

Figure 5.15: A waveform of OM 516 demonstrating the degradation of the amplifier gain for larger amplitudes.

amplitude. In case of the ORB the relation is more complicated. The pADC is capable of measuring the maximum amplitude of the PMT pulse only if the pulse width is larger than 50 ns. The PMT pulses of the optical channels have a typical width of 10 ns to 30 ns. A pulse shaper, contained in the ORBs, solves this problem by spreading the pulses. In case of multiple pulses, the widened pulses overlap and the correct amplitude information is lost.
In addition, the large spread of the pADC values at a given waveform amplitude can be understood by the error caused by missing the pulse maximum amplitude in the TWR. The amplitude resolution of the TWR can be improved by applying a linear fit of the leading and the trailing edge of the pulse. The crossing point of the tangents is considered as a better estimate for the pulse amplitude. The result is displayed in figure 5.14 (lower diagram). The dynamic range of the TWR amplitude has increased. However, the spread of the ratio of the pADC and TWR amplitude is still large.

In addition, the amplifier gain of the ORBs changes for large amplitudes. A very large waveform pulse of OM 516 is shown in figure 5.15. Above an amplitude of 400 mV the pulse shape degrades and starts to saturate. Due to the higher amplification gain, the prompt output starts to saturate much earlier as can be seen in the figure.
Finally, the maximum number of recorded pulses has to be considered. The total number of recorded edges in the TDC is limited to 16 edges corresponding to 8 pulses with a leading and a trailing edge each. The time window of the TDC is about 34 μs, while the TWR samples the signal in a window of about 10 μs.

Figure 5.16 shows the distribution of the number of pulses found in the waveforms and the number of leading edges in the TDC. As can be seen, the number of pulses in the TDC shows a peak around eight and decreases rapidly

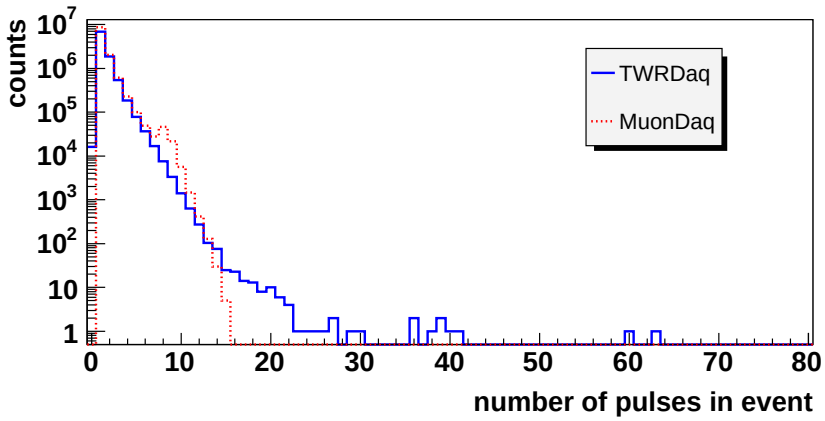

Figure 5.16: The distribution of the number of pulses per channel.

for larger numbers, while the number of pulses in the waveform extends to up to 30.
As described in section 3.2, the TDC may miss trailing edges making it possible to store additional leading edges in the free memory space. A total number of up to 16 pulses can appear. OMs with more than eight leading edges do not contain the full information of each pulse, since the corresponding trailing edges are lost.

The integrated charge forms can be used as a measure for the number of photons contained in a pulse. Figure 5.17 displays the relation between the integrated charge of the largest pulse in the waveform and the pADC value from the MuonDaq. Again, the limitation of dynamic range for the pADC is clearly visible for the electrical channel. Due to the higher amplification gain of the prompt output, the relation between charge and pADC value slightly degrades above pADC = 2000 when reaching the voltage limit of the TWR.

An important property of the DAQ systems is the dynamic range for the photon counting. Using the pulse amplitude as a measure for the number of photons in a pulse, the dynamic range is determined by the ratio of the size of the largest obtained pulse and the average size of a single photo electron pulse. The distributions of the dynamic ranges for the pADC and the TWR are displayed in figure 5.18. It is clearly visible that the dynamic range for the TWR is apparently smaller by a factor of about 2 to 3. While the total voltage ranges of both devices are of the same order (pADC: 4.096 V; TWR: $\sim$3.8 V), the amplification gain of the prompt output used by the TWR and the delayed output used by the pADC differ by a factor of $\sim$3. Thus, in order to obtain a larger dynamic range for the TWR, the amplification gain of the prompt output or the HV of the PMT has to be reduced.

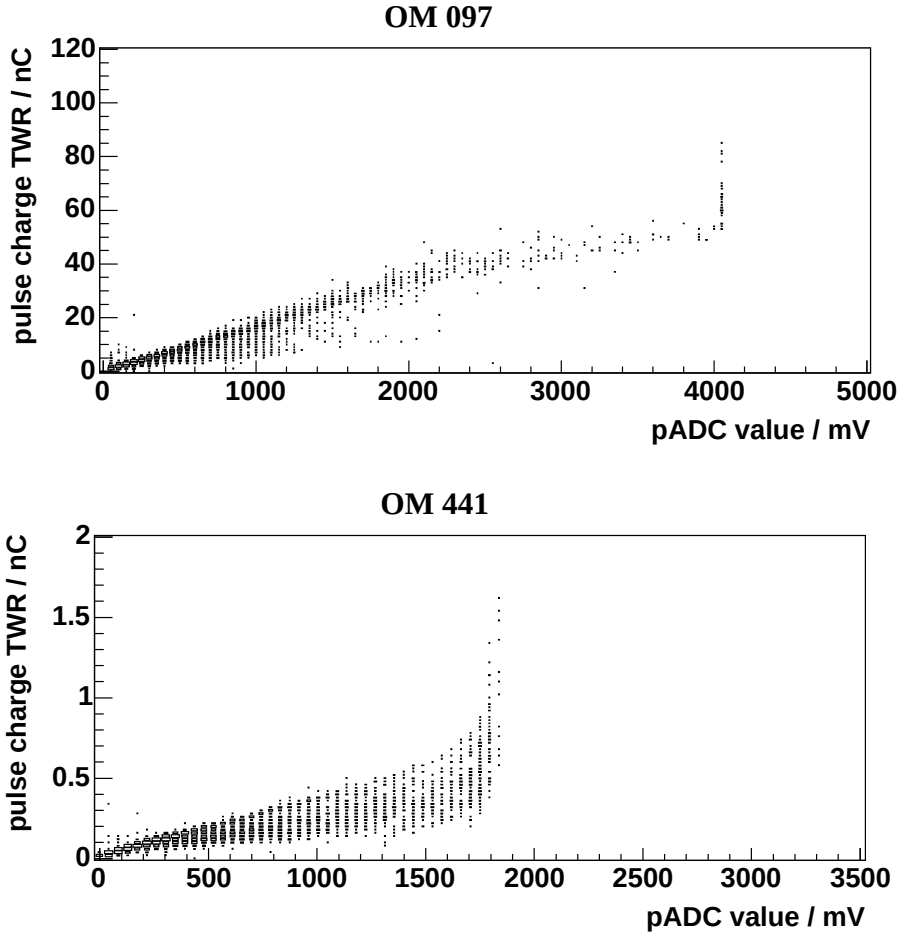

Figure 5.17: The relation between the integrated charge of the largest pulse in the waveform and the the corresponding pADC value from the MuonDaq. The diagram above shows an electrical channel (OM 97), below an optical channel (OM 441).

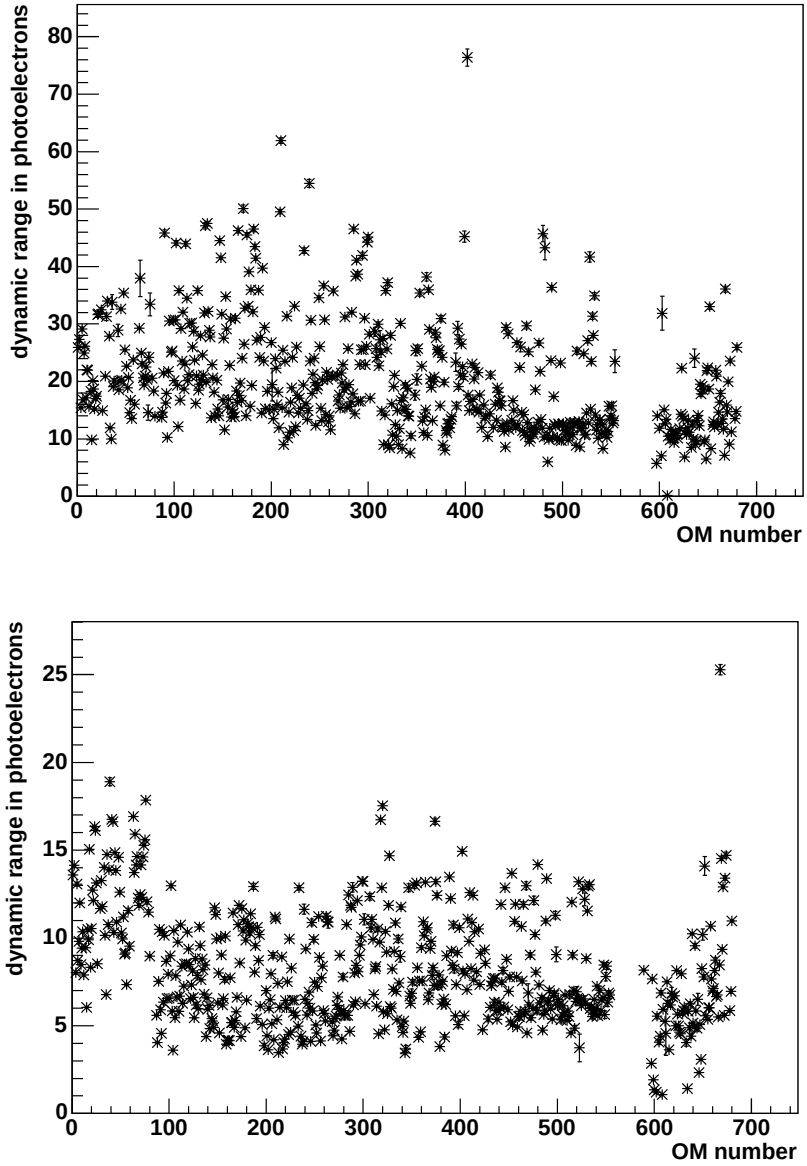

Figure 5.18: The dynamic range for photon counting using the pulse amplitude as a measure for the number of photons with the MuonDaq. Above shows the distribution of the dynamic ranges of all channels using the pADC, below the distribution using the TWRs.

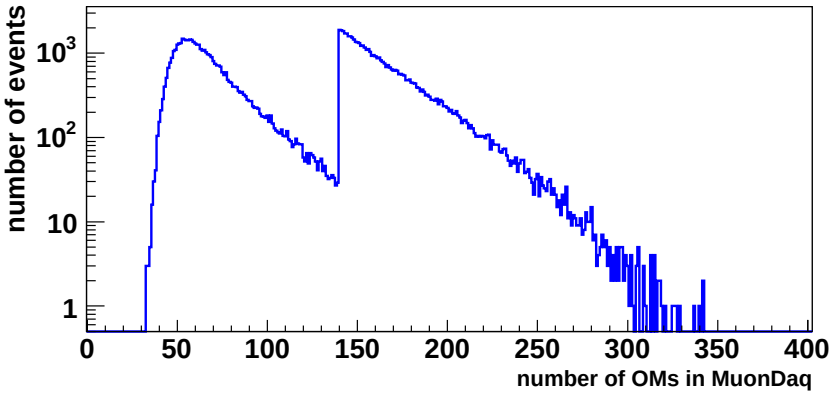

Figure 5.19: The distribution of the number of hit OMs per event in the MuonDaq for "merged data" in 2003.

5.2.3 Muon track reconstruction

The aim of this first track reconstruction using data from TWRDaq is to demonstrate that the reconstruction with data from TWRDaq gives the same result as with data from the MuonDaq. For this purpose "Merged data" containing both data from MuonDaq and from TWRDaq is used. The filtering and merging process is described in section 4.2.5. The comparison is an essential test for all other following analyses with TWR data. It has to be mentioned that the merged data set is not a pure sample of unbiased events, but is enriched with high multiplicity events. For the analysis presented in this thesis data from 2003 was used. The selected high multiplicity events have more than 140 hit OMs in the MuonDaq. Figure 5.19 shows the distribution of hit OMs in the MuonDaq per event.
For the reconstruction the original AMANDA reconstruction software is used, which uses the information that is available in the MuonDaq. Hits from the MuonDaq contain the leading edge time and the *time over threshold, TOT*. The pADC value is usually associated with all hits within a time window around the trigger time. From the TWR data a similar dataset for every hit has been extracted using the algorithms, as described in the previous sections. Thus, the data from TWRDaq differs from the MuonDaq dataset by

- individual amplitude values, which are extracted from each pulse shape,
- a different procedure to determine the leading edge time,
- and a better separation of overlapping pulses.

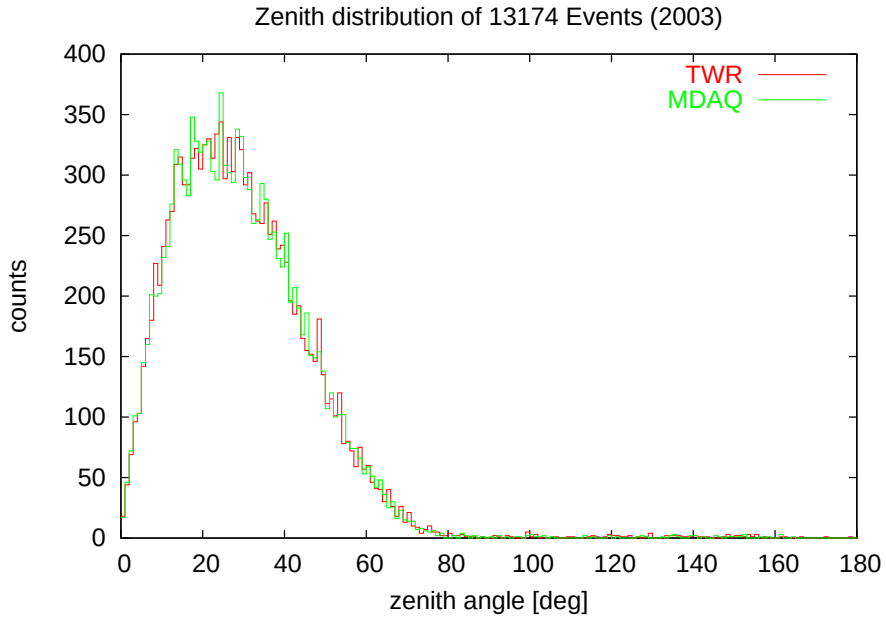

Figure 5.20: The distribution of the zenith angle obtained from reconstruction with data from TWRDaq and MuonDaq.

For the reconstruction algorithm, which is applied in this thesis, only the leading edges are utilised. Channels with a high noise rate or instabilities are excluded from the reconstruction. This procedure is termed *hit cleaning*. Only the TOT and the pADC value are used for the hit cleaning.

Figure 5.20 shows the distribution of the zenith angle obtained from reconstruction with TWR data and MuonDaq. The results for both DAQs are similar and do not show any systematic features. Thus, the hit extraction followed by the standard reconstruction with data from TWRDaq gives the same result as with MuonDaq.

The distribution of the angle between the MuonDaq and TWRDaq reconstruction results is displayed in figure 5.21, while the corresponding cumulative distribution is shown in figure 5.22. The results show that the median of the angular difference is about 1°, which is less than the angular resolution of the AMANDA detector, which is assumed to be $\sim 3°$ on tracks[2]. Thus, the reconstruction with data from TWRDaq gives similar results to the reconstruction with data from the MuonDaq. This analysis has been done without applying quality checks on the reconstructed tracks.

[2]This assumption is based on Monte Carlo data. Muon tracks have been generated using the software package dCorsika (2001) and the response of the AMANDA has been simulated. The median of the angular difference between simulated track and reconstructed track is assumed as measure for the angular resolution.

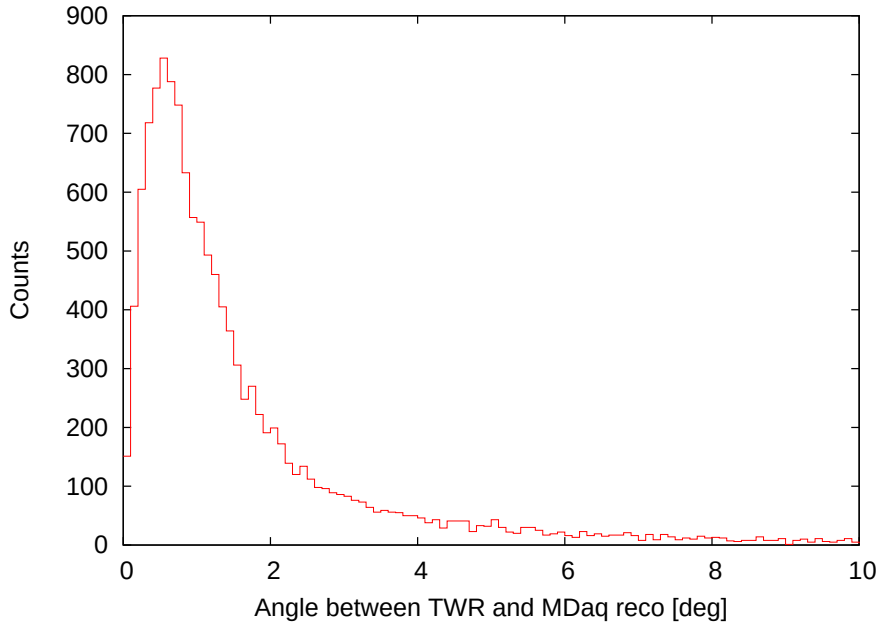

Figure 5.21: The distribution of the angle between the MuonDaq and TWRDaq reconstruction.

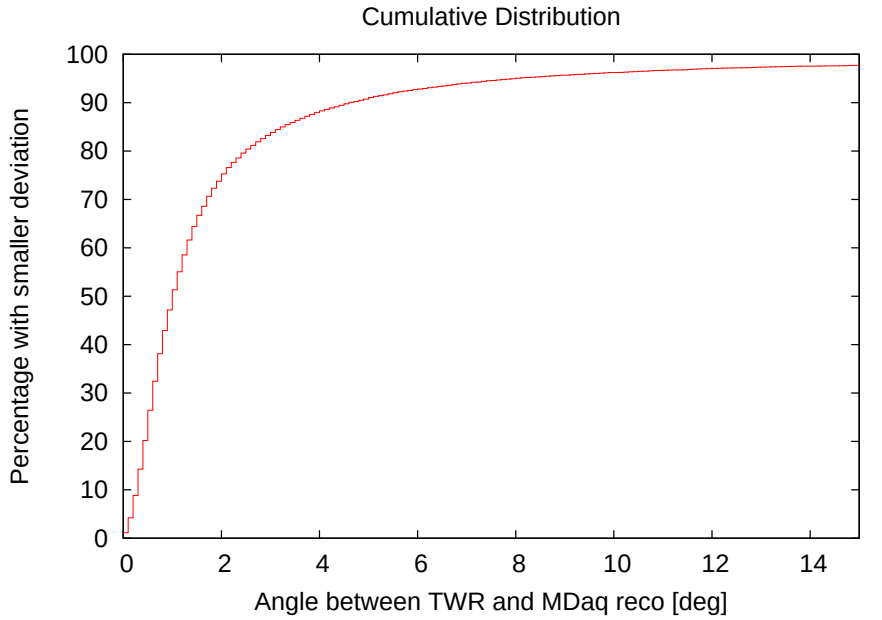

Figure 5.22: The integrated distribution of the angle between the MuonDaq and TWRDaq reconstruction representing the percentage of events with a smaller angular difference.

5.3 Estimation of the reconstruction quality

In experimental data, the true muon track direction is not known and it is difficult to determine the angular resolution of a reconstruction. In fact, this is possible for simulated data with a known track. As the Monte Carlo implementation into the detector simulation is still in a testing phase, the accuracy is probably not sufficient for a full comparison of the resolution of MuonDaq and TWRDaq. However, it is possible to investigate improvements and degradation of the reconstruction with respect to the MuonDaq using the following method. The general idea is to split all hits of an event into two subsamples of equal size. Since the hits originate from the same event being distributed randomly into two subsamples, a reconstruction with the subsamples of hits should yield a similar result. Of course, this procedure only gives good results for events with a larger number of hits, since each subsample will contain only half of the hits and the resolution will degrade significantly for a smaller number of hits [Rib].
All hit channels are ordered by the time of their first hit in a numbered list. In order to produce the subsamples, all hits of even numbered channels are combined into one subsample, *even*, whereas the other hits are collected in a subsample called *odd*. In order to produce subsamples containing the complete time window of the physical event, the hits are ordered by time. OMs which are not connected to both DAQs are excluded from the analysis.

The resulting distribution of the angular difference between odd and even reconstruction is displayed in figure 5.23. Smaller differences correspond to a better intrinsic angular resolution. The lower diagram shows the integrated distribution of both DAQs. The median of this distribution can serve as an indicator for a comparison. As can be seen, the result is slightly worse for the TWRDaq. While for the MuonDaq the median is around $\sim 4.1°$, the TWRDaq is $\sim 4.4°$ including all events.

The dependence of the median of the angular difference distribution and the number of channels in the event is displayed in figure 5.24 (top). The reconstruction results are stable above a number of participating OMs of about 40, corresponding to an average number of channels of 20 in each subsample. Furthermore, with increasing number of channels, the reconstruction becomes more stable, as the median angle between odd and even decreases.
Despite the fact that the reconstruction does not take into account the additional information delivered by the TWRDaq, the results show that the reconstruction is comparable to the MuonDaq results. In addition, figure 5.24 shows an important result. It can be seen that for events with more than 30 hit OMs, the median angle is still below 10 degrees. This means that for the corresponding subsamples with more than 15 hit OMs, the reconstruction still gives reliable results. This is an important piece of information and suggests that a further decrease of the multiplicity threshold is promising.

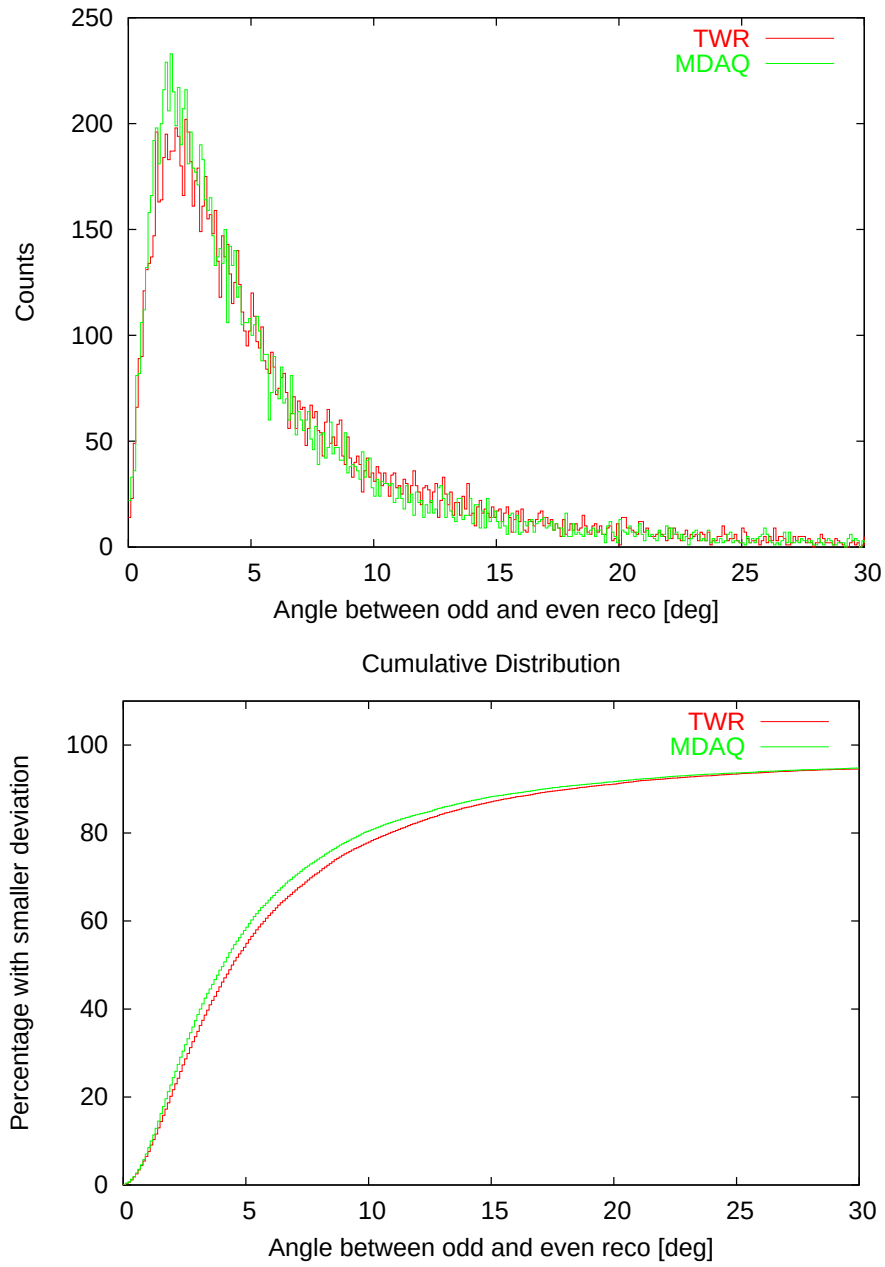

Figure 5.23: The distribution of the angular difference between odd and even sample (top). Below the cumulative distribution. The ordinate corresponds to the percentage of events of smaller angular difference.

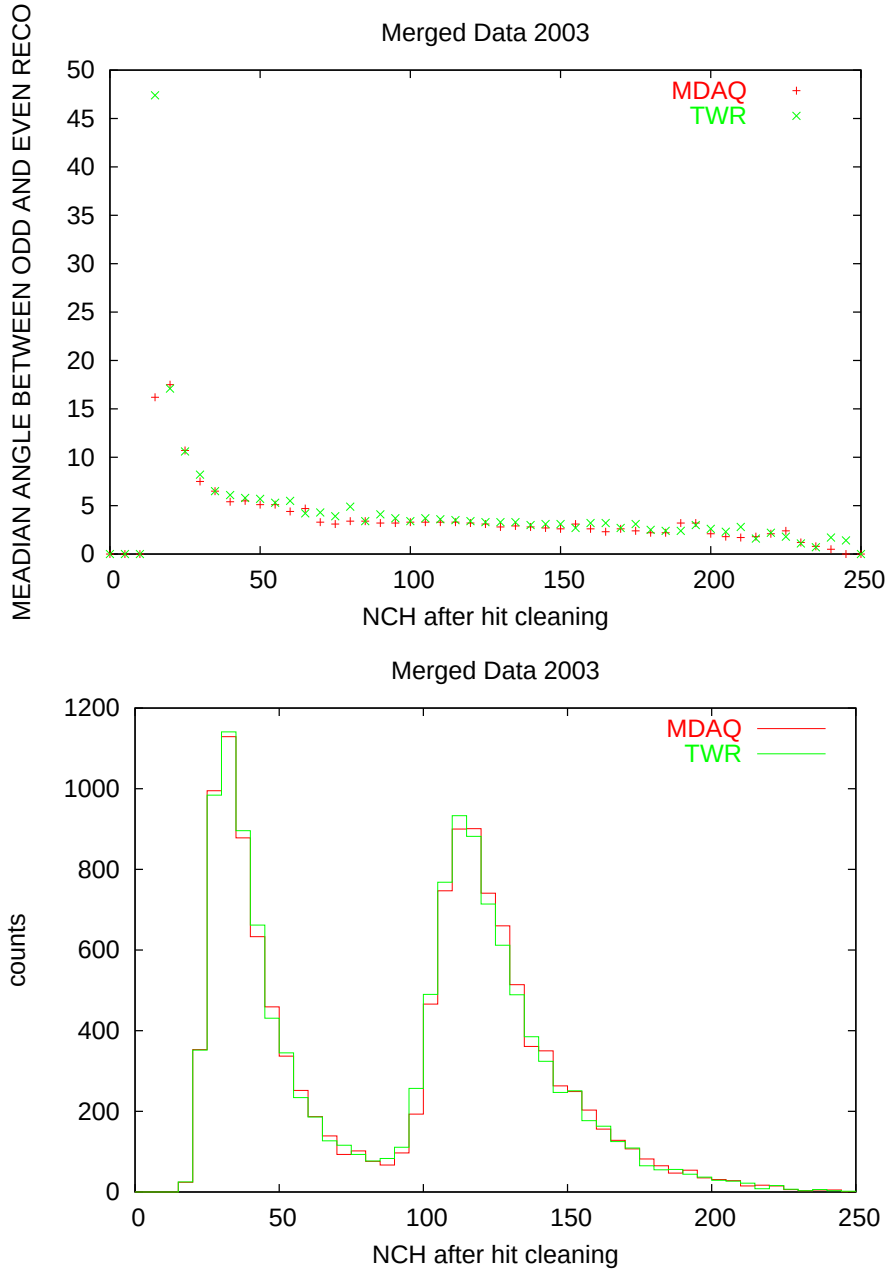

Figure 5.24: The median of the angular difference distribution versus the number of participating channels in the event (top). The corresponding distribution of number of channels in the event (bottom).

5.3.1 Systematic error

The TWR samples the PMT signals with a frequency of 100 MHz which results in a binning of 10 ns and a limited time accuracy. An additional

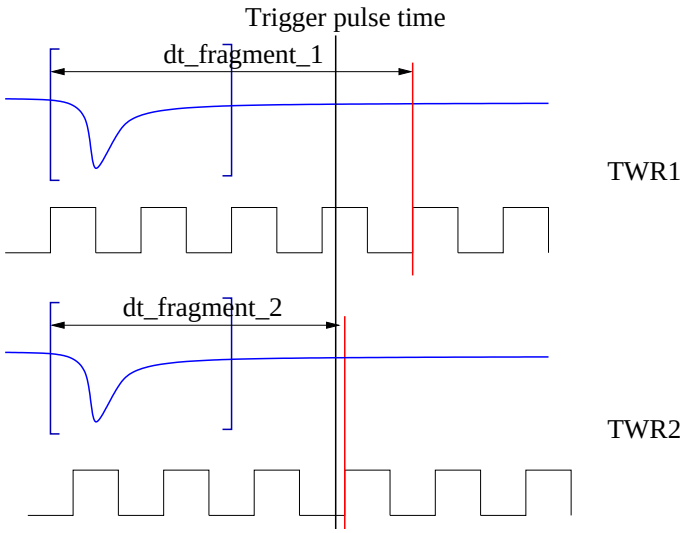

Figure 5.25: Systematic error due to the binning of the TWR.

problem arises from the lack of synchronisation between different TWRs. Every TWR is equipped with a 100 MHz oscillator, which serves as an internal clock. Figure 5.25 illustrates the problem. An incoming trigger is latched by the TWR at the following rising edge of the internal clock. Due to the independent clocks, the time difference between the actual trigger signal and the latching time in a single TWR, a jitter of about 5 ns, limits the time resolution [Nam].
This is the dominant error in time resolution for the optical channels. A solution for this problem will be a global synchronisation of all TWRs using an external oscillator.

5.4 Investigating signal characteristics using the TWRDaq

After-pulses

After-pulses may be caused by residual gas atoms in the PMT. The time between the first direct pulses caused by the photon(s) and the after-pulses are characteristic for each PMT [Leo94]. The distance between the the first pulse in a waveform and every following pulse is displayed in figure 5.26. While the hits with a time distance of less than 3 μs are presumably related to the event, the later pulses can be mostly considered as after-pulses. For

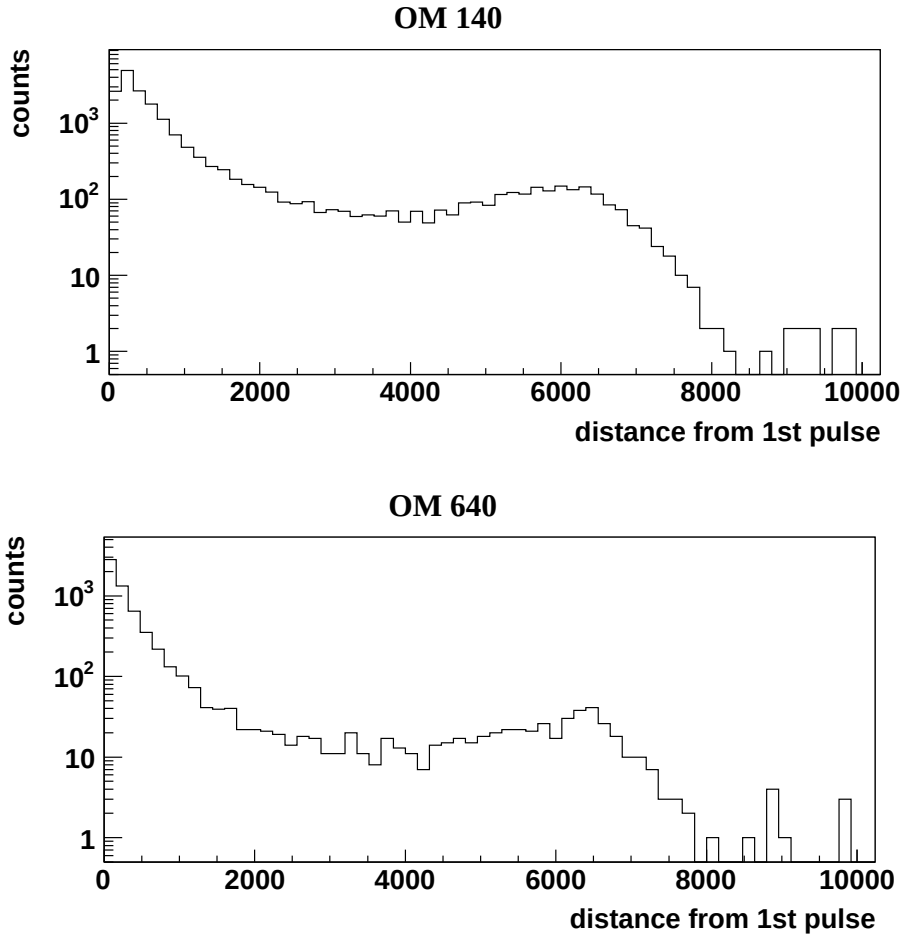

Figure 5.26: The distance between the first pulse in a waveform and every following pulse. Above shows an electrical channel (OM 140), below an optical channel (OM 640).

most of the OMs, a second maximum in the hitrate at about 6 μs after the first occuring pulse is visible. It has to be mentioned that the drop in the hitrate is caused by the time window of the TWR of 10 μs. Since most of the first hits in the TWR window are occurring around 2 μs to 3 μs in the the window, the maximum distance to the window end is about 8 μs.
The TWRDaq can be used to study the shape and the occurrence of afterpulses in order to develop an efficient filter for these pulses.

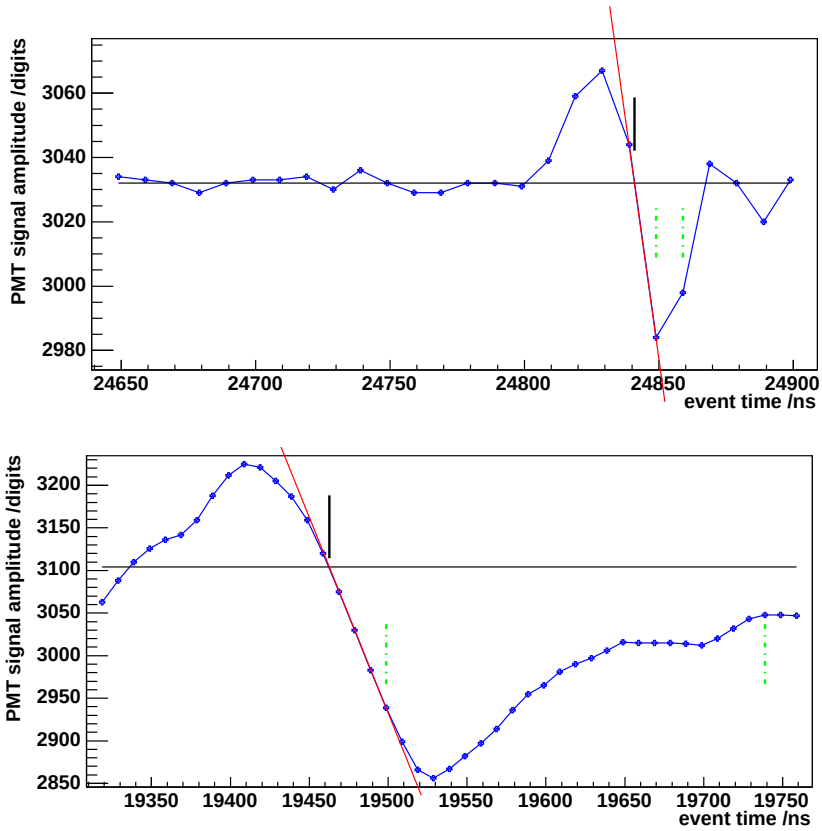

Figure 5.27: Two waveforms with a crosstalk pulse. The crosstolk pulse can be distinguished from a normal PMT pulse by a positive overshot.

5.4.1 Cross talk

Electro-magnetic interference, called *cross talk*, between signal cables or in the dAQ electronics may cause additional pulses. These pulses differ from standard PMT pulses by their appearance, which is clearly visible in the TWR signal shape. Typically, a positive pulse directly followed by a negative pulse of about equal size is visible. A simple filter algorithm may identify *cross talk* This fact can probably be used to identify these pulses to clean the data and make the reconstruction more precise. A cross talk pulse from an optical and an electrical channel are displayed in figure 5.27.

6

Proposal for a TWR based trigger system

6.1 Motivation and general idea

Presently, the AMANDA detector is triggered by the multiplicity trigger or the string-trigger, which is based on local coincidences within one string, see section 3.2. Particles which do not exceed the multiplicity trigger threshold or the string-trigger threshold will not be recorded by the AMANDA detector. The ability to trigger on local coincidences across strings would be a useful trigger for many analyses. Unfortunately, this is not available in the existing system. It is in principle possible via an online analysis of the recorded data. It is currently being investigated, how such a trigger system can be realised and it has been proposed to utilise the TWRDaq to build a software trigger system. Each TWR samples the incoming signal and, as soon as a pulse below the threshold is detected, writes out a hit containing a timestamp and a waveform. The data is collected on a PC, where the trigger software searches the data stream for possible trigger conditions. This chapter describes the first steps towards a software trigger system. The system is still under construction [Mes03].

The layout of the readout system is basically the same as of the current TWRDaq system. Figure 6.1 shows an overview of the proposed system. One major change is the firmware of the TWRs, which has to be changed to enable the TWRs to sample each channel independently. As before an individual fixed threshold is applied to detect signals in each channel. Inside the TWR, the 8 channels are grouped in 4 double-channels, whose signals are sampled in parallel. During readout, the channels have to be separated, since in most cases only one channel contains a signal below the threshold. This task will be done in the DSP.

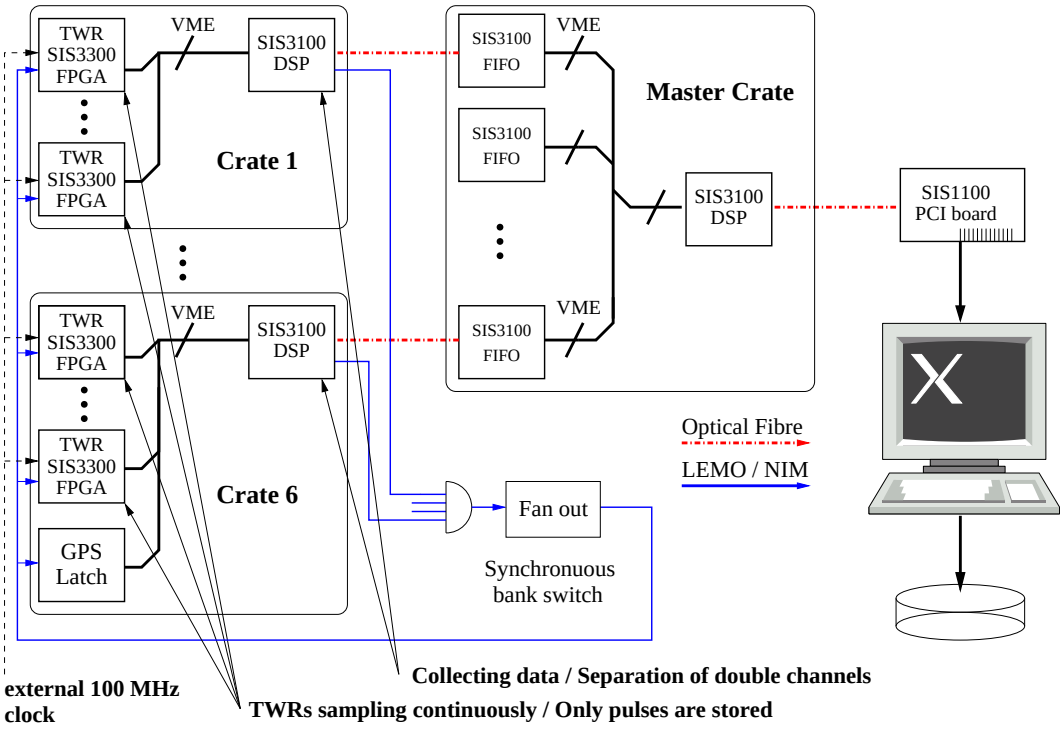

Figure 6.1: The proposed TWR trigger system.

A *TWR hit* consists of a header, a timestamp and the waveform. The header contains the OM number. The internal timestamp of the TWR is used as a measure of the start time of the waveform. In order to guarantee the synchronisation within the whole system, all TWRs are synchronised by an external 100 MHz clock.
Similar to the feature extraction, the waveform contains a programmable number of preceeding and following samples around the pulse. This stream of TWR hits is collected by the DAQ software on the connected PC.
In contrast to the MuonDaq, the timestamps are corrected for cable delays before the trigger search process in order to allow scanning for local coincidences. The TWR hits in each channel are filled in a time-ordered FIFO pipeline. For the trigger search only the start time of the waveform is used, because it is not possible to extract the exact pulse start time from each waveform due to the large amount of data.
Most of the waveforms contain only noise hits. In order to identify time intervals, which possibly contain an event, a pre-trigger search is applied. This process is illustrated in figure 6.2. The timestamps are filled in a histogram with a bin size of several μs. Time intervals of interest are identified by applying a threshold. If the contents of one or several bins exceed the threshold, a

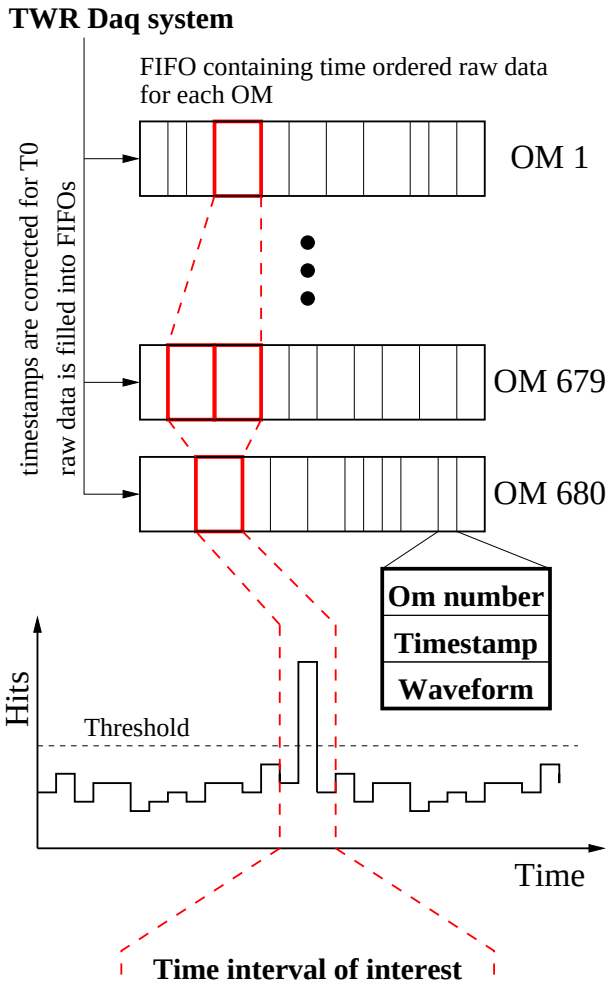

Figure 6.2: Pre-trigger search with TWR data.

time interval of interest is formed including the adjacent bins before and after the bins over threshold. The TWR hits stored in these bins are filled in a histogram and sorted by time.
This list of time sorted events forms the basis for the following search for events. Figure 6.3 illustrates the process of building the multiplicity trigger. For each hit appearing a trigger window of 2.5 μs is added to the multiplicity function. Several hits occurring in one OM, during this trigger window, extend the trigger window further. A trigger is launched if the multiplicity function exceeds a preset threshold.
In the new TWR trigger system two thresholds are used. If the multiplicity function exceeds the higher threshold $\mathrm{th}_{\mathrm{mult}}$, a multiplicity event is built from all hits around the trigger time. Events that exceed only the lower $\mathrm{th}_{\mathrm{local}}$ are tested for local coincidences using more advanced algorithms.

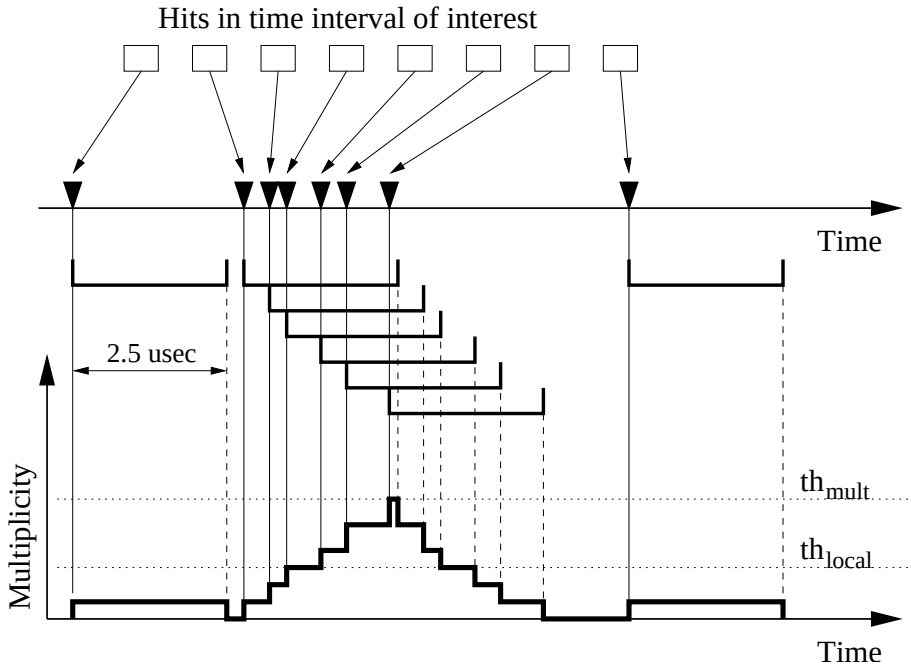

Figure 6.3: Multiplicity trigger search with TWR hits. Each hit OM adds a 2.5 μs "rectangle" starting with the waveform start time to the multiplicity function. A second hit in the same OM extends the rectangle of the OM but does not add a new rectangle. A trigger is found if the multiplicity function reaches a certain threshold.

In principle, a variety of different trigger conditions are possible. Among them, a multiplicity trigger, considering n channels with at least one hit in a time window dT serves as a basic condition. Since accidental coincidences will dominate the recorded events at low multiplicity thresholds, an additional trigger condition is useful to detect local coincidences and distinguish them from accidental coincidences. The additional trigger condition can:

- be a local coincidence within one string. N hit OMs within a row of M adjacent OMs in one string – **string trigger**.

- require in a time window dT that more than N hit OMs in a certain (spherical) volume V with radius R and centre $\vec{X}$ – **cluster trigger I**:

$$M = \{\vec{x}_k| \quad |\vec{x}_k - \vec{X}| < R\} \quad \text{with} \quad \|M\| > N\,,$$

  where $\|M\|$ is the number of elements in M.

- require in a time window dT that more than N hit OMs which fulfil a compactness condition in space – **cluster trigger II**:

$$\sum_{k=0}^{n} \frac{|\vec{x}_k - \vec{X}|}{n} < C_{\mathrm{II}}$$

  where $\vec{X}$ is the centre of gravity of the hit OMs and C_{II} is the compactness threshold.

- require in a time window dT that more than N hit OMs which fulfil a compactness condition in space and time – **cluster trigger III**:

$$\sum_{k=0}^{n} \frac{|\vec{x}_k - \vec{X}| \cdot |t_k - T_{\mathrm{m}}|}{n} < C_{\mathrm{III}}$$

  where T_{m} is the average time of the hits in the time interval dT, $\vec{X}$ is the centre of gravity of the n hits and C_{III} is the compactness threshold.

- require in a time window dT more than N OMs, with at least one hit OM in a volume with radius R around the OM – **neighbourhood trigger**:

$$M = \{\vec{x}_k| \quad \exists i \quad \text{with} \quad i < k \wedge |\vec{x}_k - \vec{x}_i| < R\} \text{ with } \quad \|M\| > N\,,$$

  where $\|M\|$ is the number of elements in M.

- be an **external triggers** e.g. laser calibration or random trigger.

- be a **supernova trigger** based on the noise rate of individual channels.

- be a **special triggers** for slow moving particles.

Since the trigger is formed within an online software analysis the algorithm has to be rather simple. While most of the trigger conditions require a large amount of computing time, the multiplicity trigger and the neighbourhood trigger are based on simple algorithms. Figure 6.4 illustrates the neighbourhood trigger. Hit modules with at least one hit module within a spherical volume with radius R are counted (solid circles) while isolated ones are not counted (dashed circles). This trigger is sensitive to cascade and track-like events.

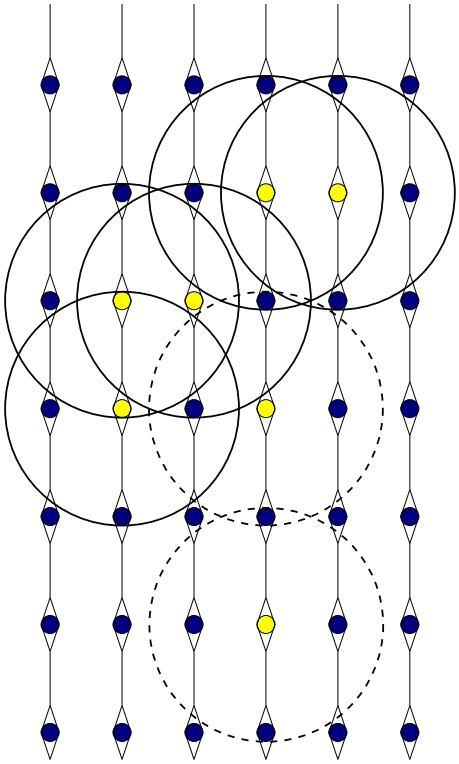

Figure 6.4: The neighbourhood trigger. Only hit OMs with at least one hit OM within a spherical volume with radius R are counted.

7

Résumé and outlook

This thesis describes the design and realisation of a new data taking system for the AMANDA detector. The original DAQ system – the MuonDaq – uses TDCs and peak sensing ADCs to sample the arrival time and amplitude of PMT pulses.
The MuonDaq limits the detector capabilities for various reasons. The information recorded by the MuonDaq is incomplete and ambiguous for high energy events. In addition, the system has a limited dynamic range for photon counting of complex signals.
The main goal of this thesis was to design and install a new AMANDA DAQ system, without the limitations of the MuonDaq. The new system – the TWRDaq – uses Flash ADCs to record the complete waveform of the PMTs. The work started with the installation of a first test system in the Antarctic summer 2001/2002 season with 48 channels. Based on this work, a new system was developed and finally installed in the 2003/2004 season and connected to 576 channels. After one year of successful operation, this system was improved again to achieve higher trigger rates. The number of connected channels increased to 597. This system has now been operating since February 2004. Most of the goals have been fulfilled.
It was shown that the dead time of the new TWRDaq is about 20 μsec and the real dead time in percent of the total number of triggers amounts to only 0.015 ± 0.01 % and 0.018 ± 0.013 % for trigger thresholds of $M = 24$ and $M = 18$ respectively. Thus, the TWRDaq in the present configuration operates almost without dead time. In contrast, the dead time of the MuonDaq amounts to 2.2 msec and results in a data loss of about 15 %.
The current system is externally triggered by the multiplicity trigger of the MuonDaq. In 2003 the multiplicity threshold was set to 24 with a trigger frequency of about 90 Hz. Due to the negligible dead time of the TWRDaq, the multiplicity threshold was lowered from 24 to 18 in the Antarctic summer 2003/2004 resulting in a trigger frequency of 150 Hz. Thus, the sensitivity of

AMANDA for low energy events increased. A hit extraction algorithm and further tools to determine the exact arrival times of the photons and the number of photons in each pulse have been developed. The algorithm uses a dynamic threshold to detect adjacent pulses. Pulses that overlap can be separated by this algorithm. The muon track analysis described in this thesis is based on this algorithm.
While the TDC of the MuonDaq is only capable of measuring up to 16 edges, limiting the dynamic range to 8 pulses, the number of pulses in a waveform from the TWRDaq can exceed 60. High energy events will benefit from this extended dynamic range. The hit extraction algorithm delivers a value for the amplitude of each individual pulse in a waveform. This makes the estimation of the number of photons contained in each pulse more precise, which is important for the energy resolution.
Furthermore, the consistency of the data from the TWRDaq was tested by comparing hits measured by both DAQs. Events from both DAQs are associated by their GPS time and written in a combined data stream, termed *merged data*. One requirement for track reconstruction is an accurate determination of the cable delays between the PMTs. This time calibration was performed before for the MuonDaq. The basic idea of the time calibration presented in this thesis is to determine the time offset between MuonDaq and TWRDaq for each channel, using the merged data. Then the cable delays determined with the MuonDaq are incorporated to determine the final cable delay for each channel. The results show that a timing accuracy between 3.5 ns and 4.5 ns for the optical channels and about 5 ns to 8 ns for the electrical channels can be achieved. This is accurate enough for track reconstruction.
It was shown that the angular difference between reconstructed tracks using TWR data and data from MuonDaq is smaller than the expected angular resolution of AMANDA.
In addition, a different approach was used to estimate the intrinsic track reconstruction quality in both DAQs. Hits from a single track were split into two sub-samples. Track reconstruction was performed with both sub-samples. The angular difference between both reconstructions gives a measure of the track quality. The analysis presented showed that, despite the fact that the reconstruction does not take into account the additional information delivered by the TWRDaq, the reconstruction is comparable to the MuonDaq results.
For events with more than 30 hit OMs, the analysis of the corresponding subsamples with more than 15 hit OMs show a good correlation. This is an important piece of information and suggests that a further decrease of the multiplicity threshold is promising.
The improvements of the detector capabilities and further plans to extend the maximum trigger rate to up to 200 Hz results in a significant increase in data rate, which can be solved without loss of data only by further improvements of the *feature extraction*, a self-developed compression algorithm and by increas-

ing the readout speed of the system.
This thesis describes the successful design, installation and first tests of the new TWRDaq. A complete investigation of all features of the new system is a subject of future work within the AMANDA collaboration.

8

Outlook – Further work

The present system is still triggered by the trigger system of the MuonDaq, using global multiplicity conditions within the whole detector or local coincidence conditions within a single string. An advantage of using devices like TWRs, containing programmable logic like FPGAs, is the potential to build a fast software trigger system. A new firmware for the TWR FPGAs has already been developed [Mes]. First successful tests have already been performed in the 2003/2004 Antarctic summer season. It is proposed to upgrade the TWRDaq in the following Antarctic season again, in order to generate a trigger signal.
The present reconstruction is mainly based upon the leading edge time of the first pulses for each channel. Advanced reconstruction using information from the following pulses is necessary for a further improvement of the reconstruction.
The bandwidth for data transmission from the South Pole to the Northern hemisphere is limited. Therefore, it is necessary to develop an improved compression algorithm for the waveform data [Ref].
The improvement in energy resolution, due to the improved amplitude measurement and the larger dynamic range, will be investigated using the neural net approach [Mun]. A first point source analysis will follow soon after [Gro].
Finally, it has to be mentioned that the experience gained from waveform reconstruction will be an important opportunity for the IceCube collaboration.

Appendix A

Data format

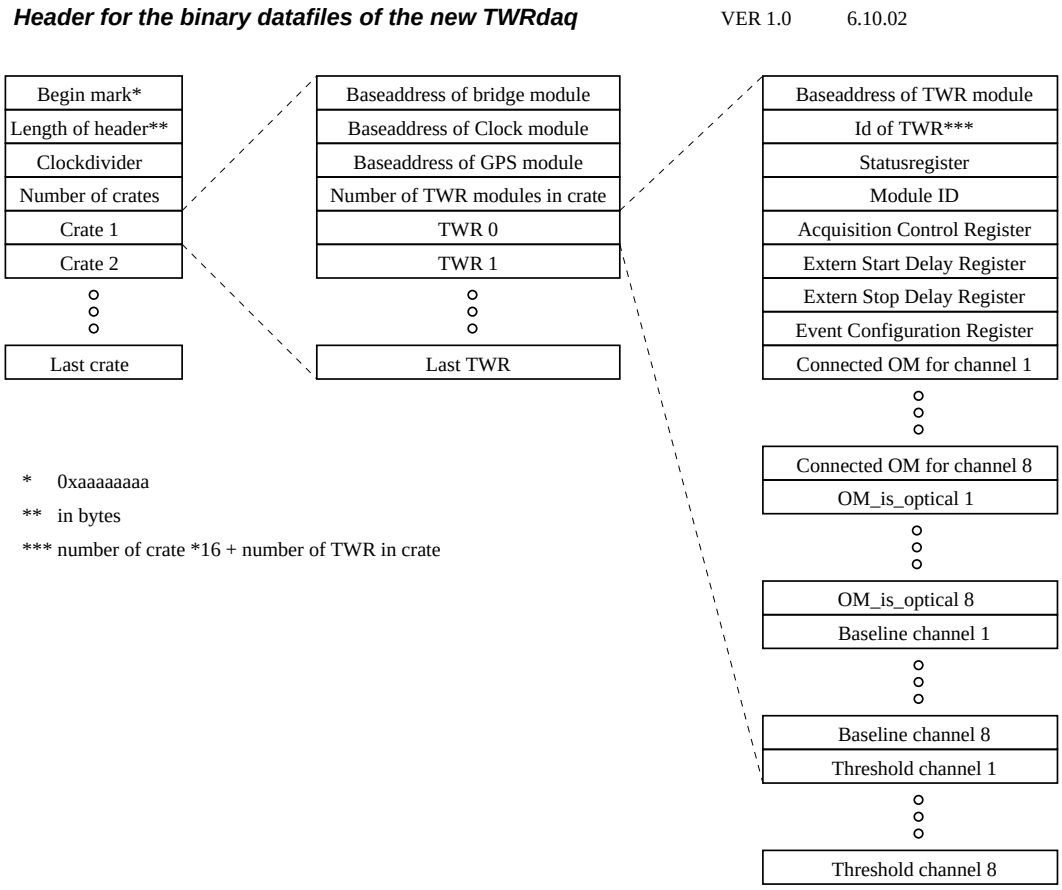

Figure A.1: Header of binaryfile

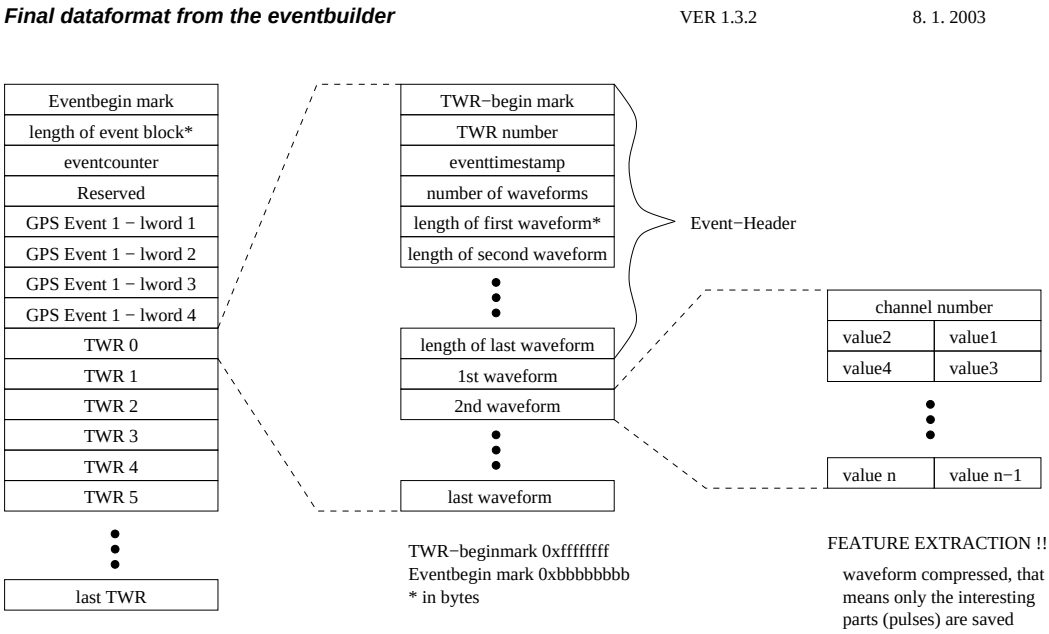

Figure A.2: Dataformat of binaryfile

Waveform data format with feature extraction
only the interesting peaks are saved

VER 1.1
4. 7. 02

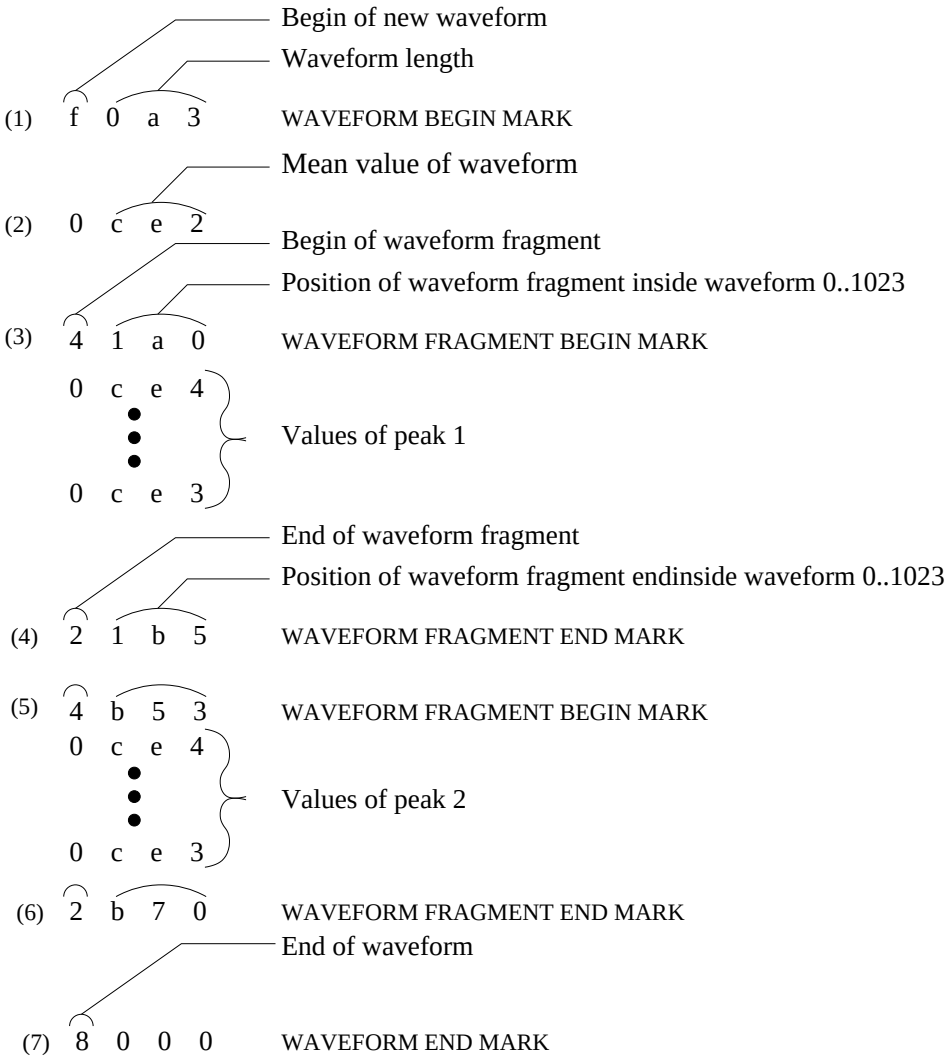

Each waveform begins with WAVEFORM BEGIN MARK accompanyed by the length of the whole waveform in bytes followed by the mean value of the waveform (2). Two waveform fragments are stored in this example beginning with WAVEFORM FRAGMENT BEGIN MARK (3) and (5) accompanyed by the position of the fragment inside the waveform and terminated with a WAVEFORM FRAGMENT END MARK (4) and (6). The waveform is closed by a WAVEFORM END MARK (7). To align the waveform to full 32 bit words, a filling word 0xaaaa is inserted if ne− cessary.

Figure A.3: Dataformat of compressed waveform

A.1 Description of the config file TWR.cnf

The configuration file TWR.cnf contains important information on the system like the number of the connected OMs, the TWRs and the applied threshold. The clock_predivider sets the speed of the internal timestamp counter relative to the TWR frequency of 100 MHz. A value of 100 means that the timestamp-counter is running with a frequency of 100 MHz / 100 = 1 MHz and has an accuracy of 1μsec.

A typical TWR.cnf can be seen here:

GENERAL

/* PCI driver name */
PCI_DRIVER_NAME /usr/local/sis1100/nod/sis1100
`Directory in which the SIS1100 driver is located.`

/* Data output directory */
DATA_OUT_DIRECTORY /export/seal1/datadir/
`Output directory for the data.`

/* Number of 128-event blocks per file */
EVENTBLOCKS_PER_FILE 40
`This number multiplied by 128 gives the number of events per rawdata file.`
/* VLF trigger stuff */
VLF_TRIGGER_VETO 0
DURATION_OF_VETO 60
OVERLAP 3
TIME_0 0
TIME_1 15
TIME_2 30
TIME_3 45
`The GPS latch will produce 4 trigger vetos with a length of DURATION seconds beginning at TIME_0, TIME_1, TIME_2, TIME_3 minutes of each hour. This veto is extended in both directions by OVERLAP seconds.`

/* DSP parameters for Feature Extraction */
PRECEEDING_VALUES_OPTICAL 0x3
FOLLOWING_VALUES_OPTICAL 0x4
PRECEEDING_VALUES_ELECTRICAL 0x10

FOLLOWING_VALUES_ELECTRICAL 0x12
These parameters define how the Pulse Extraction in the DSP works. See 4.2.3

/* clock predivider for internal TWR clock */
CLOCK_PREDIVIDER 1
The clock_predivider sets the speed of the internal timestamp counter relative to the TWR frequency of 100 MHz. A value of 100 means that the timestamp counter is running with a frequency of 100 MHz / 100 = 1 MHz and has an accuracy of 1μsec.

STATUS_REG 0x102
ACQ_CONTROL_REG 0x2b4
EVT_CONFIG_REG 0x2c
TFCC 1022
These values define various parameters for the TWR, for example the waveform window length.

N_CRATES 6
The number of crates holding TWRs.

CRATE_0

/* local VME base of bridge module in master crate */
BASE_BRIDGE 0x04000000
The base address of the local SIS3100 bridge module in the master crate connecting to this remote crate.

/* Sharc program */
/* has to be located in direcory current_daq */
DSP_PROGRAM s3300v61.ldr
The DSP file for the remote SIS3100 bridge module in this crate

BASE_GPS 0x10000000
The remote VME base address of the GPS2VME in this remote crate. If it is set to 0xffffffff there is no GPS2VME in this crate

N_TWR 0x10
The number of TWRs in this crate

BASE_TWR 0x00000000
The VME base address of the first TWR
EXTERN_STRT_DEL 0

```
The start delay for this TWR. It has no meaning for the current
DAQ.
```

EXTERN_STOP_DEL 700

```
The stop delay for this TWR. This number multiplied by 10nsec
defines the delay time for an incoming trigger.  A value of 700
means, that the waveform
covers about 3000nsec before the trigger and 7000nsec after the
trigger.
```

TWR_OM	640	641	643	644	645	646	647	648

```
The number of the conected OM beginning with 1
```

OPTICAL	1	1	0	0	0	0	0	0

```
If the OM is read out by an optical fibre, the value is set to 1
otherwise 0
```

TWR_BASELINE	4000	4000	4000	4000	4000	4000	4000	4000

```
The baseline for the OM. Currently this value has no meaning,
since the baseline is determined automatically at the begin of
each run.
```

TWR_THRESHOLD	20	20	20	20	20	20	20	20

```
The threshold for the channel is determined by:
<determined baseline> - TWR_THRESHOLD and is programmed into
the TWR. The thresholds are manually set and optimized for every
single OM.
```

...

BASE_TWR	0xf0000000							
EXTERN_STRT_DEL	0x0							
EXTERN_STOP_DEL	700							
TWR_OM	123	124	125	126	127	128	129	130
OPTICAL	1	1	0	0	0	0	0	0
TWR_BASELINE	4000	4000	4000	4000	4000	4000	4000	4000
TWR_THRESHOLD	20	20	20	20	20	20	20	20

CRATE_2

BASE_100MHz	0x0
BASE_GPS	0x10000000
N_TWR	0x10

...

A.1.1 Name convention and content of the raw data files

The convention for the binary filenames is

twr_yyyy_ddd_rrrr_ffff.dat in 2003

twr_yyyy_ddd_rrrr_ffff_bbbbb_eeeee.dat in 2004

with

yyyy	year
dddd	day in year
rrrr	run number as received from muon daq
ffff	file number incremented with every new file of actual run
bbbbb	time of first event in file in seconds of actual day
eeeee	time of last event in file in seconds of actual day

The header of the raw data file contains the whole structure of the system and all important numbers, like the threshold applied for the pulse detection used for Feature Extraction. Figure A.1 shows the structure of the header.

A.2 Additional diagrams

A.2.1 Hit efficiency

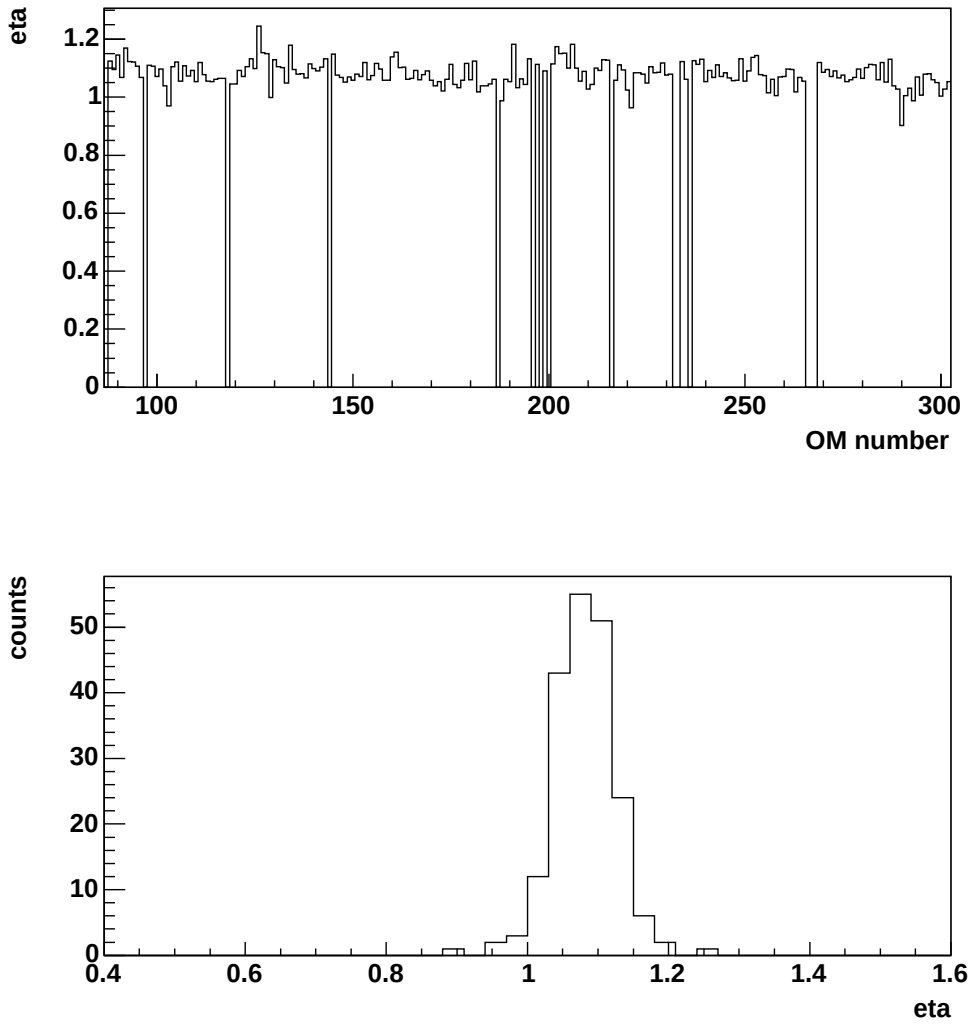

Figure A.4: Hit efficiency for strings 5 to 10. The the ratio of pulses η for each OM is shown above, while the distribution of η is shown below.

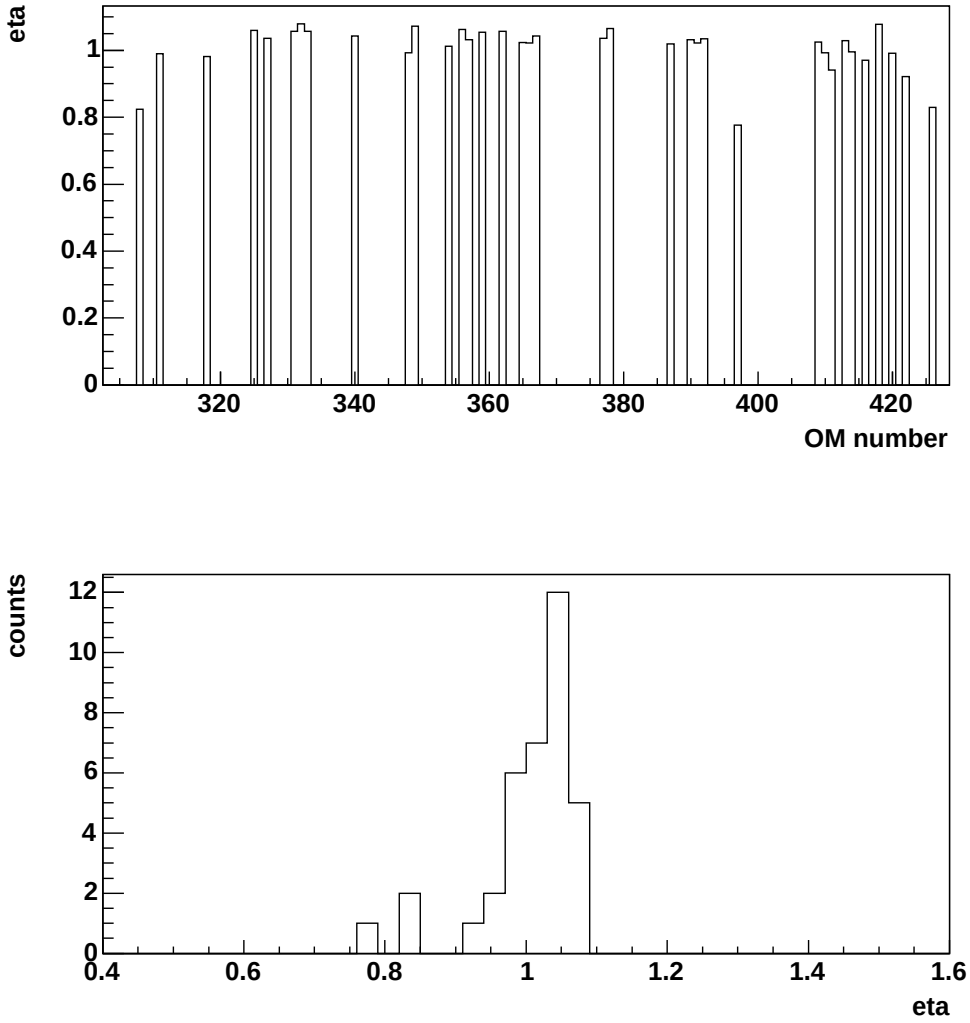

Figure A.5: Hit efficiency for the electrical OMs in strings 11 to 13. The the ratio of pulses η for each OM is shown above, while the distribution of η is shown below.

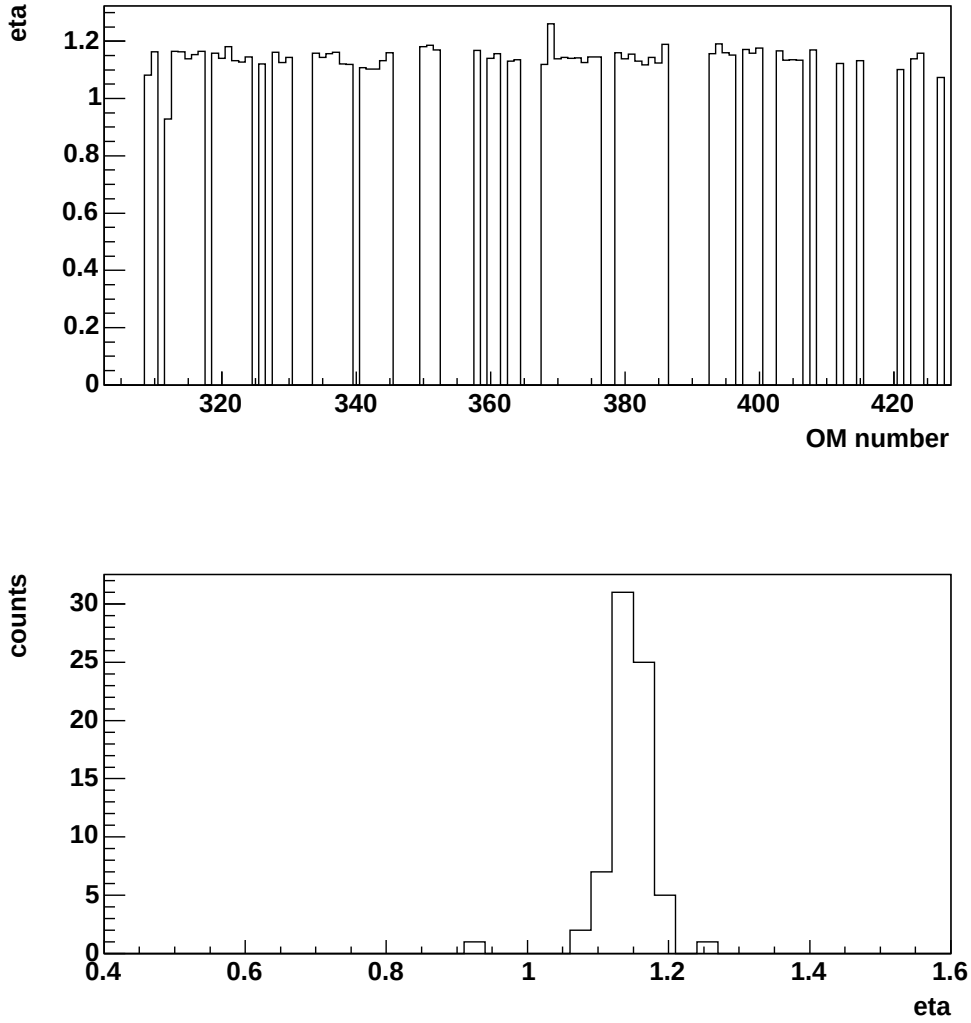

Figure A.6: Hit efficiency for the optical OMs in strings 11 to 13. The the ratio of pulses η for each OM is shown above, while the distribution of η is shown below.

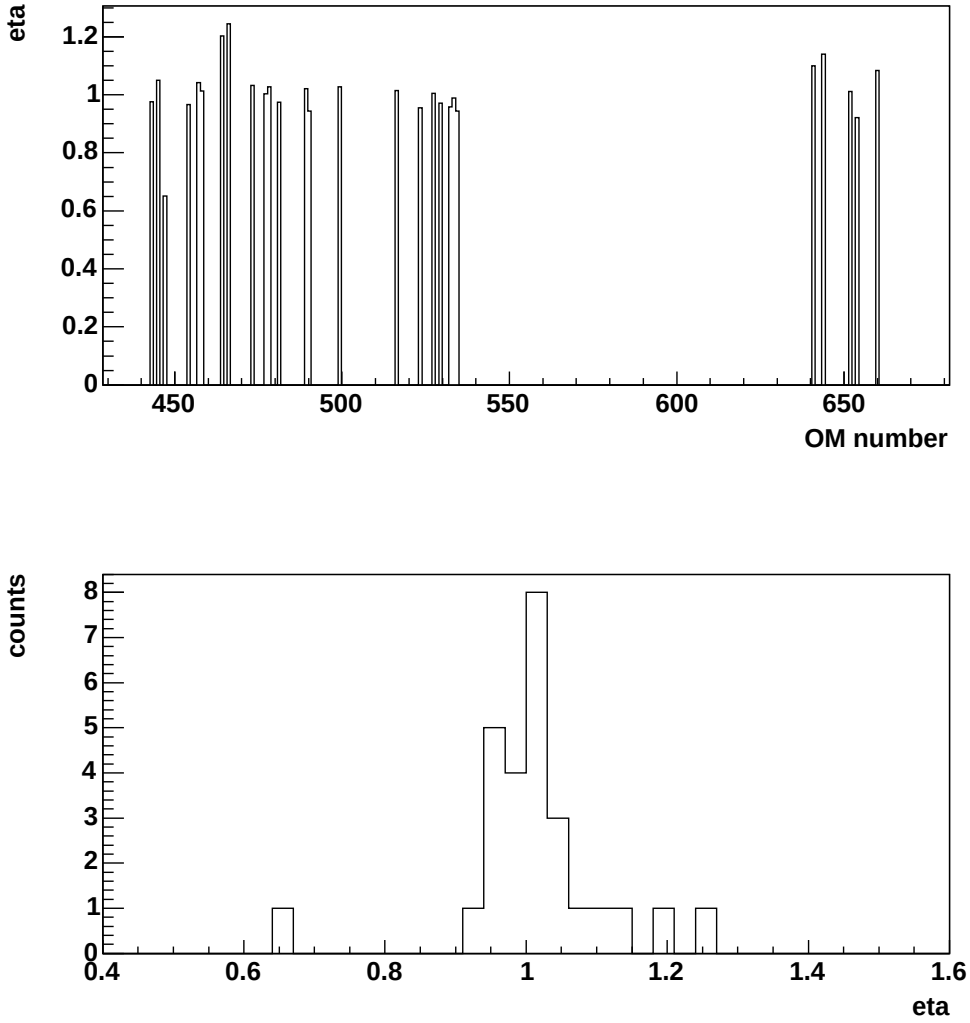

Figure A.7: Hit efficiency for the electrical OMs in strings 14 to 19. The the ratio of pulses η for each OM is shown above, while the distribution of η is shown below.

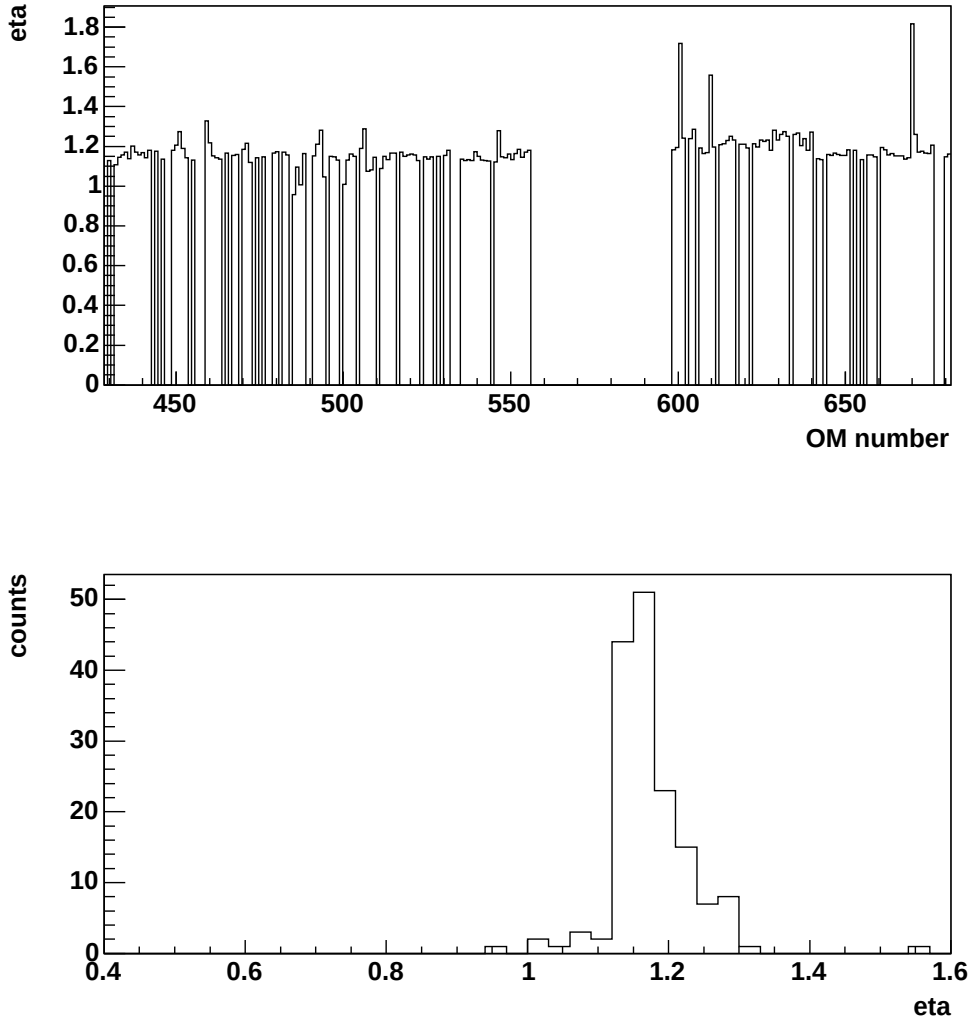

Figure A.8: Hit efficiency for the optical OMs in strings 14 to 19. The the ratio of pulses η for each OM is shown above, while the distribution of η is shown below.

List of Figures

List of Tables

Bibliography

[A+00] E. Andres et al. The amanda neutrino telescope: Principle operation and first results. *Astroparticle Physics*, 13:1–20, 2000.

[A+01] E. Andres et al. Observation of high-energy neutrinos using cherenkov detectors embedded deep in antarctic ice. *Nature*, 410:441 – 443, 2001.

[A+02a] J. Ahrens et al. Limits to the muon flux from wimp annihilation in the center of the earth with the amanda detector. *Phys.Rev.*, D66(032006), 2002.

[A+02b] J. Ahrens et al. Observation of high energy atmospheric neutrinos with the antarctic muon and neutrino detector array. *Physical Review D*, 66, 2002.

[A+02c] J. Ahrens et al. Search for supernova neutrino-bursts with the amanda detector. *Astroparticle Physics*, 16:345, 2002.

[A+03] J. Ahrens et al. Search for neutrino-induced cascades with the amanda detector. *prd*, 67(012003), 2003.

[A+04a] J. Ahrens et al. Muon track reconstruction and data selection techniques in amanda. *Nuclear Instruments & Methods*, 524:169–194, 2004.

[A+04b] J. Ahrens et al. Twr software manual. 2004.

[Ack] M. Ackermann. *Datahandler manual pages.* DESY-Zeuthen, http://www.ifh.de/nuastro/protected/datahandler.html.

[Ahr01] J. Ahrens. Ein webbasiertes überwachungsystem fr das amanda neutrinoteleskop. Master's thesis, Johannes Gutenberg-Universitt Mainz, 2001.

[B+91] A. Burrows et al. The future of supernova detection. *Physical Review D*, 45(10), 1991.

[B+00] R. Barth et al. *GS Multi-Branch System User Manual*. Gesellschaft für Schwerionenforschung mbH GSI, Planckstr. 1 D-64291 Darmstadt Germany, 2.2 edition, 2000.

[B+01] S. W. Barwick et al. Potential of amanda ii in he neutrino astrophysics. In *Proceedings of the 27th International Cosmic Ray Conference, Hamburg, Germany*, pages 1–4, 2001.

[Bec04] J. K. Becker. Calculation of the agn neutrino flux and of event rates for large volume neutrino telescopes. Master's thesis, University of Wuppertal, 2004. WU D 04-06.

[Blo84] V. Blobel. Unfolding methods in high–energy physics experiments. Proceedings of the 1984 CERN School of Computing, CERN, 1984.

[CMU95] P. Padovini C. Megan Urry. Unified schemes for radio-loud active galactic nuclei. *Publ.Astron.Soc.Pac.*, 107(803), 1995.

[Eks04] P. Ekstroem. *A Dark Matter Search with AMANDA*. PhD thesis, Stockholm University, 2004.

[FB95] H. Falcke and P. L. Biermann. The jet-disk symbiosis. I. Radio to X-ray emission models for quasars. *Astronomy & Astrophysics*, 293:665, 1995.

[Gai90] Thomas K. Gaisser. *Cosmic Rays and Particles*. Cambridge University Press, 1990.

[Gee03] H. Geenen. Atmospheric neutrino and muon spectra measured with the AMANDA-II detector. In *Proceedings of the 28th ICRC*, Tsubuka, 2003.

[Gre66] K. Greisen. End to the Cosmic-Ray Spectrum? *Physical Review Letters*, 16, 1966.

[Gro] A. Groß. Phd thesis in preparation.

[Gro04] Particle Data Group. *Particle Physics Booklet*. Springer, 2004.

[H+95] M. Honda et al. Calculation of the flux of atmospheric neutrinos. *Physical Review D*, 52:4985, 1995.

[H+01] S. Hundertmark et al. A method to detect uhe neutrinos with amanda. In *Proceedings of the 27th International Cosmic Ray Conference, Hamburg, Germany*, 2001.

[Hes11] V. F. Hess. über die absorption der g–strahlung in der atmosphäre. *Physikalische Zeitschrift*, 12(22,23):998–1001, 1911.

[Hes12] Viktor Franz Hess. über beobachtungen der durchdringenden strahlung bei sieben freiballonfahrten. *Physikalische Zeitschrift*, 13:1084–1091, 1912.

[JKB] P. L. Biermann and W. Rhode J. K. Becker. In Prep.

[JL95] S. Pakvasa J.G. Learned. Detecting ν_τ oscillations at pev energies. *Astroparticle Physics*, 3(3):267–274, 1995.

[K+97] A. Karle et al. Analog optical transmission of fast photomultiplier pulses over distances of 2 km. *Nuclear Instruments & Methods*, 387:274–277, 1997.

[Kam01] K.-H. Kampert. Cosmic rays and particle physics. *Heavy Ion Phys.*, 14:203–215, 2001. invited talk presented at the "Symposium on Fundamental Issues in Elementary Matter".

[Lei03] H. Leich. *GPS2VME User's Guide*. DESY Zeuthen, January 2003.

[Leo94] W.D. Leo. *Techniques for Nuclear and Particle Physics Experiments*. Springer Verlag, 1994.

[LM00] J. G. Learned and K. Mannheim. High-energy neutrino astrophysics. *Annu. Rev. Nucl. Part. Sci.*, 50:679, 2000.

[Lon92] M.S. Longair. *High Energy Astrophysics*, volume 1. Cambridge University Press, 1992.

[M+] K. Münich et al. In Prep.

[Man95] K. Mannheim. High-energy neutrinos from extragalactic jets. *Astroparticle Physics*, 3:295, 1995.

[Man96] K. Mannheim. Beacons at the gamma ray horizon. *ArXiv Astrophysics e-prints*, 1996.

[Man97] K. Mannheim. Agn models: High-energy emission. *ArXiv Astrophysics e-prints*, 1997.

[Mes] T. Messarius. Phd thesis in preparation.

[Mes03] T. Messarius. Analyse von zufälig getriggerten daten des amanda-detektors. Master's thesis, University of Wuppertal, 2003. WU D 03-02.

[Mir04] I. F. Mirabel. Microquasar – agn – grb connections. *app*, 2004.

[MPR01] K. Mannheim, R. J. Protheroe, and J. P. Rachen. Cosmic ray bound for models of extragalactic neutrino production. *Physical Review D*, 63:23003, 2001.

[MRS03] A. D. Martin, M.G. Ryskin, and A.M. Stasto. Prompt neutrinos from $c\overline{c}$ and $b\overline{b}$ and the gluon at very small x. *ArXiv Astrophysics e-prints*, 2003.

[Mun] K. Munich. Phd thesis in preparation.

[Nam] J. Nam. Private communication. UCI Irvine, http://www.ps.uci.edu/ jwnam.

[P+99] W. S. Paciesas et al. The fourth batse gamma-ray burst catalog (revised). *ArXiv Astrophysics e-prints*, 1999. accepted for publication in Ap. J. Suppl.

[R+56] F. Reines et al. Detection of the free neutrino: A confirmation. *Science*, (124):103, 1956.

[RB93] J. P. Rachen and P. L. Biermann. Extragalactic Ultra-High Energy Cosmic-Rays - Part One - Contribution from Hot Spots in Fr-II Radio Galaxies. *Astronomy & Astrophysics*, 272:161, 1993.

[Ref] F. Refflinghaus. Diploma thesis in preparation.

[Rib] M. Ribordy. A new method to estimate the angular resolution. webpage.

[S+03] K.Z. Stanek et al. Spectroscopic discovery of the supernova 2003dh associated with grb 030329. *Astrophys.J.*, 591:L17–L20, 2003.

[Sch02] Th. Schmidt. *Aufbau und Funktionsnachweis eines Optischen Moduls mit optisch-analoger Pulsübertragung für den AMANDA–II– und ICECUBE– Detektor*. PhD thesis, Humboldt Universität Berlin, Germany, 2002.

[SNO02] SNO Collaboration. Direct Evidence for Neutrino Flavor Transformation from Neutral-Current Interactions in the Sudbury Neutrino Observatory. *Physical Review Letters*, 89:11301, 2002.

[SS96] F. W. Stecker and M. H. Salamon. High Energy Neutrinos from Quasars. *Space Science Reviews*, 75:341, 1996.

[Sup98] SuperKamiokande Collaboration. Evidence for Oscillation of Atmospheric Neutrinos. *Physical Review Letters*, 81:1562, 1998.

[Sys02] Struck Innovative Systems. *SIS1100/SIS3100 Standard Design Firmware Version 5 User Manual*. http://www.struck.de, version: 1.30 edition, August 2002.

[Sys03] Struck Innovative Systems. *SIS3300/SIS3301 65/80/100 MHz VME FADCs Users Manual, Dedicated AMANDA Firmware Version: 1.00*. http://www.struck.de, version: 1.00 edition, January 2003.

[VZ80] L. V. Volkova and G. T. Zatsepin. Promt lepton generation-atmospheric muon and neutrino spectra at high-energies. *Soviet Journal of Nuclear Physics*, 37:212, 1980.

[W+99] K. Woschnagg et al. Optical properties of south pole ice at depths from 140 to 2300 meters. In *Proceedings of the 26th International Cosmic Rays Conference*, volume 2, page 200. ICRC XXVI, 1999.

[W+01] R. Wischnewski et al. Performance of the amanda ii detector. In *Proceedings of the 27$^{\text{th}}$ International Cosmic Ray Conference, Hamburg, Germany*, pages 1105 – 1109, 2001.

[W+02] C. Wiebusch et al. Results from amanda. *Modern Physics Letters A*, 17(31):2019–2037, 2002.

[WB99] E. Waxman and J. Bahcall. High energy neutrinos from astrophysical sources: An upper bound. *Physical Review D*, 59:23002, 1999.

[Wie98] B. Wiebel Sooth. *Measurement of the allparticle energy spectrum and chemical composition of cosmic rays with the HEGRA detector*. PhD thesis, University of Wuppertal, 1998.

[YS85] H. Elliot Y. Sekido, editor. *Early History of Cosmic Rays*. D. Reidel, 1985.

Appendix B

Acknowledgement

This work has been pursued in the framework of the AMANDA collaboration and I would like to thank all former and present members. After three years, it is difficult to remember all persons who have contributed to this work. I am sure that I will forget someone.
If there are two persons, I have to thank most, these are Prof. Wolfgang Rhode and Karl-Heinz Becker. I would like to thank them for their continuous and unrelenting support during the last three years.
When I first arrived at the South Pole, I felt a little lost. I was a member of the collaboration for about five month, but my knowledge about the detector and the conditions in Antarctica were still very limited. Without the invaluable help from the Mainz collaborators, Tom Feser, Marc Hellwig and Jens Ahrens, the TWR project would not have been a success. Together we managed to solve a lot of problems. I also have to thank Henrike Wissing and Jiwoo Nam for their inestimable help.
I have to thank Steven W. Barwick for his support for the TWR project. The two weeks which I spent in Irvine helped a lot to increase my knowledge about AMANDA detector. He was of invaluable help in finding weak points in the TWR system and giving impulses to solve them. I am grateful to Jiwoo Nam for helping me to find critical bugs in the DAQ system and for many interesting discussions.
I also feel grateful to all my colleagues from the Astroparticle group in Wuppertal. Especially, I have to thank my room mates Kirsten Münich, Julia Becker, Heidrun Bojahr and Matthias Bartelt for the nice and friendly atmosphere.
Furthermore, I am indebted to Andreas Gross for his great work on track reconstruction with TWR data and to Timo Messarius for his extensive work on the TWR system and the new trigger system. I also have to thank Christopher Wiebusch for his encouraging support for our project.
Special thanks go to Tino Häupke and Matthias Kirsch for their helpful

support in critical situations at the Pole and numerous discussions about further possibilities of the TWR.
I also would like to thank Dr. Nikolaus Kurz from the Gesellschaft für Schwerionenforschung for his support with the MBS system.
This work has profited a lot from discussions with Markus Ackermann, Stephan Hundertmark, Tonio Hauschildt, Mathieu Ribordy, Thierry Castermans, Christine Burgess and others at the Pole and in the Northern hemisphere.
Thanks to Oana Taşcău, I did not forget that there still exists a world outside the University.
To my family, thank you very much. Although my Grandmother was worried, when I first told her about going to the Pole, she always supported me.